Wafer-Scalable Fabrication of Metal Nanostructures for Plasmonics-Assisted Biomedical Sensing Applications

Thesis by
Chieh-feng Chang

In Partial Fulfillment of the Requirements for the Degree
of
Doctor of Philosophy

CALIFORNIA INSTITUTE OF TECHNOLOGY
Pasadena, California
2015
(Defended May 27, 2015)

© 2015
Chieh-feng Chang
All Rights Reserved

To my parents

ACKNOWLEDGEMENTS

I have received so much help along the way during these years at Caltech, and there are so many people I have to thank. The list may be incomplete, but my gratitude goes to all the people who have enriched my life professionally, socially, or in another way.

First and foremost, I would like to dedicate this thesis to my parents for all their encouragement and support all along, not just during my graduate studies here at Caltech but for every day in my life. You have been the most important backing force for me to stay coherent in the Ph.D. program, and without you I cannot imagine how much more difficult it would have been for me to go through this stage. I would also like to thank you for your patience and understanding when I was unable to visit you in Taiwan for a few years in a row due to heavy schedules of research and experiments. Your immeasurable love is something I can never fully repay in my life.

I would like to thank my advisor, Prof. Axel Scherer, for the opportunity of working in the Nanofabrication Group. You have taught me so much not only about scientific training, but also about strategic thinking, life philosophies, and so on. It is always fun to listen to those anecdotes you can readily share, from people's hilarious fiascos in the cleanroom to different methods of raising piglets in the farms. It is hard to believe that so many years have passed while it seems yesterday when you were telling me what the Ph.D. program is really about in our first meeting. I will remember all the precious advice well.

A million thanks go to Dr. Sameer Walavalkar, who has been such an extraordinary mentor for my thesis work. Thank you for showing me so many cool tricks about nanofabrication, for arranging a number of collaboration opportunities, and for having all the inspiring sessions of discussion and brainstorming for ideas and results. You are such an outstanding scholar, and it has been a privilege to work together with you. It has been a great pleasure as well since I truly enjoy all your comments that are so humorous but true on science, sports and many other topics. I am also heartily thankful that you genuinely care about my career development, and I look forward to more opportunities of working with you.

I spent so much wonderful time together with Dr. Aditya Rajagopal, and I really miss your company after you moved out of Pasadena for your career. I can still vividly recall the time when we pulled many all-nighters for problem sets together in the library, and time flies so fast. You have been one of the best buddies I have ever met, and I had such a great time traveling to

conferences together with you in Washington, D.C., in Germany, and in Maui. I miss the time when we were working together on the same project, sharing jokes, camaraderie, and exciting new ideas. I look forward to another opportunity of working with you again in the future.

Dr. Se-Heon Kim has been a great mentor in teaching me the techniques of nanolaser fabrication, vacuum technologies, microscopy tricks, numerical simulation, and many others. It was a wonderful experience learning from experts like you, and you always speak in a kind and modest manner like a gentleman scholar. Due to the change of funding sources, unfortunately at the end I did not continue the projects on III-V materials, but the training and the methodology you taught me still played a big role in my subsequent research. I wish you all the best in the Bay Area.

In addition to the aforementioned people, credit also goes to the Nanofabrication Group members for their friendship and for their help in my learning of cleanroom techniques. Kate Finigan is not only a helpful group administrator, but also a good personal friend who offered much advice regarding how I should approach life. I enjoyed many conversations with Mark Goldberg about theatre, movies, philosophies, and the world in general; thank you for being a wonderful and considerate friend during my years in the Nanofabrication Group. Andrew Homyk is an awesomely brilliant researcher, who knows not only about science but basically about everything. I really appreciate all the comments and suggestions you gave me when I was trying to figure things out. Dr. William Fegadolli, Dvin Adalian, and Samson Chen all helped me with various projects, from fixing vacuum pumps to the secret sauce of aligned electron beam lithography. Keith Russell always approaches things with dedication and competence; thank you so much for helping with many things in the laboratory. Lots of thanks also go to various group members who have contributed to the friendly atmosphere of the Nanofabrication Group, including Dr. Mike Shearn, Dr. Joyce Wong, Xiomara Madero, Erika Garcia, Juan Pablo Cardenas, and many others. Beyond the Nanofabrication Group, I need to thank Brandon Marin a lot for his impressive knowledge about biomolecules. You also have an awesome sense of humor, and it was so pleasant to work with you. Congratulations to your recent success in internship and in your personal life, and I am very sure you will keep rocking. I also thank C. J. Yu for his help with biochemistry.

I would like to thank my other committee members for their scientifically-inspiring comments: Prof. Scott Fraser, Prof. David Rutledge, and Prof. Amnon Yariv. Thank you so much for taking time being on my committee despite your super busy schedules, and for all the guidance you offered during the meetings. I was taking classes from Prof. Rutledge and Prof. Yariv during my

first year, and suddenly the graduate program is close to the end. Prof. Fraser has been offering all the insightful and constructive comments about future possibilities of my research, which I sincerely appreciated. Outside of Caltech, I would like to thank Prof. Andrea Tao from UCSD and Prof. Stephen Cronin from USC for allowing me to use their Raman microscope.

I would have been fighting with machine issues all the time instead of doing research without the KNI staff members who keep the place running smoothly: Dr. Guy DeRose, Melissa Melendes, Nils Asplund, Bophan Chhim, Steven Martinez, Matthew Sullivan, and many others. In particular, special thanks go to Melissa and Bophan who taught me so much when I first entered the world of nanofabrication, and the learning curve would have been much steeper without your kindness and patience. I would like to thank Melissa for also being a considerate personal friend, who always cares about if things are going well and if I am feeling alright. You have brought so much warmth to the cleanroom deep in the ground. I learned a great deal from Dr. DeRose about the electron beam lithography, which plays a very important role in this work. Probably due to his rigorous training and outstanding service record in the Underwater Demolition Team, Nils is always so meticulous in making sure that hardware glitches are removed in time. Many thanks also go to Steven and Matthew for teaching me how to use new machines and showing me tricks of improving the results of electron microscopy.

I am sincerely grateful to the Reed family: Daniel, Alice, Christopher, and Stephanie, as well as Kari Johnson. You are like another family to me during all these years, and I owe so much gratitude to you for all the kindness, hospitality, and encouragement. Thank you so much for inviting me to many parties and trips, which added lots of warmth and fun to my life outside of the cleanroom. During those days when I was still trying to see the light from the other end of the tunnel, you are like a cool breeze taking away the sweat on my forehead and reminding me that there would be an exit somewhere out there in the distance as long as I persevere. I am so fortunate to have you in my life.

Many Caltech people also offered lots of personal friendship during my stay. I would like to thank Laura Flower Kim and Daniel Yoder from the ISP Office, who greatly care about my well-being. I had a ton of fun working with you during the international student orientation and the Caltech World Fest. Tomasz Tyranowski and I have so many common hobbies; it was big fun to spend time with you, and you have my best wishes for your post-Caltech life. Outside of Caltech, I would like to thank Chu-Yi Wang, Edwin W. Chen and Julian T. Yeh for the moral support.

Last but not least, I would like to acknowledge the International Fulbright Science and Technology Program for all the wonderful adventures and experiences I would otherwise have no access to without being a Fulbrighter. The Fulbright gateway orientation, the S&T seminars and the Capstone meeting will forever be treasured and unforgettable memories to me. Specifically I would like to thank Ann Kerr, who coordinates the Fulbright activities in the Greater Los Angeles area, for inviting me to all the cultural events and for sharing so many intercultural anecdotes with me. I also made many good friends from the Fulbright program, especially Anke Zwirner, Emily Stork, and Friederike Wrobel. I really appreciate it that you always thought of me when throwing a party, and that you stayed in touch after you moved on to the next stage of your career.

Thank you all, for everything.

ABSTRACT

Plasmonics provides many opportunities of sensing and detection since it combines the nanoscale spatial confinement and the optical temporal resolution. The wireless nature of photonic investigation, moreover, is very desirable for biomedical applications. Plasmonic metals, however, are difficult to pattern with great nanoscopic precision, and traditional approaches were time-consuming, non-scalable, stochastically-manufactured, or highly-limiting in the pattern designs. In this work, wafer-scalable nanofabrication methods are presented for various plasmonic structures for biomedical sensing applications. The fabrication steps have ready counterparts in commercial semiconductor foundries and therefore can be directly applied for mass production.

The fabrication and measurement of extraordinary transmission (EOT) are discussed in Chapter 2. Fabrication options are available for substrates like silicon-on-sapphire and silicon-on-glass, so that the devices can be mechanically robust for user-friendliness. The metal layer can also be varied for EOT applications in different ranges of wavelengths. The EOT nanostructures can be fabricated to be polarization-sensitive, and the concept of fluorescence-based EOT assays is demonstrated.

The fabrication and applications of surface-enhanced Raman spectroscopy (SERS) are then discussed. With a hybrid approach, the top-down designing defines uniform SERS nanostructures on a chip, while the bottom-up process of thermal reflow increases the fabrication precision beyond the lithography resolution limit. Based on the thiophenol study, an enhancement factor greater than 10^{10} can be achieved. The first Raman spectrum of tracheal cytotoxin is demonstrated without any special sample preparation, and thrombin binding could be easily resolved through chip functionalization. The binding dynamics of ethyl mercaptan, which is similar to the highly toxic gas of hydrogen sulfide, can be detected with a good resolution in time at a low concentration.

With a few more steps of fabrication, the plasmonic structures can be integrated into systems that do not call for laboratory infrastructures. A built-in micro-channel on a chip can make the device useful without dedicated support of a microscope or additional microfluidic structures. The nanostructures can also be transferred onto flexible substrates for better conformity onto various surfaces. Finally, the SERS structures can be transferred onto a fiber tip for in-field or through-the-needle applications, especially when combined with a portable Raman-scope.

TABLE OF CONTENTS

Chapter 1 Introduction....1
Chapter 2 Extraordinary Transmission (EOT)....6
2.1 Fabrication....8
2.1.1 Electron Beam Lithography....9
2.1.2 Deposition and Lift-Off of Hard Mask....9
2.1.3 Etching....10
2.1.4 Thermal Oxidation....14
2.1.5 Metal Deposition....15
2.1.6 Removal of Protruding Nanostructures....19
2.1.7 Photolithography and Substrate Opening....23
2.2 Choices of Substrates and Metals....27
2.2.1 Silicon-on-Sapphire Substrates....28
2.2.2 Silicon-on-Glass Substrates....33
2.2.3 Options for the Metal Layer....37
2.3 EOT Characterization....41
2.3.1 Experimental Setup....41
2.3.2 Polarization Measurement....42
2.3.3 Comparison between Au and Al....46
2.4 EOT Fluorescence Measurement....47
Chapter 3 Surface-Enhanced Raman Spectroscopy (SERS)....52
3.1 Fabrication....55
3.1.1 Thermal Reflow of Au....56
3.1.2 Facilitating the Thermal Reflow....59
3.1.3 Optional Masking of Substrate....61
3.2 Characterization with Thiophenol....62
3.3 Simulation and Enhancement Factors....64
3.3.1 MEEP Simulation....64
3.3.2 Definition and Calculation of Enhancement Factors....67
3.4 Tracheal Cytotoxin (TCT) Measurement....69
3.5 Aptamers and Thrombin....70
3.5.1 Aptamer Attachment....70
3.5.2 Thrombin Binding....72
3.5.3 Temperature Response....78
3.6 Hydrogen Sulfide and Ethyl Mercaptin....81
Chapter 4 Integration into Systems....84
4.1 Variations for Integrated Microfluidics or Implantation Applications....84
4.2 Plasmonic Structures on Flexible Substrates....88
4.3 All-Fiber Sensors and Systems....95
Chapter 5 Conclusions and Future Directions....106

LIST OF FIGURES

Figure 2.1 Examples of slanting sidewalls of FIB cross sections. 7
Figure 2.2 Schematic diagrams of (A) RIE etching and (B) ICP-RIE etching....... 11
Figure 2.3 (A) Pseudo Bosch process, right before the passivation layer in the forward direction is removed by the ion milling effect; (B) the SF_6 component in the plasma can now etch the exposed areas of silicon. The green color denotes the passivation layer of C_4F_8, and the red color means the mask. 12
Figure 2.4 Control of the sidewall angle from the pseudo Bosch etching to be (A) slanting inward, (B), etched vertically, or (C) slanting outward. 13
Figure 2.5 Examples of arbitrary shapes made possible by the top-down process of lithography and etching. 14
Figure 2.6 Results of evaporation from the CHA machine on chips of different etching depth. The structures in (A) and (B) were shorter than those in (C) and (D), while the thickness of the Au deposition was the same. 17
Figure 2.7 Results of evaporation from the TES machine; the sidewall deposition was more serious than in CHA. 18
Figure 2.8 Insufficient thermal reflow of Au due to the shape and/or density of nanostructures. 20
Figure 2.9 Result of thermal reflow from a chip with evaporated Au. 21
Figure 2.10 (A) and (B) show the revealed top of nanostructures after the resist layer had been ashed to the appropriate height; (C) and (D) show the results right after the TFA Au etch. 21
Figure 2.11 Fabricated nano-apertures on a 200 nm layer of Au. 22
Figure 2.12 (A) Blurry vacuum viewport of the XeF_2 etcher; (B) residues from chips with Au inadvertently placed in the chamber by previous users. 25
Figure 2.13 Fabrication sequence of nano-apertures for EOT on silicon for the sputtering option. 26
Figure 2.14 Fabrication sequence of nano-apertures for EOT on silicon for the evaporation approach. 27

Figure 2.15 (A) Undercut etching, or known as notching, would occur when the SOS chips were etched for too long in the plasma; (B) no undercut etching around the base when the silicon layer was not etched through (scale bar: 200 nm); (C) and (D) show the examples when the silicon layer were about to be etched away. 29

Figure 2.16 (A) and (B) are results of successful thermal reflow from SOS chips; (C) and (D) show the nano-apertures after mechanical snapping. 30

Figure 2.17 (A) and (B) are examples for the RIE oxide etch to remove the silicon dioxide stubs all the way into the nano-apertures; (C) and (D) show that the etch time can be controlled for a flush surface. 31

Figure 2.18 In (A) and (B), gold was about to recede from the base of the nanostructures when the temperature was too high; at an even higher temperature, larger openings would result as in (C); (D) shows another sign indicating higher temperature than necessary, when the Au around the nanostructure base region would reflow slightly upwards along the sidewall. 32

Figure 2.19 (A) Absorption depth of silicon at different optical wavelengths. (B) FFT mode of Filmetrics F40 for measuring thick silicon; (C) the wavelength range can be further specified to improve fitting results. 34

Figure 2.20 (A) Calibrated etch rate for thinning down the top silicon layer on SOG chips. (B) Photo of thinned SOG chips; the right one came from the edge of an SOG wafer. Chip size: 10 by 10 mm. 36

Figure 2.21 (A) Nanostructures on an SOG chip after pseudo Bosch etching. (B) Remaining thickness of the silicon layer after plasma thinning and pseudo Bosch etching. 36

Figure 2.22 After a resist layer was spin-coated on the chip, oxygen plasma ashing could remove the right amount of resist to reveal the top of the nanostructures. 37

Figure 2.23 CD-26 developer would etch away aluminum without affecting silicon dioxide or the resist layer, as shown in (A) and (B). Without an etch stop, if the etch time was too short the results would look like (C) and (D), while over-etching would be like (E) and (F). 39

Figure 2.24 Examples of nano-apertures on an aluminum film. 40

Figure 2.25 (A) and (B) show the feasibility of evaporating aluminum on SOS chips with nanostructures; (C) and (D) are results after the nanostructures are mechanically snapped. 40
Figure 2.26 Schematics of the experimental setup for EOT measurement. 42
Figure 2.27 Transmission spectra of various nano-apertures on a 200 nm Au layer. 43
Figure 2.28 (A) One example of the CAD design for two-component nano-apertures; (B) – (F) are transmitted spectra for the patterns with different offsets between the components. 45
Figure 2.29 (A) Au and (B) Al EOT transmission spectra from the same pattern of nano-apertures and at the same metal thickness. 46
Figure 2.30 Procedures of photo-uncaging. (A) DECM-CG is first coated on the chip; (B) UV exposure from the backside photo-uncages the molecules at the nano-apertures; (C) FITC fluorophores are then attached to the photo-uncaged areas; (D) FITC fluorescence can now be excited from the backside. 48
Figure 2.31 Scanned images of (A) reflection and (B) transmission from the backside sapphire surface at focus; laser: 633 nm. (C) Transmission image illuminated by the 488 nm source when the nano-apertures were roughly at focus. 49
Figure 2.32 (A) Extraordinary refractive index n_e of sapphire as a function of wavelength. (B) Much sharper microscopy image when the refractive index liquid was used. 50
Figure 2.33 Microscopy images of nano-apertures when illuminated by a laser source at (A) 488 nm, (B) 561 nm, and (C) 633 nm. 51
Figure 3.1 Jablonski diagrams of Rayleigh and Raman scattering. 53
Figure 3.2 Fabrication sequence of SERS nanostructures on silicon. 56
Figure 3.3 Different results from various parameters of thermal reflow. (A): incomplete separation; (B): separated but not bulbed; (C): good examples of nano-bulbs; (D): a 15 nm gap between nano-bulbs. 57
Figure 3.4 Formation of nano-bulbs when (A) some nanopillars tilted to the other one, and (B) one nanopillar leaned to the side. 58
Figure 3.5 Results of excessive thermal processing on SERS chips. 59

Figure 3.6 Oxidized nanopillars after a brief immersion in BHF for (A) ~2 seconds and (B) ~6 seconds. 59
Figure 3.7 Thermal reflow results from chips that were treated in BHF for different durations of time. 60
Figure 3.8 SERS structures with a PMMA layer masking the bottom substrate. 61
Figure 3.9 SERS and regular Raman spectra of thiophenol with an offset between data; the skeletal formula of thiophenol is shown next to the legend. 64
Figure 3.10 Electric field strength from MEEP simulation results of nano-bulbs with dimensions from actual chips. (A) and (B) are the *xz* and *xy* cross sections from an excitation source of 633 nm; (C) is the *xz* plot from 675 nm. 66
Figure 3.11 Extended Raman spectrum of tracheal cytotoxin. 70
Figure 3.12 Role of thrombin during coagulation *in vivo*. 73
Figure 3.13 (A) Customized chamber on glass slide for injection of thrombin solution at various concentrations. (B) Raman spectra of TBA aptamers with no thrombin and different thrombin concentrations of 1, 10, and 100 pm. 74
Figure 3.14 Relative peak strength between Raman modes of thrombin and TBA aptamers. 76
Figure 3.15 Time evolution of the Raman spectra from the binding dynamics of 500 fM thrombin onto TBA aptamers. 77
Figure 3.16 Schematics of different conformations of TBA aptamers, when they are unraveled, folded in quadruplex, or attached to thrombin. 79
Figure 3.17 Raman spectra of thrombin and TBA aptamers when the solution was (A) heating up and (B) cooling down. 80
Figure 3.18 Time evolution of Raman spectra of ethyl mercaptan on Au nano-bulbs. 83
Figure 4.1 Fabrication sequence of SERS nanostructures in a recessed region on silicon. 85
Figure 4.2 Black silicon was about to occur since the passivation level was not enough in the cryogenic etch. 87
Figure 4.3 Fabricated nanostructures in recessed regions on silicon. 87

Figure 4.4 (A) – (C): Fabrication sequence of SERS nanostructures on a flexible substrate; the amount of embedding of Au nanocups in the substrate can be controlled as in (D) and the final device can be compressed or stretched as in (E). 89

Figure 4.5 Various SEM micrographs of fabricated Au nano-cups. 91

Figure 4.6 Fabrication steps to shrink the nanostructure size beyond the lithography resolution limit. After Si nanostructures are defined in (A), they are partially oxidized as in (B). After the removal of the outer SiO_2 layer as in (C), the structures can be oxidized again as in (D). 91

Figure 4.7 Fabrication sequence of SERS or EOT nanostructures on a flexible substrate in an upright orientation. 92

Figure 4.8 SEM micrographs of SERS Au nano-bulbs transferred onto PDMS in an upright position. 93

Figure 4.9 Fabrication sequence of SERS Au nano-bulbs on a flexible substrate with the bottom Au layer removed. 94

Figure 4.10 SEM micrographs of Au nano-bulbs with the bottom Au layer removed. 95

Figure 4.11 Schematic diagrams of (A) the transfer of Au nano-bulbs onto a fiber tip and (B) the working principle of a SERS fiber. 96

Figure 4.12 Optical micrograph of a fiber chip (A) before and (B) after the removal of the bottom Au layer. (C) shows the associated SEM micrograph after the Au layer was removed. (D) is an optical micrograph after the Si region below the patterns was already etched. 97

Figure 4.13 (A) SEM micrograph of a fabricated SERS fiber showing the nanostructures on the tip; (B) and (C) show the zoomed-in images at the edge and at the center of the nano-patterns, respectively. (D) shows the lateral dimensions when imaged from the side. 98

Figure 4.14 Optical micrographs of the SERS fiber (A) from the end and (B) from the side. 99

Figure 4.15 Anticipated Fabry-Perot effect due to the adhesion layer at the fiber tip; excitation: 633 nm. 100

Figure 4.16 SEM micrographs of a SERS fiber in a hypodermic needle. 101

Figure 4.17 Schematic diagram of a benchtop all-fiber SERS system. 102
Figure 4.18 Working mechanism of 90/10 optical fiber coupler. 104
Figure 4.19 Schematic diagram of a portable all-fiber SERS system..... 105
Figure 5.1 (A) Screenshot of a photomask covering portions of EOT nano-apertures for partial photo-uncaging. (B) Schematic diagram of a smart petri dish based on EOT nano-apertures..... 108
Figure 5.2 Schematic diagram of another configuration of SERS fiber tip. 109
Figure 5.3 (A) Schematic of local field enhancement between Au nano-bulbs from numerical simulation. After the chip is coated with a photo-sensitive material, it can be illuminated at a correct amount of flux so that photo-reaction only takes place around the hot spots, as in (B). These spots are now accessible again as in (C), which can be functionalized as in (D). The same technique can be applied to the interior cavities of nanocups, as shown in (E) and (F). 111
Figure 5.4 Fabrication of plasmonic nanostructures on a flexible sticker through (A) a carrier chip or (B) substrate etching. The final structure as (C) can conform onto a non-flat surface while preserving the nanostructures. In (D), with a thicker sacrificial layer (left) or an etched carrier chip (right), the patterns can be transferred upright as in (E). EOT nano-apertures can be processed in a similar way, as shown in (F)..... 113
Figure 5.5 (A) Au nano-bulbs after thermal reflow, which can be topically shaped with focused ion beam as in (B) or generally modified with ion milling as in (C). Shadow evaporation can also be the method of metal deposition to fabricate asymmetric nanocups, as shown in (D)..... 114

Chapter 1

Introduction

Miniaturization has been a constant trend of science and technology in the past millennia. Shrinking the system without sacrificing the performance means better mobility, lower cost, easier production, and many other associated benefits. The same fashion was still going strong in the past decades, especially for the famous Moore's Law in the electronics industry [1]. In photonics, the size of a laser has evolved from the first bulky ruby laser [2] into highly-compact semiconductor lasers in consumer electronics, and various nano-lasers in laboratories [3, 4]. Over the years, electronic and optical devices alike have become faster and more power-efficient, thanks to the rigorous evolution of miniaturization.

As this trend continues, however, some bottlenecks start to emerge on the horizon. Miniaturization of transistors is now coping with challenges like material strength, leakage currents, and so on. Perhaps one of the most prominent issues is the transistor bandwidth, which had been steadily increasing in the past decades until very recently. Commercial chips, such as the central processing unit (CPU) in computers, slowed down their steps for reaching an even higher clock rate and instead adopted the multi-core designs to improve the overall performance. In the research world, while Si transistors operating around 200 GHz have been demonstrated [5], it is not very likely for them to go way faster than this in the near future. Various applications like sensing, on the other hand, demand an even higher bandwidth. Photonics, on the other hand, enjoys hundreds of THz in terms of bandwidth, but its miniaturization has not been so extraordinary when compared with the electronics counterparts. Many optical setups still require bulky mechanical components on an optical table, and integrated photonics on a chip is still an ongoing effort for standardization, computer-aided design, and so on. In addition, the inefficient conversion between electric and photonic energy prevents electronics from taking advantage of the optical bandwidth, while the diffraction limit disables photonic signals from accessing individual nanoscale features already pervasive in electronic chips. As a result, it has been a popular research topic regarding how to combine the strengths of all these areas.

Plasmonics provides such an opportunity. Plasmonics is the interaction between photons and metals when light impinges on a metal-dielectric interface [6, 7]. At such an interface, light can be further manipulated on the nanoscale if metal structures can be made several times smaller than the optical wavelength [8]. Fortunately, fabrication of such small structures has been possible thanks to all the nanotechnology developed for device miniaturization in electronics. Now the high bandwidth and fast temporal features of optics can start to be combined with spatial confinement for investigations on the nanoscale.

In addition, plasmonics can also provide a plethora of information around the metal-dielectric interface. For metals, the dielectric constant can be defined as [9]

$$\tilde{\epsilon}(\omega) = 1 - \frac{{\omega_p}^2}{\omega^2 - i\gamma\omega},$$

where γ is the damping constant and $\omega_p = \sqrt{Ne^2/\epsilon m^*}$ is the plasma frequency with N being the electron density, e the electron charge, ϵ the permittivity, and m^* the effective electron mass. The material behavior is thus different as a function of the wavelength and sensitive to the dielectric properties immediately surrounding the metal. When the frequency is way below the plasma frequency, $\omega \ll \omega_p$, the real part of the effective permittivity is negative, resulting in a highly-reflecting metal-dielectric interface. Metals are therefore excellent mirrors at frequencies from the microwave range to mid-infrared. Above the plasma frequency, $\omega > \omega_p$, the real part of the effective permittivity becomes positive, and metals behave like transparent dielectric materials with unique dispersion characteristics. This is one reason that metals are no longer good materials as reflectors for deep-ultraviolet or even X-ray applications. At optical frequencies, the real part of the metal dielectric constant is negative, so this contrast with the positive ϵ of the neighboring dielectric material results in very strong confinement of light at the surface. On the other hand, the magnitude of the imaginary part of the metal dielectric constant is still smaller than that of the real part, so overall the loss is not too significant for the signals to be excessively attenuated, and bound modes or traveling waves can be supported at the interface. These properties have been used in applications like surface plasmon resonance (SPR) to determine the density of self-assembled monolayers [10]. For plasmonic applications, Au and Ag are the most common metals; Al and Cu are also used

[11]. Occasionally, other metals such as Cr, Pt, Pd, Ni, etc. may also be chosen [11]. Table 1.1 shows the plasma wavelengths and damping constants of Au, Ag, Al, and Cu [11, 12].

Metal	Plasma Wavelength (nm)	γ (eV)
Au	139	0.07
Ag	135	0.02
Al	98	0.13
Cu	142	0.07

Table 1.1 Plasma wavelengths and damping constants of some metals commonly used for plasmonics.

These metals are, however, difficult to etch with great resolution. Wet etching typically does not provide the nanoscale resolution required for plasmonic applications; dry etching, on the other hand, also has its limitation in terms of plasma chemistry and the achievable size. Gold requires the chlorine chemistry [13], and is typically forbidden in etch chambers due to its ability to contaminate other materials [14]. The chlorine chemistry, in addition to generating toxic exhaust, is known to alter the properties of photoresist, pump oil, and so on, which would require special treatment. Silver also needs chlorine-based plasma [15]. Aluminum needs the combination of Cl_2 and BCl_3 [16, 17]. Unless the chamber is heated above 35 ^oC, $AlCl_3$ would deposit on the chamber wall and react with moisture into HCl, which attacks aluminum. Non-volatile derivatives from $AlCl_3$ or BCl_3 can also clog the system [17]. As for Cu, in the Caltech cleanroom it is directly banned in the metal plasma etcher to avoid chamber contamination. Even in the scenarios like Ag or Al, the etch resolution will be determined by intrinsic plasma parameters such as the ion angular distribution, which will be discussed in further detail in Section 2.1.3. In short, there is no precise etching control on the nanoscale for these metals in order to achieve the resolution required for many plasmonic applications. As a result, previous efforts relied on other techniques such as focused ion beam (FIB) [18], metal lift-off [19, 20], bottom-up synthesis [21], and so on. These methods, however, have various drawbacks such as being non-scalable, offering limited resolution, being

non-deterministic, and so on, which will be discussed in further detail in the associated sections. Due to the low speed and/or the mediocre resolution available for making a chip with these techniques, it would be difficult to fabricate plasmonic structures with various dimensions to scan the entire parameter space, or to confirm novel ideas from theories or simulations. Moroever, due to the inability of mass production, those chips can only stay in the laboratory as precious pieces of collection, instead of being used in various settings.

In spite of the relative difficulty of making these structures, the promising features of plasmonics have resulted in a great boom in the number of applications, including metamaterials [22, 23], optical nano-antennae [24], nonlinear optics [25], superlenses and hyperlenses [26, 27], plasmonics-assisted nano-optical tweezers [28], electro-optical modulators [29], and so on. Plasmonics is especially attractive in the fields of biomedical sensing due to its sensitivity to biochemical binding events and its wireless, non-invasive nature of optical readout. Various plasmonics-based biomedical sensing techniques have been proposed and demonstrated, including extraordinary transmission (EOT) [30], surface-enhanced Raman spectroscopy (SERS) [31], localized surface plasmon resonance [32], and so on. All would be great if only plasmonic structures could be mass-produced on the wafer scale.

Recently, Walavalkar *et al.* demonstrated a new method of fabricating plasmonic nano-apertures that can be applied to the entire wafer [33]. Instead of tackling plasmonic metals directly, Si structures were used as a template to define the nanoscopic variations on the chip. Owing to decades of high demand in the electronics industry, high-quality silicon wafers are now readily affordable and well-characterized. With the advancement of the electronics industry, various machines are now also available in commercial foundries to process silicon wafers in a large batch. Silicon as a starting point is therefore a promising alternative for the mass production of plasmonic chips, which will in turn enable the exploration of many scientific and engineering opportunities.

In this work, it is demonstrated that the hybrid approach of using Si as a template can lead to metal nanostructures for various plasmonic applications. The top-down designing and fabrication would allow the designer lots of freedom to decide where the plasmonic structures

should be located on a chip. Taking advantage of bottom-up physical processes, such as thermal reflow, an even better nanoscale precision can be further achieved that goes beyond the resolution of regular nano-lithography. This thesis is divided in several parts as follows: Chapter 2 describes the fabrication and measurement of extraordinary transmission (EOT) nano-apertures. The choices of various substrates and metals as well as EOT-based sensing are discussed. Chapter 3 focuses on surface-enhanced Raman spectroscopy (SERS); its fabrication is one good example illustrating the true power of the hybrid approach. The measurement and detection are reported for several biomedical-relevant molecules: thrombin, tracheal cytotoxin (TCT), and ethyl mercapatan. In Chapter 4, the efforts are discussed regarding how to integrate the chips into the system level so that they can be user-friendly outside of a laboratory; after all, one important goal of mass-producing plasmonic structures is to enable a wider audience of users to benefit from their potential in biomedical sensing. Finally, Chapter 5 outlines the outlook for future work, so that both designers and users can have more choices of available nanostructures and more straightforward operation of sensing and detection.

Chapter 2

Extraordinary Transmission (EOT)

Extraordinary transmission (EOT) is a phenomenon that electromagnetic energy passes through sub-wavelength apertures on metal at a much larger intensity than predicted by classical theories. According to these theories, such as those by Bethe [34] and Bouwkamp [35], the far-field transmission would diminish rapidly when the aperture size shrinks further and further into the sub-wavelength dimension; for a simple circular aperture at a radius of r, the transmitted power would be proportional to $(r/\lambda)^4$ [6]. In 1998, however, optical EOT was first discovered by Ebbesen *et al.* [36], and since then this seminal paper has been cited for more than 6,100 times. When the sub-wavelength apertures are arranged in some specific patterns, the transmission can be several orders of magnitude stronger than calculated from the aforementioned theories. Later on, EOT was also demonstrated for millimeter [37] and THz waves [38].

Several models have been proposed to explain the EOT phenomenon, including constructive interference [39], evanescent wave coupling [40], antenna effects [41], coupled localized modes [42], and so on. In the regime of optical wavelengths, EOT is also facilitated by plasmonics [6, 33, 39, 41, 43, 44]. Like other plasmonic phenomenon, EOT is highly geometry- and wavelength-dependent, which is a very promising feature for photonic applications on a nanoscopic scale without resorting to bulky optical components like filters. It can also depend on the incoming wave vector, such as the orientation of polarization or the angle of incidence, which provides additional degrees of freedom for various applications. In recent years, as a result, EOT-based sensing techniques have been a popular research area [30, 45, 46] for several reasons. As discussion in Chapter 1, the change of dielectric constants around the metal-dielectric interface would readily influence the plasmonic response, which would in turn affect the optical readout. Binding events, for example, can be measured in this way [47]. Furthermore, since optical waves have to travel through these tiny tunnels of metal, the signal-to-noise ratio can be greatly improved if the bio-molecules of interest can be placed right at the exit of the tunnels.

The options for making EOT nanostructures, however, have been very limited so far. Most of the work has resorted to focused ion beam (FIB) [18, 36, 48], which is a time-consuming and non-scalable process. Since most of the FIB machines do not come with a laser-interferometer sample stage, there would be precision issues when patterns have to be spread over a large area. The lack of a laser-based heightmeter also prevented precise, automated adjustment to the variation of topology or tilt of the wafer to be written. The ion beam tail further limits the feasible milling thickness; like laser Gaussian beams, the smaller the ion beam is focused, the faster it diverges, which can be seen in Fig. 2.1. As a result, when the metal thickness exceeds a certain level, the milled cross section would be in a pronounced shape of funnels, which limits the design flexibility. In addition, common FIB machines use Ga ions as the source, which in effect would dope the areas around the milled apertures [49]. These impurities would surely affect the overall metal dielectric constant, and the device performance would deviate from the design and simulation in unforeseen manners. Argon milling [46], while a faster process, has very little etching selectivity and therefore can only achieve a very poor aspect ratio. Sputtered material may also re-deposit on the chip surface. Another option would be metal lift-off [20]. For good lift-off results, however, typically the metal should not exceed 1/4 of the thickness of the patterning polymer, so again high-aspect-ratio EOT structures are unavailable. Sometimes metal deposition onto nano-spheres was used [45], but this approach seriously limits the design freedom regarding the available shapes and periodicity of the nano-apertures.

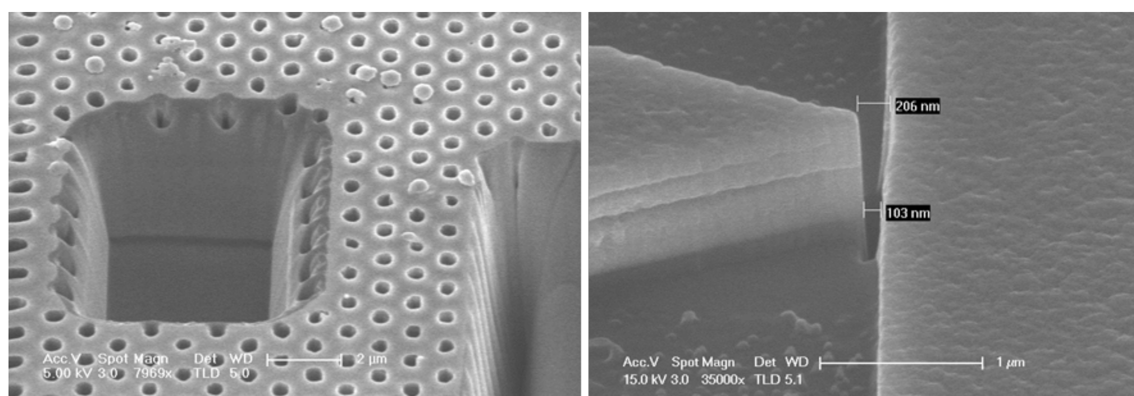

Figure 2.1 Examples of slanting sidewalls of FIB cross sections.

Some researchers were attempting with other top-down approaches for fabricating EOT nanostructures, in which dielectric materials [30] or e-beam resists [50] were shaped for metal deposition, so far with limited success. One big issue is that the dry etching process for shaping dielectric structures is limited by the same constraints as etching plasmonic metals directly, which was discussed in Chapter 1, and there are certain barriers regarding resolution and aspect ratios that these approaches cannot cross. The metal thickness was also quite limited, including another approach of direct nanoimprinting on Au films [51]. This issue was appropriately addressed in the recent work of Walavalkar *et al.* [33]; the ability to etch Si nanostructures with a high aspect ratio and repeatable precision opens a new door for EOT nanofabrication.

In this chapter, the nanofabrication steps are first discussed and explained for their benefits, along with their compatibility for wafer-scalable production in commercial semiconductor foundries. It is then demonstrated that in addition to silicon substrates, silicon-on-sapphire (SOS) and silicon-on-glass (SOG) versions are also achievable. Furthermore, the metal layer can be either Au or Al, with possibilities of extending to other types of metals with similar fabrication steps. EOT behaviors are then characterized; since incident wave vectors are important in plasmonics, it is shown that the spectral transmission would be different at different angles of polarization. Comparisons between Au and Al counterparts are also made. Towards highly-sensitive fluorescence-based EOT assays, photo-uncagable functionalization on SOS chips is demonstrated. Some part of the contents in this chapter was presented in the 2014 IEEE EMBS Micro and Nanotechnology in Medicine Conference [52].

2.1 Fabrication

This section reviews the fabrication steps and options for making the EOT nano-apertures. Individual explanations are available from electron beam lithography to XeF_2 undercut etching, followed by a brief summary and sequence illustration. It should be emphasized that all the fabrication methods have their counterparts in commercial semiconductor foundries, and therefore can be readily converted for wafer-scale production, which is one of the key points of this work.

2.1.1 Electron Beam Lithography

Most of the fabrication was done at the Kavli Nanoscience Institute (KNI) at Caltech. To obtain the nanoscale resolution required for optical extraordinary transmission, the tool of choice at KNI is the Leica EBPG 5000+ system, where EBPG stands for electron beam pattern generator. Electron beam lithography, however, is chosen simply because of its flexibility for fast proto-typing; in commercial semiconductor foundries, immersion photolithography can easily achieve the patterning resolution required for these structures since the critical dimensions here are greater than 30 nm, which is well within the capability of such machines, and the whole fabrication can be readily done in a wafer-scalable, mass-produced manner.

For the convenience of subsequent steps, poly(methyl methacrylate) or PMMA was mainly used for the electron beam exposure. PMMA is a positive-tone e-beam resist with good sensitivity and consistency, and it provides sufficient resolution for the intended structures. The wafer is first cleaned with acetone and isopropyl alcohol (IPA) to remove any possible organic residues on the surface. PMMA 950 A4 from MicroChem is then spin-coated on the wafer; a typical recipe is 4000 rpm for 1 minute, which yields a thickness of ~200 nm. After being baked at 180 ^{o}C on a hot plate, the wafer is e-beam exposed by the EBPG system, followed by development in the mixture of methyl isobutyl ketone (MIBK) : IPA = 1 : 3. The development time is related to the e-beam exposure dose, and a typical recipe is 1 minute of development for a dose of 1350 $\mu C/cm^2$.

2.1.2 Deposition and Lift-Off of Hard Mask

PMMA, while being a good e-beam resist, does not survive plasma etching very well and therefore is a poor choice of masking material. Another type of e-beam resist, the negative-tone hydrogen silsesquioxane (HSQ) like XR-1541 from Dow Corning, is more robust against plasma etching but still not enough for the depth of etching to be achieved in these applications. While metals fare pretty well in plasma etching, on the other hand, they are not allowed in the high-quality etch chambers at KNI. To meet all these requirements, aluminum oxide (Al_2O_3) or alumina is a good choice since it is a dielectric material and it provides excellent etching selectivity against silicon in various etching chemistry. Compared with some

types of metals, the lift-off results also preserve the nanoscale resolution of e-beam writing with very high fidelity. A comprehensive study of alumina as a silicon-etching mask can be found in [53].

Alumina can be either reactively sputtered or evaporated onto the wafer after PMMA development. For sputtering, typically argon is used with oxygen injection to achieve stoichiometric deposition from an aluminum target. The amount of oxygen has to be carefully calibrated, and may differ a lot from machine to machine due to different gas inlet configurations. For the two sputtering machines available at KNI, as an example, one requires 13 sccm of O_2 flow and the other only 1 sccm, while the Ar flow is the same amount of 100 sccm for both. If too little oxygen is provided, the film will retain some of the metallic properties of aluminum; if too much, the target will be "poisoned" and no sputtering would result [54]. If the aluminum target was newly exposed to the atmosphere (due to target swapping, etc.), it is a good practice to do some pre-sputtering to eliminate the native oxide built up on the aluminum surface. On the other hand, alumina can also be evaporated onto the wafer, such as by an e-beam evaporator. Evaporated alumina tends to be even more robust than the sputtered one, but it is also usually more difficult to lift off.

PMMA dissolves very well in dichloromethane (DCM), which is a better choice for lift-off than acetone. Sometimes sonication is needed to facilitate lift-off, especially for evaporated alumina. If things go wrong, such as poor lift-off or change of plans, alumina can be removed in heated phosphoric acid (H_3PO_4). A few minutes are sufficient already for the removal. Although buffered hydrofluoric acid (BHF) is supposed to remove alumina [55], its effect was not good enough during actual tests at KNI.

2.1.3 Etching

For anisotropic etching on the nanoscale, wet chemistry is no longer feasible and plasma etching (i.e., dry etching) is called for. Dry etching was first developed as the reactive ion etching (RIE), as shown in Fig. 2.2, and over the years it has become a versatile and reliable tool. In the RIE configuration, however, the total amount of input power determines the level of plasma ionization as well as the forward driving power (and therefore the DC bias), and

hence these quantities are coupled in the etching process. In order to have more flexibility for the required etching precision on the nanoscale, the other configuration of inductively-coupled plasma (ICP) is preferred here. Briefly speaking, in the ICP-RIE configuration the plasma is ionized by one power source, typically at 13.56 MHz, while the forward driving is achieved by another source for capacitively-coupled plasma (CCP). In this manner the ion density and the incident ion energy can be independently tuned, and the etching recipe can therefore be designed to be more chemical (i.e. relying on ion-level chemical reactions) or milling (i.e., assisted by the bombarding effects from the incident ion energy). A thorough study on the ICP-RIE etching of silicon can be found in [53].

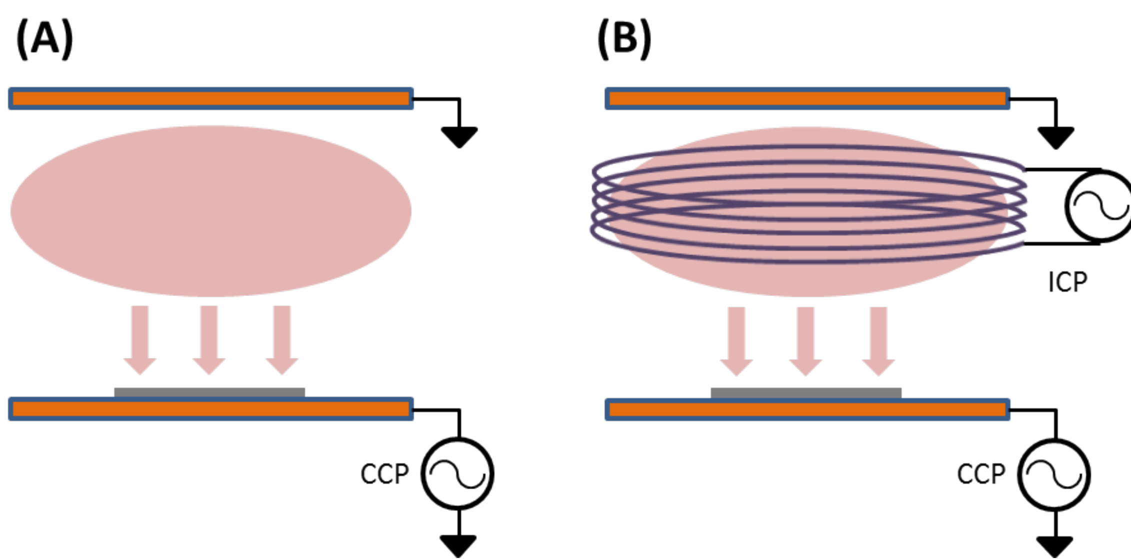

Figure 2.2 Schematic diagrams of (A) RIE etching and (B) ICP-RIE etching.

Pseudo Bosch is the most important etching chemistry in this work. The namesake comes from the same use of gases as the Bosch plasma etch, in which sulfur hexafluoride (SF_6) and octafluorocyclobutane (C_4F_8, also commonly known as halocarbon C318 among gas vendors) are employed. In the traditional chopping Bosch process, one cycle consists of an SF_6 step for etching and another C_4F_8 step for passivation [53]; in the pseudo Bosch mechanism, on the other hand, both SF_6 and C_4F_8 are simultaneously present all the time, and hence the term "pseudo" in the name. Using silicon as an example and referring to Fig. 2.3 (A), at one

moment the C_4F_8 component in the plasma creates a passivation layer everywhere on the wafer. The forward power of the plasma, however, has the ion milling effect to remove the regions directly facing the plasma while keeping the passivation on the sidewalls in place, resulting in the configuration of Fig. 2.3 (B) at the next moment. The SF_6 component in the plasma can now chemically etch the exposed areas of silicon. At the very next moment, the whole surface is passivated again by C_4F_8 and the scenario goes back to Fig. 2.3 (A); depending on the level of C_4F_8 in the plasma, the newly exposed sidewall regions will be passivated at a different level, which will affect how easily they will be milled away by the ion angular distribution at the next moment [53]. With less passivation, the subsequent etching will result in an undercut; with more passivation, on the other hand, the silicon at the base of the structures will be better protected and will start to "bulge out." The reason of using the ICP-RIE configuration is now apparent, since now the plasma concentration for passivation and etching can be controlled independently of the plasma forward power, which in turn determines the ion milling efficiency and the ion angular distribution [53].

From the previous discussion it is apparent that the pseudo Bosch etch offers many advantages over the traditional chopping Bosch for the requirement of nanoscale precision.

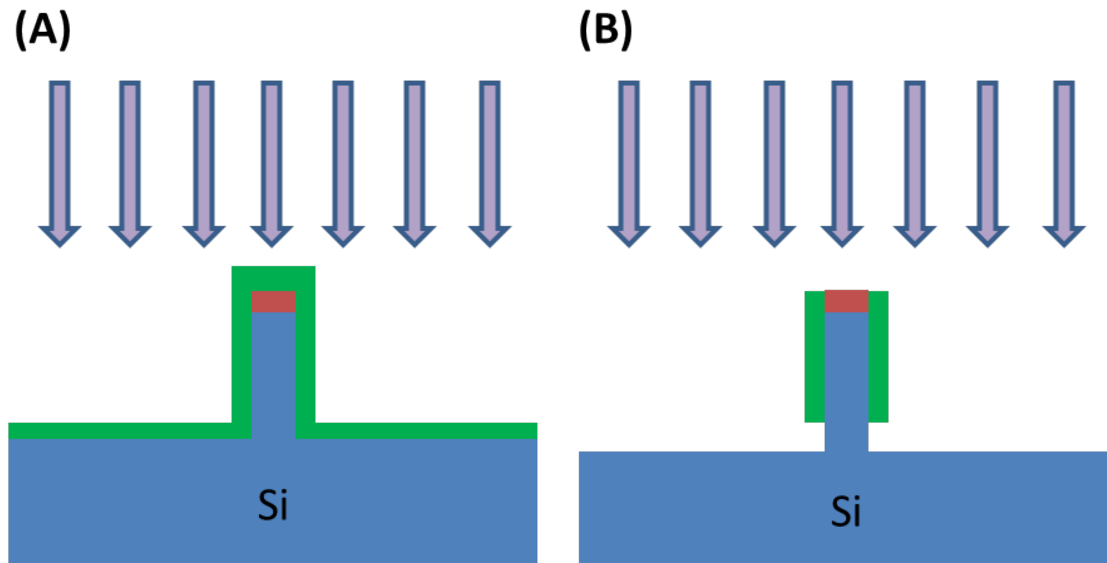

Figure 2.3 (A) Pseudo Bosch process, right before the passivation layer in the forward direction is removed by the ion milling effect; (B) the SF_6 component in the plasma can now etch the exposed areas of silicon. The green color denotes the passivation layer of C_4F_8, and the red color means the mask.

The sidewalls can be etched smoothly in the pseudo Bosch, while scalloping is unavoidable in the chopping Bosch [53], which, among other adverse effects, limits how small the nanoscopic features can survive the etching without falling apart due to excessive undercut from the scalloping. By tuning the parameters such as the gas composition and the input power, the sidewalls can be chosen to be slanting inward (Fig. 2.4 [A]), etched vertically (Fig. 2.4 [B]), or slanting outward (Fig. 2.4 [C]), which are well illustrated here with the scanning electron microscope (SEM) images. Furthermore, if the ratio between SF_6 and C_4F_8 is adjusted in the middle of the process, 3D sculpting can be achieved for the etched structures [33, 54], which can be a useful feature in some applications.

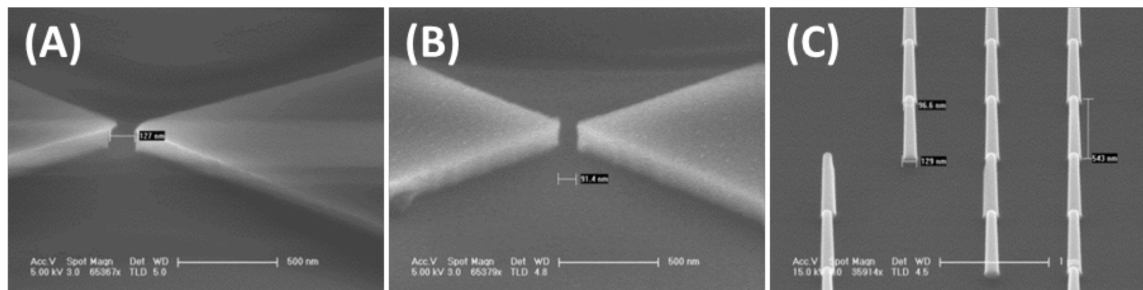

Figure 2.4 Control of the sidewall angle from the pseudo Bosch etching to be (A) slanting inward, (B), etched vertically, or (C) slanting outward.

The choice of lithography and etching is a powerful combination that allows great flexibility for the top-down designing process. With Al_2O_3 as a robust hard mask and with pseudo Bosch as a tunable tool, arbitrary shapes with a high aspect ratio can be etched on silicon at a high precision on the nanoscale. Figure 2.5 shows some examples of the possible structures that can be easily fabricated on the wafer scale with this approach.

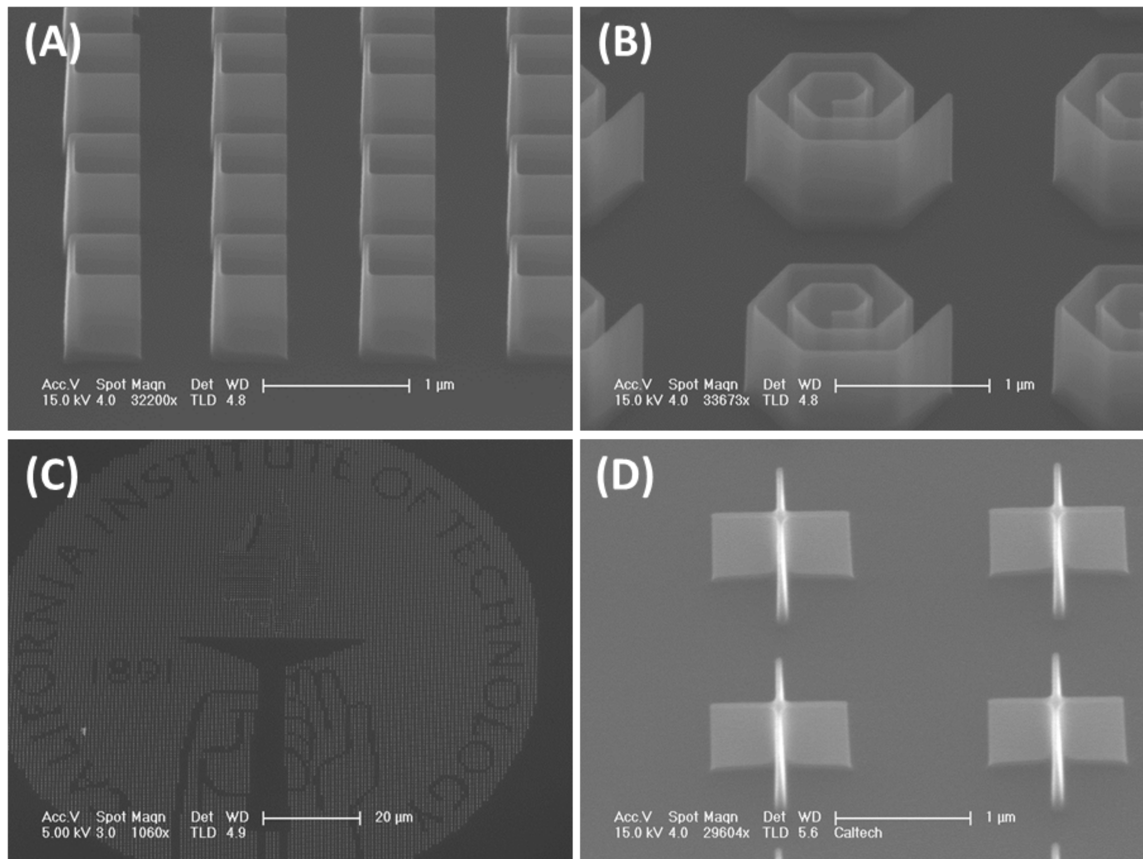

Figure 2.5 Examples of arbitrary shapes made possible by the top-down process of lithography and etching.

2.1.4 Thermal Oxidation

While silicon is a good candidate for providing a template of 3D structures, its bandwidth of 1.12 eV means wavelengths shorter than ~1100 nm will be absorbed in this material. In order for the nano-apertures not to be highly lossy due to absorption in silicon, thermal oxidation is called for to convert the etched structures into silicon dioxide, which is transparent well into the ultraviolet (UV) regime. Furthermore, if thermal treatment is to follow after Au deposition, formation of Au-Si eutectic would occur at a temperature greater than ~400 ^{o}C [56], and therefore silicon should not be exposed to gold in the beginning. Some other metals like Al would also eutectically dissolve into Si when the temperature is greater than ~577 ^{o}C even if high vacuum can be maintained during the annealing process [57]. For EOT

applications, the SiO_2 nano-apertures also facilitate subsequent functionalization since various techniques are available to attach bio-molecules to glass [58, 59].

Two options are available for thermal oxidation: dry and wet. In the former, oxygen is supplied to the furnace for the oxidation process; in the latter, the O_2 flow goes through a flask filled with water before entering the furnace, thus carrying H_2O vapor along the way. The H_2O molecules diffuse faster than the bulkier counterparts of O_2 through the existing oxide layer, and therefore wet oxidation offers a much higher speed than the dry alternative, although at a cost of more dangling bonds, a lower oxide density, and so on [60]. In this work, eight hours of dry oxidation at a temperature around 1000 ^{o}C would be sufficient. Around 240 nm of oxide would come out of the furnace for this time duration, which is more than enough to turn the 3D nanostructures thoroughly into silicon dioxide. If a thick layer of oxide is desired, it is optional to turn the etched structures into high quality of oxide by dry oxidation first, followed by wet oxidation to increase the layer thickness into the substrate.

2.1.5 Metal Deposition

Two options of metal deposition were used for this work: sputtering and evaporation. Both worked well for the two choices of metals in this work, Au or Al, depending on the structures intended to be made.

Sputtering offers the benefit of conformal coating, which is especially useful if the nanostructures are 3D-sculpted during the pseudo Bosch etch. It is also a good option when the nanostructures are sparse enough for thermal reflow of gold to be successful; more discussion on the reflow process can be found in Section 3.1.1. The sputtering of Au was done at a home-built machine at KNI maintained by the Scherer Group, nicknamed McGill, with an argon flow of 100 sccm. First, an adhesion layer of Ti was sputtered at 30 mTorr and 175 W for about 2 minutes, which deposits ~5 nm of titanium as a wetting layer for the subsequent Au sputtering. Gold was then sputtered at 10 mTorr and 80 W for a few minutes, depending on the desired final thickness. In this work the Au thickness ranged from 150 to 200 nm approximately. Aluminum can also be sputtered by either the McGill system or the

other one made by a company called TES. A typical recipe is 100 sccm of Ar at a pressure of 10 mTorr and a power setting of more than 300 W.

Evaporation, on the other hand, has very good directionality and sidewall deposition can be minimized; this is a very desirable feature when thermal annealing could not drive the metal satisfactorily away from the sidewalls when the pattern is too dense, or when the nanostructures are of a shape that cannot be mechanically broken well without specialized apparatus. The process of mechanical snapping will be discussed in the next section. In this work e-beam evaporators were used for the deposition, although thermal evaporators can also be an option if the chamber can accommodate two targets so that Ti and Au can be evaporated sequentially without breaking the vacuum.

To obtain the desirable nano-apertures for extraordinary transmission, however, additional factors have to be taken into consideration than in sputtering. The angular distribution in evaporation, though small, is still nonzero and can result in intolerable sidewall deposition that makes subsequent processing more difficult. One prominent parameter is the height of nanostructures before the evaporation. If the structures are too tall, they will "shadow" the regions around the base by blocking the small angular contribution from the other side that could have otherwise reached the spot. The result would be shapes of slightly upward-facing funnels for the fabricated apertures, which may not be desirable in some applications. Figure 2.6 shows the different results from the same deposition run in the CHA machine on two chips of different etching depth. In Figs. 2.6 (C) and (D), the structures are much taller than those in (A) and (B), and the shadowing effect is therefore much more obvious since higher structures are more efficient in blocking; the sidewalls also collected more deposition along the way.

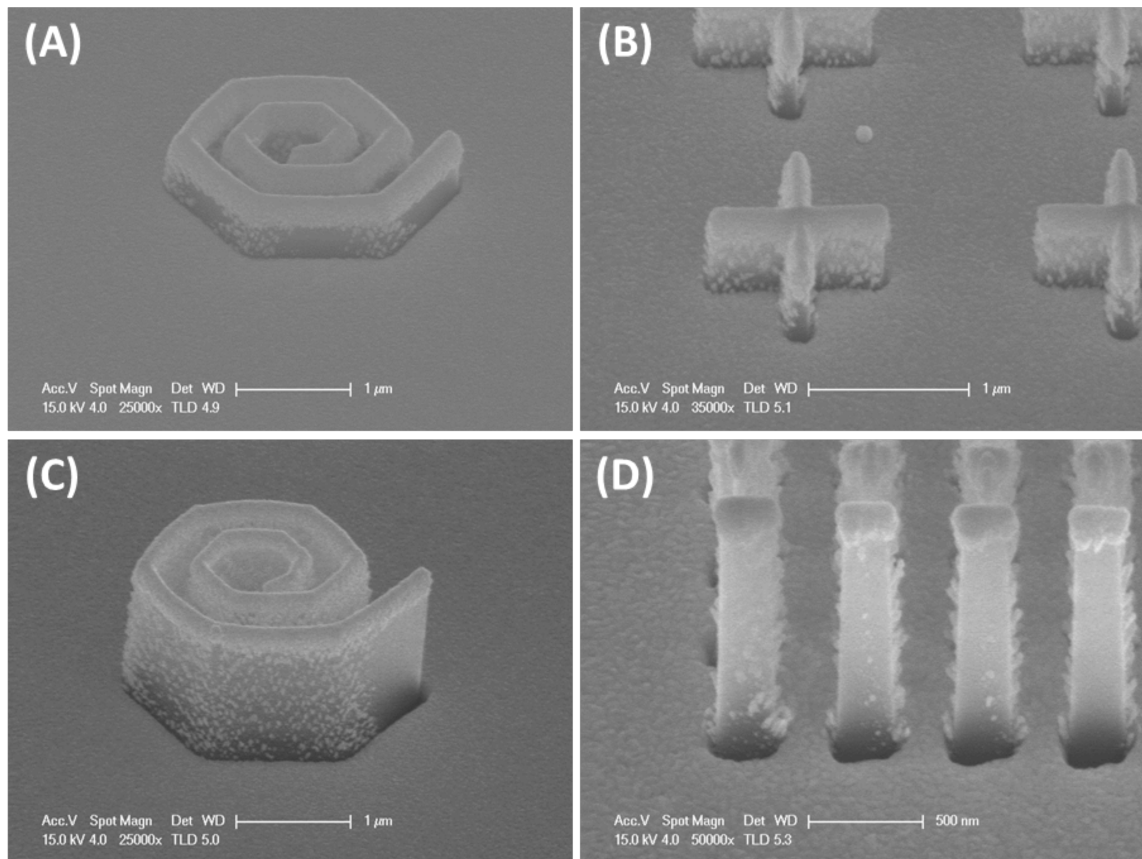

Figure 2.6 Results of evaporation from the CHA machine on chips of different etching depth. The structures in (A) and (B) were shorter than those in (C) and (D), while the thickness of the Au deposition was the same.

Due to its high directionality, evaporation can achieve something that cannot be done in sputtering: angled deposition by tilting the chip orientation. This is another issue to consider, however, when the sidewall deposition has to be minimized. At KNI there are two e-beam evaporators, one manufactured by the TES and the other by CHA Industries, Inc. The CHA model has a domed wafer loader that conforms to the angular distribution of evaporated metal, so that the metal vapor will impinge on the chips at a right angle. The wafer loader of the TES machine, however, is planar in shape. As a result, unless the chip sits right above the crucible of the TES machine and the table rotation is turned off during the deposition, more sidewall deposition is anticipated from this machine. This is indeed the case, as seen in Fig. 2.7.

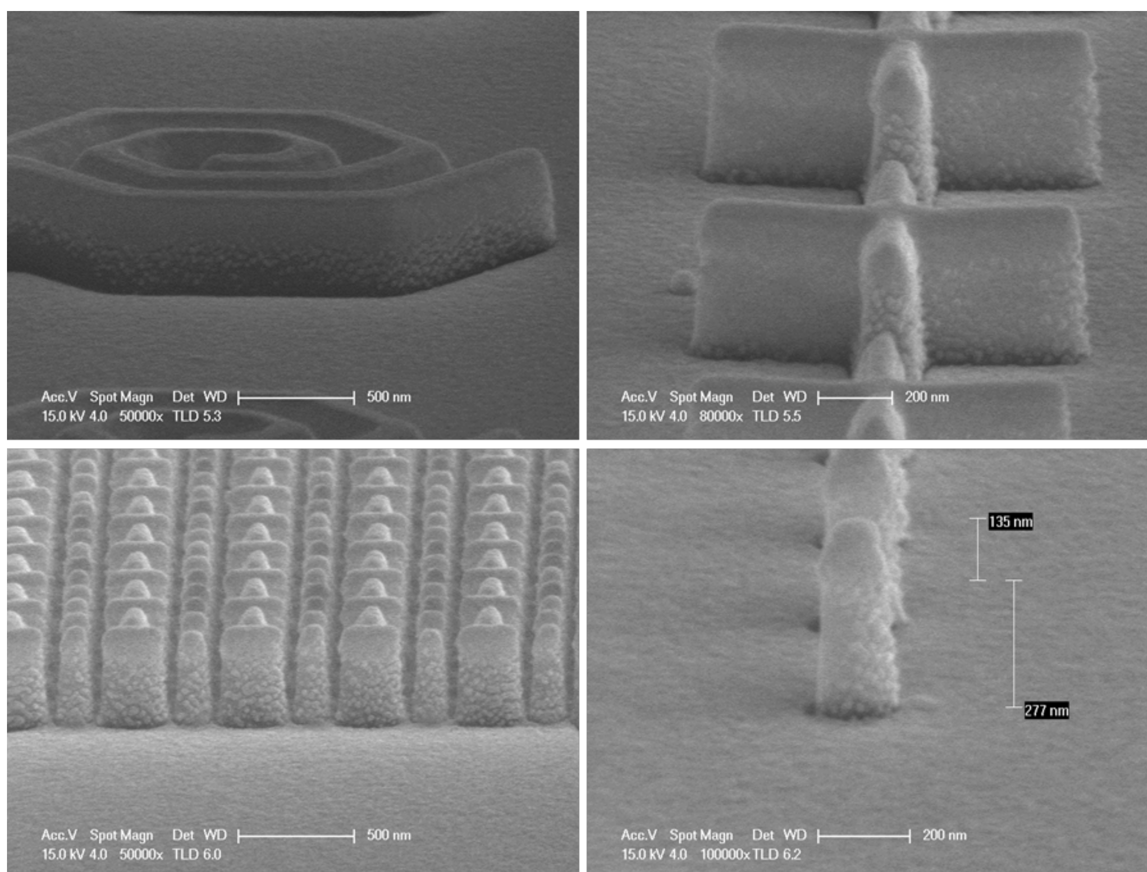

Figure 2.7 Results of evaporation from the TES machine; the sidewall deposition was more serious than in CHA.

If for any reason the gold layer has to be removed for another deposition, the gold etchant TFA from Transene does a good job without affecting the nanostructures since it is based on potassium iodide (KI). For extreme purists who are concerned about the thin adhesion layer of Ti, a very quick dip in BHF would be sufficient since BHF attacks Ti very fast [55]. Another option is aqua regia, which is a mixture of nitric acid and hydrochloric acid with an optimal molar ratio of HNO_3 : HCl = 1 : 3. It should be noted that since commercial nitric acid and hydrochloric acid are commonly available at a w/w concentration of 70% and 37%, respectively, this translates to a volume ratio of approximately 1 : 4. The specifications of commercially-available HNO_3 and HCl are listed in Table 2.1. Aqua regia does not attack silicon dioxide, and will leave the nanostructures intact.

Acid	Molecular Weight	Density (g/cm^3)	Concentration w/w
HNO_3	63.01	1.42	68 - 70%
HCl	36.46	1.19	36.5 - 38.0%

Table 2.1 Specifications of commonly-available nitric acid and hydrochloric acid.

2.1.6 Removal of Protruding Nanostructures

Depending on the choice of metal sputtering of evaporation, which in turn depend on the type of nano-apertures to be fabricated, two options are available for removing the nanostructures above the chip so that the apertures can be exposed. For scenarios in which sputtering and thermal reflow (see Section 3.1.1) are sufficient, a thin layer of polymer such as PMMA 950 A2 is coated on the chip in order to protect the regions without nanostructures. The nanostructures can then be mechanically broken off by scrubbing the chip with a Q-tip [33]. On this nanoscale, Au provides tenacious connection that defies mechanical scrubbing if there is still residual gold on the sidewall, whether from the evaporation (like Fig. 2.7) or from insufficient thermal reflow (like Fig. 2.8). A specialized machine of chemical-mechanical planarization (CMP) may be able to address this issue due to its ability of mechanical polishing, but unfortunately such a machine is not available at KNI for now. For high-volume production in commercial foundries, the CMP machine is anticipated to polish away the nanostructures on the wafer scale.

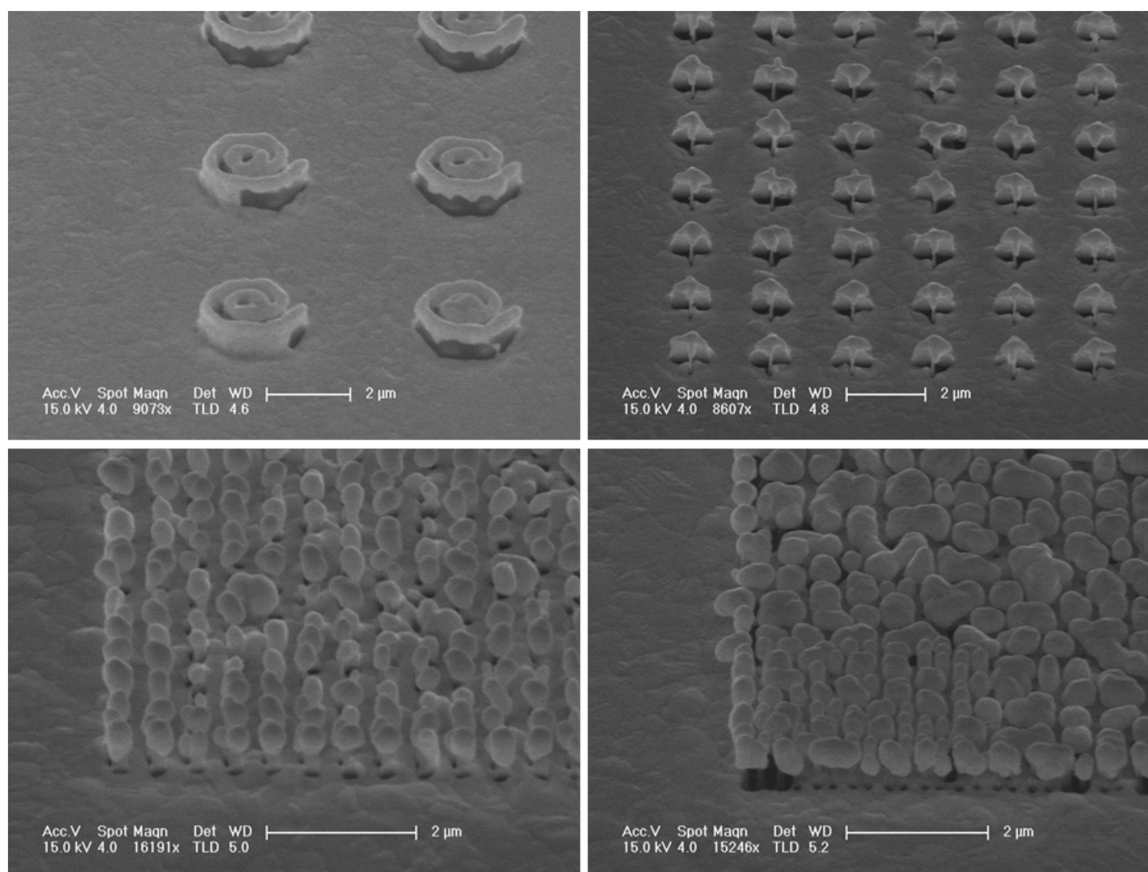

Figure 2.8 Insufficient thermal reflow of Au due to the shape and/or density of nanostructures.

When evaporation is called for due to the shape and/or density of nanostructures, another approach is needed to remove the nanostructures since thermal reflow does not drive away the small residue of sidewall deposition, as shown in Fig. 2.9. In this case mechanical snapping would not work well, and the etching method is preferred. First, a layer of e-beam or photoresist is spin-coated on top of the chip; the thickness is not critical here, although it is desirable for the thickness to be larger than the height of nanostructures to avoid the complexity of dealing with sidewall coverage, etc. Oxygen plasma, either from a barrel asher or from an RIE machine, can then be employed to remove the resist layer to the desired level of height and expose the top of nanostructures, as shown in Figs. 2.10 (A) and (B). A quick immersion of the chip in the TFA gold etchant would be sufficient to remove the Au deposition on top of the nanostructures; the results are shown in Figs. 2.10 (C) and (D).

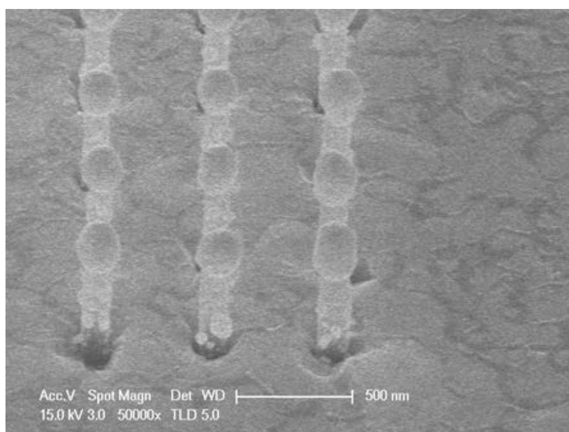

Figure 2.9 Result of thermal reflow from a chip with evaporated Au.

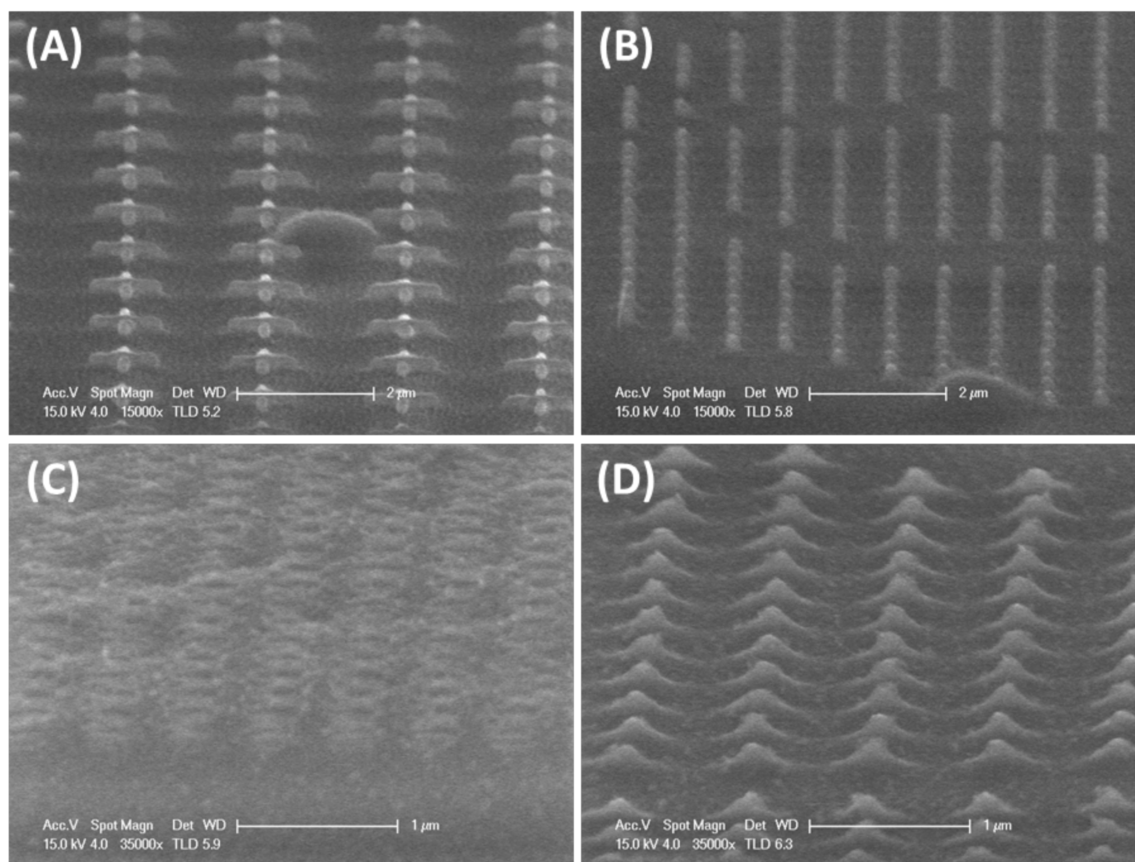

Figure 2.10 (A) and (B) show the revealed top of nanostructures after the resist layer had been ashed to the appropriate height; (C) and (D) show the results right after the TFA Au etch.

Here the chip was further immersed in BHF to remove the main body of nanostructures, which are made of silicon dioxide. With controlled time of etching, the wet chemistry can remove the nanostructures without going all the way through the oxide layer underneath the general region of the gold layer. Figure 2.11 shows some examples of fabricated nano-apertures on a gold layer at a thickness of 200 nm.

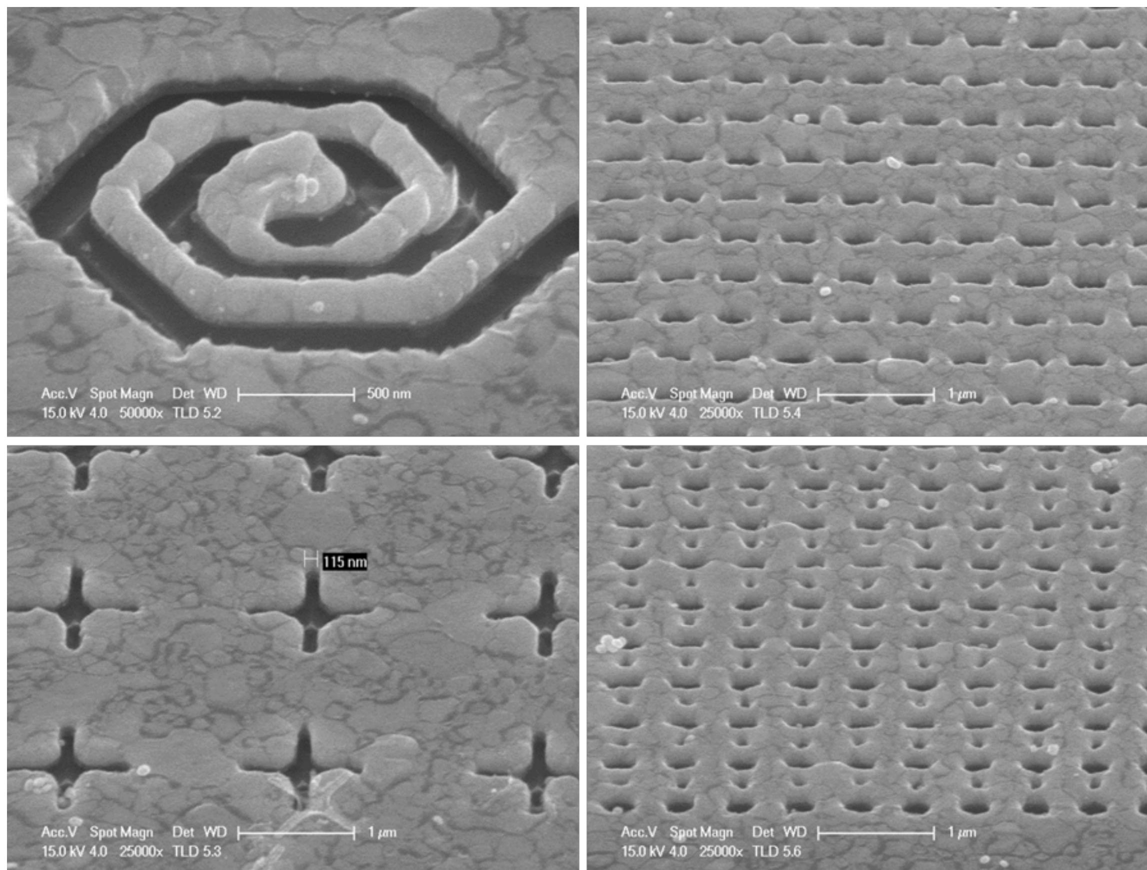

Figure 2.11 Fabricated nano-apertures on a 200 nm layer of Au.

Theoretically this etching approach can also be used to treat chips with sputtered gold; in reality, however, several technical issues stand in the way. The TFA gold etchant converts gold into gold iodide via

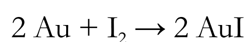

$$2\ Au + I_2 \rightarrow 2\ AuI$$

while AuI dissolves better with the presence of KI. The TFA etch would discolor the gold surface and make it look somewhat reddish like copper, however, probably due to the finite

solubility of AuI that does not immediately go away and would adhere to the surface. This would not be desirable for the fabrication, where the residue of AuI may introduce unwanted effects. Aqua regia, on the other hand, was found to attack the adhesion layer of Ti extremely fast, and the entire metal layer would peel off the chip very soon.

2.1.7 Photolithography and Substrate Opening

Photolithography also played a supporting role in the fabrication. To define large areas, for example, it would be more efficient to produce a mask first to save time in the subsequent exposure. This can be done at KNI through either the Heidelberg DWL 66 system or the EBPG e-beam writer. In the former case, the system parses the computer-aided design (CAD) file and directs a laser head to expose the photoresist layer coated on a mask, hence the name of direct-write laser for DWL. If a bright field mask is desired, the complimentary dark field patterns can be transferred to another mask coated with image reversal photoresist such as AZ 5214 E from MicroChem. This is because the Heidelberg machine at KNI uses a HeCd laser at 442 nm, while AZ 5214 E has to be exposed at a wavelength from 310 to 420 nm. When the EBPG system is used instead, a layer of e-beam resist is coated on the mask instead depending on the type of mask to make. When a dark field mask is desired, PMMA is a good choice for this purpose. For bright field mask, a negative e-beam resist like ma-N 2403 from MicroChem can be convenient. Another type of negative e-beam resist, HSQ, is not appropriate in this scenario since it has to be removed with an oxide etchant such as BHF, which would attack the mask substrate as well, unless special masks not made of glass are utilized. On the other hand, ma-N 2403 can be removed either by oxygen plasma ashing or by Nano Strip from Cyantek (a commercial mixture of sulfuric acid and hydrogen peroxide compounds), and neither method would affect the glass substrate itself. After the patterns are defined and developed on the mask, a chrome etchant like CR-7S from Cyantek is used to remove the chrome layer in the exposed regions. Based on perchloric acid, such an etchant would not compromise photoresist, PMMA or ma-N 2403 in the time scale required to etch away the chrome layer. Finally the resist layer is stripped by either oxygen plasma or wet chemistry.

In the fabrication of EOT nano-apertures on silicon, photolithography was used to define the backside opening so that the silicon region right below the apertures can be removed subsequently for light to pass through. This can be done with the MA/BA 6 series mask aligner from SUSS MicroTec, which comes with video cameras on both the top and the bottom sides. Briefly speaking, first an image of the photomask is captured with the bottom video camera and displayed on the monitor. The chip is then placed facing down on a transparent holder; with the help of the bottom video camera and the photomask image on the screen, the chip can be aligned to the desired location. The photoresist layer on the backside of the chip is then exposed and developed as usual.

The backside region defined by photolithography was first exposed to BHF so that the oxide layer can be etched away. A silicon etcher with xenon difluoride (XeF_2) could now be used to remove the substrate region below the nano-apertures:

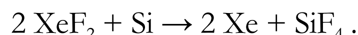

$$2\,XeF_2 + Si \rightarrow 2\,Xe + SiF_4\,.$$

Both Xe and SiF_4 are gaseous at room temperature and can be pumped away. The process has a very high etching selectivity of silicon against photoresists or silicon dioxide [55], so the oxide layer below the metal can serve as a natural etch stop. There are a few cautions of using the XeF_2 system, however. After the chips are loaded in the system, it is a good practice to purge the chamber with a few cycles of dry nitrogen in order to remove the moisture in the air, or otherwise hydrofluoric acid would be generated via [61]

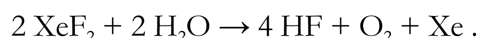

$$2\,XeF_2 + 2\,H_2O \rightarrow 4\,HF + O_2 + Xe\,.$$

While this would not render the chips immediately useless, in the long run it would however etch the glass of the vacuum viewport, making it blurry as a piece of ground glass, as shown in Fig. 2.12 (A). In the typical etching conditions of the KNI XeF_2 system, on the other hand, gold would be affected by the XeF_2 vapor and leave dissoluble residues in the chamber [54], which can be seen in Fig. 2.12 (B). It is therefore advised to remove the front side resist layer only after the XeF_2 etching is done. Now that there is only a thin membrane in the regions of the nano-apertures, oxygen plasma ashing is a better option in this case.

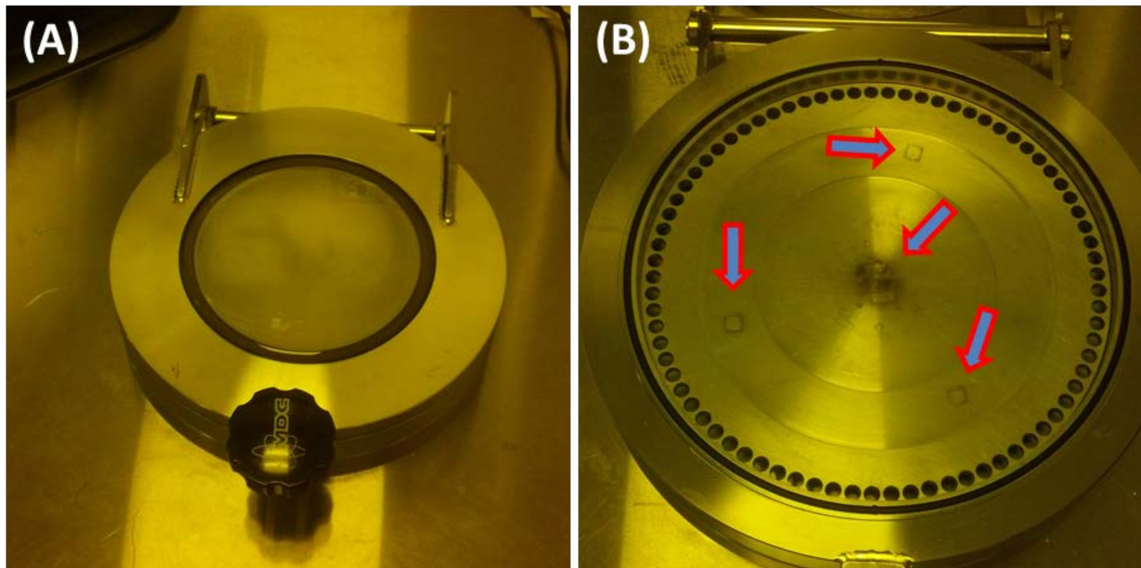

Figure 2.12 (A) Blurry vacuum viewport of the XeF_2 etcher; (B) residues from chips with Au inadvertently placed in the chamber by previous users.

The fabrication sequence for the sputtering approach is illustrated in Fig. 2.13. In (A), Al_2O_3 was deposited and lifted off after e-beam lithography, which served as the pseudo Bosch etch mask in (B). After thermal oxidation as in (C), Au was sputtered as in Fig. 2.13 (D) and annealed into the configuration as in Fig. 2.13 (E). After the protruding nanostructures were removed, the Si region below the nano-apertures was etched away with BHF and XeF_2 following backside-aligned photolithography, and the front side resist layer was stripped with oxygen plasma. The nano-apertures, now as shown in Fig. 2.13 (F), would then be available for measurement.

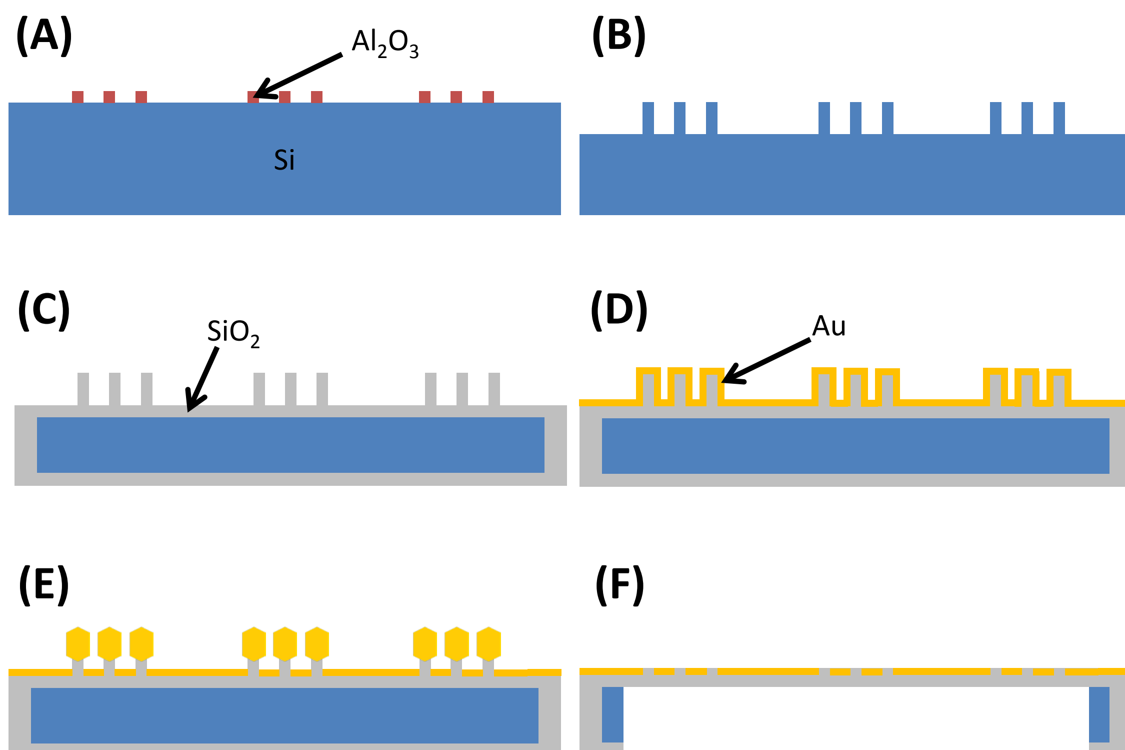

Figure 2.13 Fabrication sequence of nano-apertures for EOT on silicon for the sputtering option.

For the evaporation approach, the fabrication sequence is illustrated in Fig. 2.14. A resist layer was first coated on top after the evaporation step, as shown in Fig. 2.14 (A), which could be brought down to the desired level by oxygen plasma, as depicted in Fig. 2.14 (B). The Au region on top of nanostructures was first etched away with the TFA etchant, resulting in structures like Fig. 2.14 (C), and the nanostructures could be etched to the desired height with BHF by controlling the etch time, as shown in Fig. 2.14 (D). In Fig. 2.14 (E) the resist layer was already stripped, and following the same procedures for removing the Si region below nano-apertures, the device would be ready for measurement, as shown in Fig. 2.14 (F).

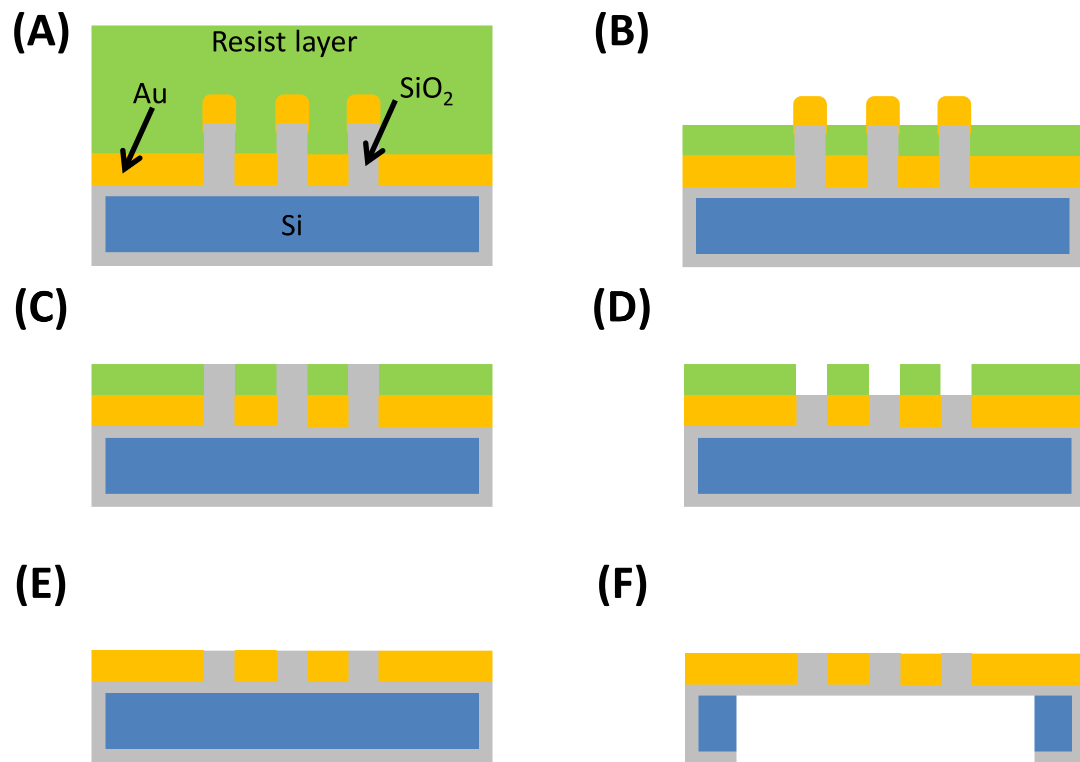

Figure 2.14 Fabrication sequence of nano-apertures for EOT on silicon for the evaporation approach.

2.2 Choices of Substrates and Metals

While silicon as a substrate is an inexpensive and well-studied option, its lack of transparency in the optical wavelengths requires the opening of the substrate below the regions of interest, as already described in the previous section. When further treatment is applied on the chip, the fragile membrane is prone to breaking, sometimes lowering the yield to unacceptable levels. Here it is shown that the same fabrication principles can be done on silicon-on-sapphire or silicon-on-glass chips with the same successful results.

On the other hand, Au has been the example of metal deposition in the previous sections, but it is not the only choice. Aluminum is shown to be an alternative option here, with other metals equally possible for future work based on the same approach.

2.2.1 Silicon-on-Sapphire Substrates

Silicon-on-sapphire (SOS) was initially used in the electronics industry as part of the silicon-on-insulator (SOI) development, in which the goal was to block the leakage currents in the substrate and the cross-talking between transistors through the substrate [62]. The superb optical and chemical characteristics of sapphire, however, make SOS chips a good candidate for EOT chips. Sapphire is transparent in the optical regime, very stable in various wet chemistry, and mechanically robust. One downside is that due to its hardness, regular chip scribers have no effect on such an adamant material and special dicing saws have to be utilized.

In the Scherer Group there is a stock of 4" SOS wafers from previous research projects, which was used in this work. The top silicon layer is 600 nm in thickness with a film resistivity of 8 Ω-cm, while the sapphire substrate is 530 μm. The chip fabrication sequence then follows the steps described in Section 2.1, except that there is no need for the undercut etching by XeF_2 anymore. Compared with bulk silicon chips, however, some caution is needed for etching SOS chips with the pseudo Bosch etch. While sapphire is an excellent etch stop since it barely gets attacked by the pseudo Bosch etch, good control on the etch time is still needed so that excessive etching can be avoided after the silicon layer has been etched through. When the sapphire surface is exposed, positive charge will start to accumulate and expel the incoming plasma ions, giving them additional momentum in the lateral direction. This extra momentum will enable the plasma ions to break the sidewall passivation more easily, resulting in additional etching around the base of the nanostructures, as seen in Fig. 2.15 (A). With excessive etching, such nanostructures may even collapse when the entire base is etched away from the lateral sides. This kind of undercut etching, also known as notching, appears in plasma etching of SOI structures as well [63]. A better option is to leave a certain thickness of the silicon layer instead of etching all the way through; this approach also has the added benefit of better yield for the oxidation step, since now the nanostructures are homogeneously connected to the thin layer below instead of heterogeneously to sapphire. An example of nanopillars not etched through the silicon layer is shown in Fig. 2.15 (B), where the pillar height is ~485 nm. Notching was no longer observed in this case. In Figs. 2.15 (C) and (D), the silicon layer was about to be etched away; due to the thickness variation, some spots were gone faster than others.

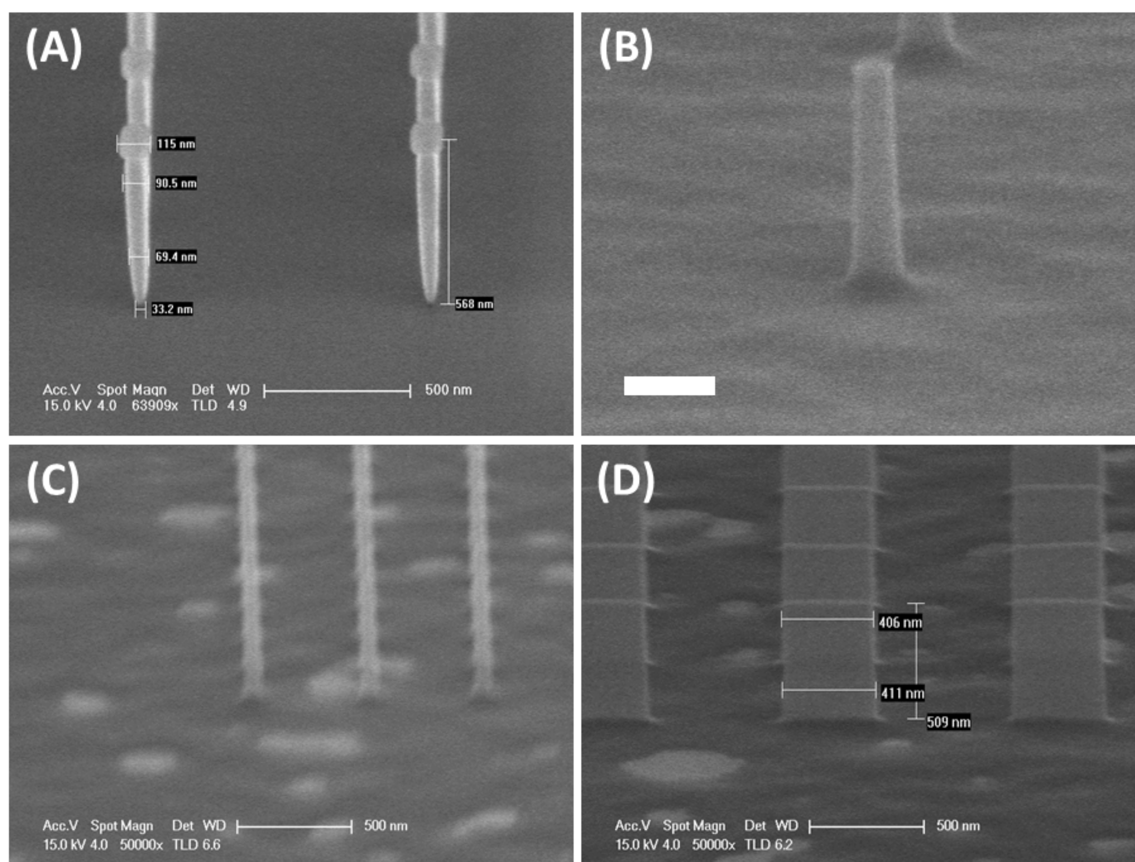

Figure 2.15 (A) Undercut etching, or known as notching, would occur when the SOS chips were etched for too long in the plasma; (B) no undercut etching around the base when the silicon layer was not etched through (scale bar: 200 nm); (C) and (D) show the examples when the silicon layer were about to be etched away.

The nano-patterns on the SOS chips allowed the approach of thermal reflow and mechanical breaking, but the etching method would also work since sapphire is so chemically stable that it does not get affected at all in BHF [55]. Figures 2.16 (A) and (B) show the results of SOS chips after thermal reflow; it can be seen that the Au nano-bulbs had been well separated from the layer below, which is a requirement for good mechanical snapping. Figures 2.16 (C) and (D) are examples of the nano-apertures after the nanostructures had been mechanically broken off.

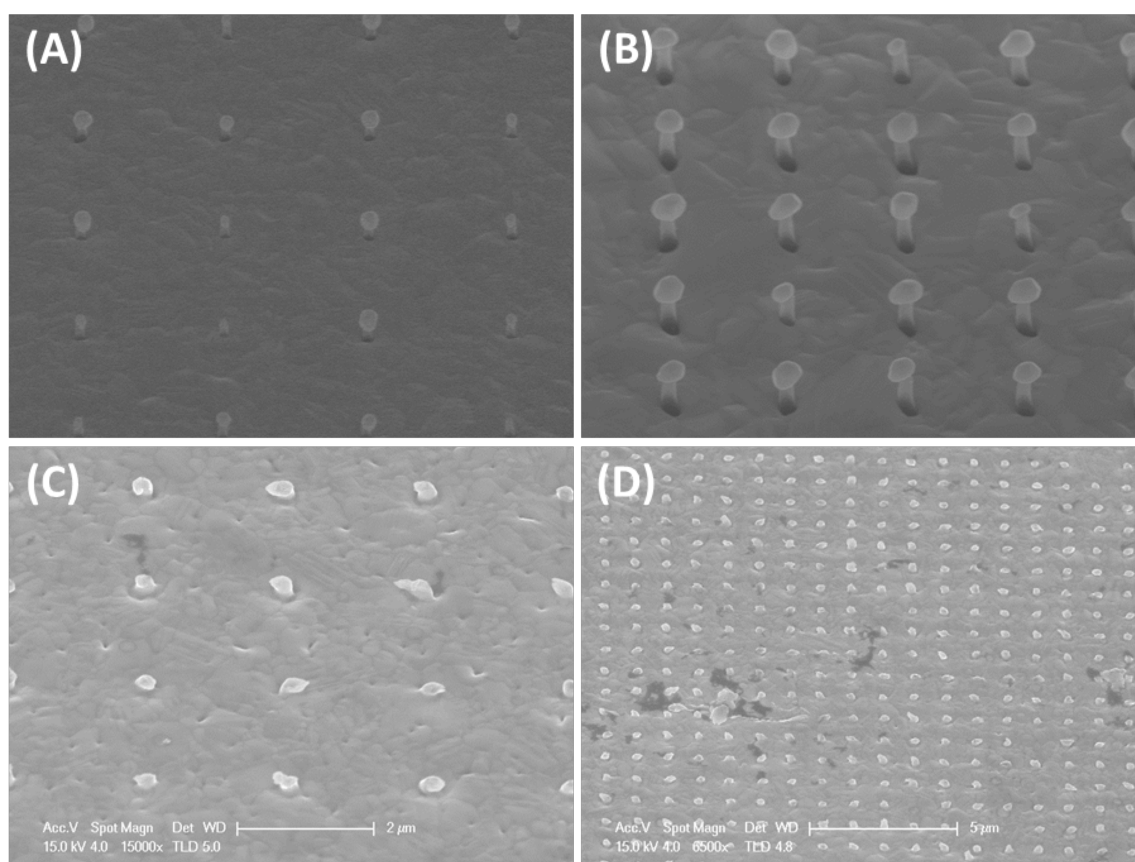

Figure 2.16 (A) and (B) are results of successful thermal reflow from SOS chips; (C) and (D) show the nano-apertures after mechanical snapping.

If the tiny protrusion of silicon dioxide is unwanted, it can be shortened to fine-tune the spectral transmission or to facilitate subsequent bio-molecular functionalization if necessary. In addition to wet chemistry, plasma etching for silicon dioxide is also an option. Chips with Au are not allowed in the ICP etchers at KNI to avoid chamber contamination, so the Plasmatherm Unaxis RIE etcher was used instead. A typical recipe is CF_4 : CHF_3 : Ar = 45 : 15 : 60 sccm at a pressure of 20 mTorr and an RIE power of 80 W (since it is not an ICP-RIE configuration, only one power setting can be adjusted), which has an etch rate of ~20 nm/min. Figures 2.17 (A) and (B) show the results of etching all the way into the nano-apertures, while Figures 2.17 (C) and (D) are examples of when the etching time was controlled for the silicon dioxide "stubs" to be etched flush with the chip surface. This plasma oxide etch can also be used to remove the nanostructures for the metal evaporation approach

as discussed in Section 2.1.6, although if the etching selectivity between silicon dioxide and the resist layer is not high enough, it may cause some problems if Au is not allowed in the RIE machine. Another way is to remove a large portion of nanostructures with wet chemistry first, followed by plasma oxide etch.

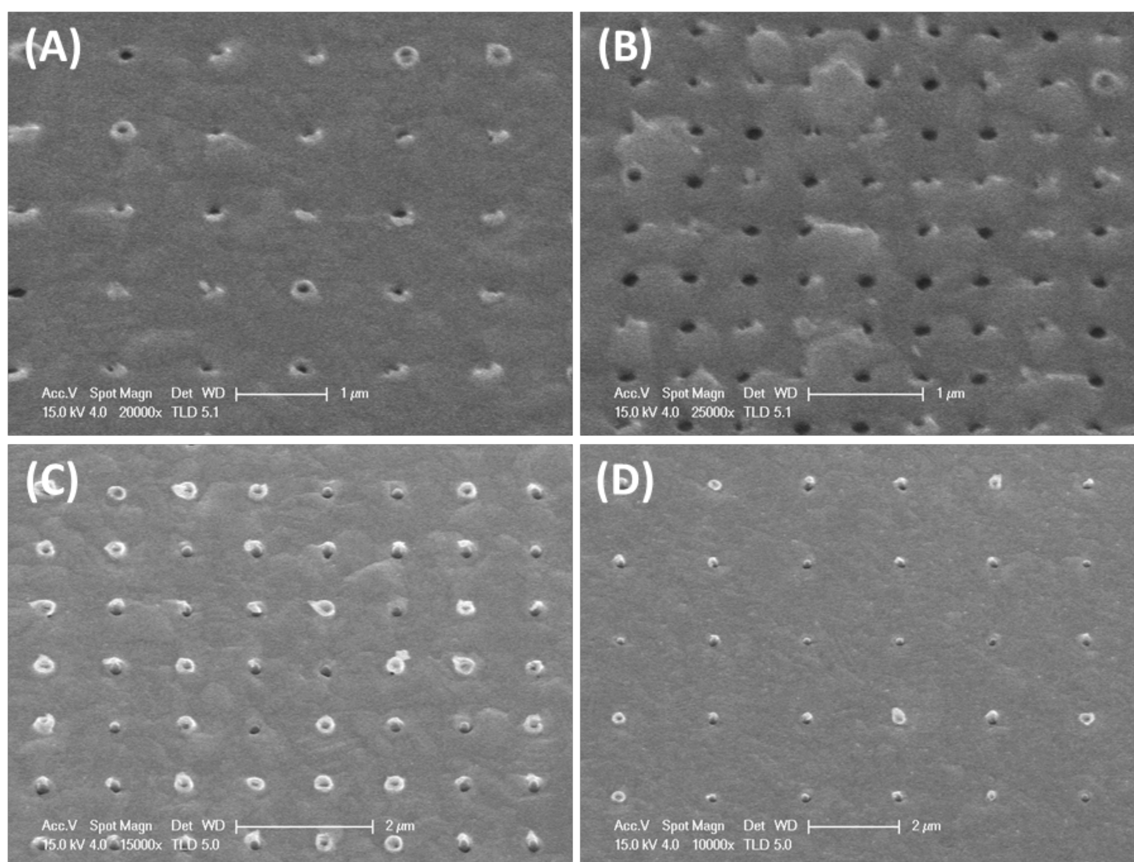

Figure 2.17 (A) and (B) are examples for the RIE oxide etch to remove the silicon dioxide stubs all the way into the nano-apertures; (C) and (D) show that the etch time can be controlled for a flush surface.

One caution of thermal reflow for SOS chips is excessive heating, especially now that the silicon layer is only 600 nm in thickness from the beginning, nanostructures cannot be made taller than this number in order to facilitate Au separation in the reflow process. Figure 2.18 shows some possible defects resulting from a reflow temperature that was elevated too high. In Figs. 2.18 (A) and (B), the cohesive force of Au was starting to overcome the adhesive force

on the silicon dioxide, and the Au layer was beginning to recede from the base of the nanostructures. In Fig. 2.18 (C), even bigger openings resulted due to the same reason, and such a device would be of little use. Even when the thermal treatment temperature is not way too high, there can be undesirable effects as in Fig. 2.18 (D), in which the nanostructures would wick the gold slightly upwards along the sidewall. Careful control and calibration of the reflow temperature is thus required.

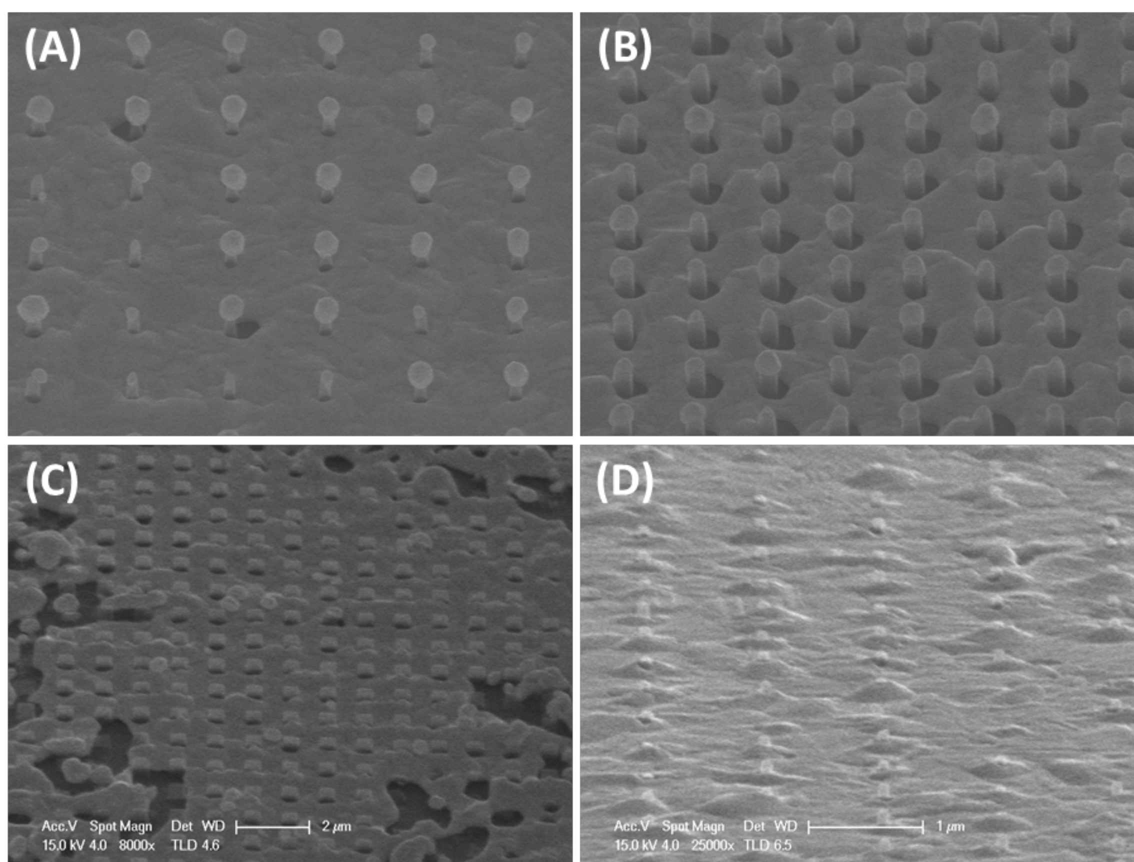

Figure 2.18 In (A) and (B), gold was about to recede from the base of the nanostructures when the temperature was too high; at an even higher temperature, larger openings would result as in (C); (D) shows another sign indicating higher temperature than necessary, when the Au around the nanostructure base region would reflow slightly upwards along the sidewall.

2.2.2 Silicon-on-Glass Substrates

Although silicon-on-sapphire chips provide a strong and transparent substrate, the available wafers still place some restrictions on the applications. The thickness of the silicon layer at 600 nm is the biggest issue, which is especially serious if the nanostructures are to be 3D sculpted for spectral tuning. The sapphire layer at a thickness of 530 μm also limits the use of high-magnification objectives in microscope-based applications, since objectives with a long working distance are either unavailable or extremely expensive to be highly magnifying. Other commercially available SOS wafers also have similar silicon and sapphire thickness. As mentioned earlier, SOS wafers were designed for the electronics industry, so the backside is typically unpolished, which can be disastrous for optics. The mechanical hardness and chemical inertness of sapphire now becomes an obstacle – it would be extremely difficult to polish or etch the backside to be optically flat. The high pricing of SOS wafers is also a concern, since sapphire is actually overkill if the only goal is to have a substrate that is transparent and does not break. Even in the electronics industry, the main stream of the SOI substrates is buried silicon dioxide in silicon wafers, even though the SOS technology has been invented for more than half a century [64].

Silicon-on-glass (SOG) chips would be a good choice to address all these issues. They are less expensive in price, and they are available for a thicker device layer of silicon and a thinner handle layer of glass. Glass is also much softer than sapphire, and does not call for special dicing saws. In this work, SOG wafers purchased from Plan Optik AG were used. The silicon layer is 20 ± 5 μm in thickness, <100> orientation, and boron-doped to be 1-50 Ω-cm; the glass layer is 300 ± 10 μm thick and double-side polished for optical qualities. Unlike sapphire, glass can be readily etched in BHF and can be efficiently thinned down if necessary.

Although the thickness of the silicon layer is now more than enough, it has to be brought down to a moderate level first so that the entire Si region can be fully oxidized in the thermal furnace within reasonable time. At this moment the thickness variation of ± 5 μm excludes the possibility of thinning down the entire wafer at once, and hopefully in the future when there is a greater demand of SOG wafers with a more uniform silicon layer (preferably within ± 0.5 μm), a single etch can bring the top layer to the desired thickness. For now, the thinning

process has to be done individually for each chip, or otherwise the yield will be sacrificed; while the thicker region attains the desired thickness, the thinner part will be gone already, or while the thinner region is at the correct thickness, the other areas will be too thick for thorough oxidation.

First, the thickness of the silicon layer has to be measured for each chip. At KNI a handy tool for such a purpose is Filmetrtics F40, a device integrated into the microscope Olympus BX51M for measuring thin film thickness using spectral reflectance. Even though silicon is not an excellent light-absorbing material due to its indirect bandgap, at a thickness greater than 10 μm it would still absorb a significant amount of light. Referring to Fig. 2.19 (A), the absorption depth of silicon is already 11.76 μm at an optical wavelength of 800 nm, and

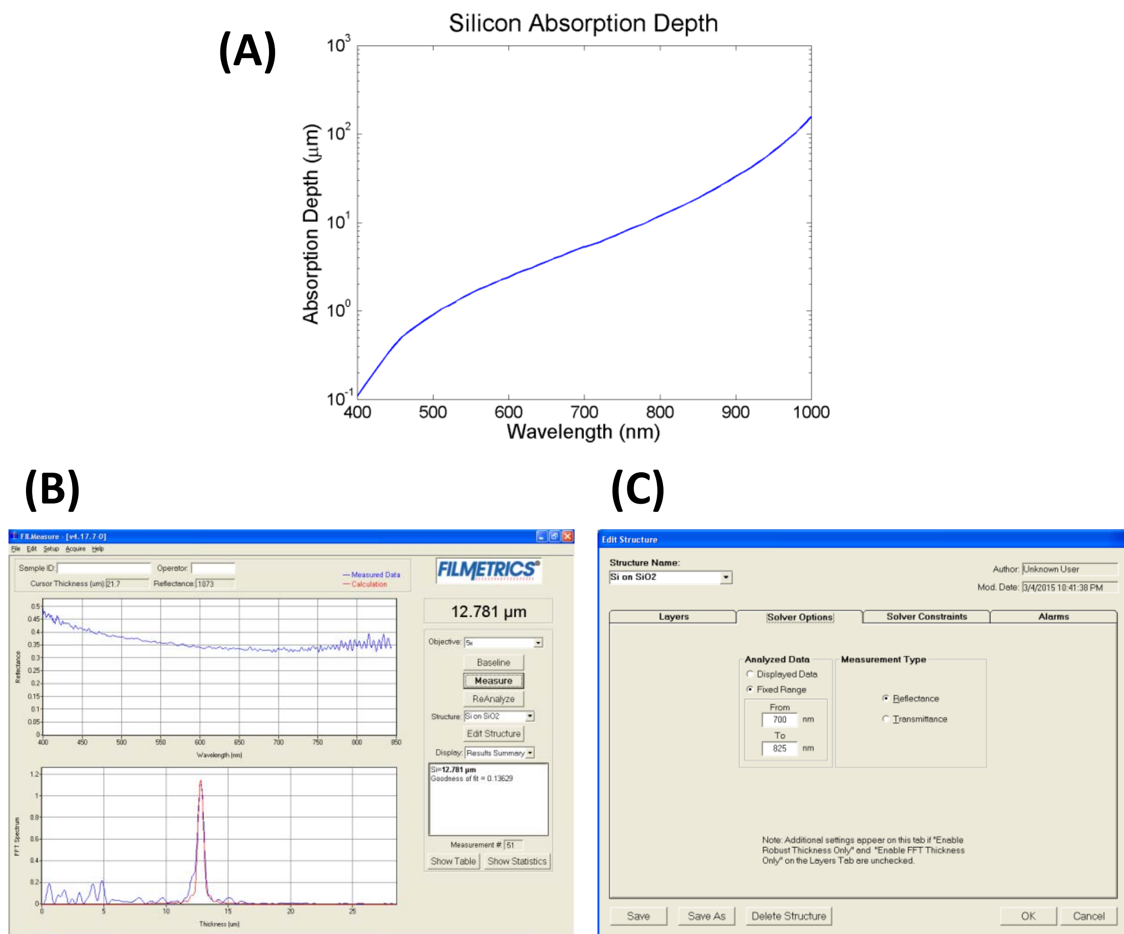

Figure 2.19 (A) Absorption depth of silicon at different optical wavelengths. (B) FFT mode of Filmetrics F40 for measuring thick silicon; (C) the wavelength range can be further specified to improve fitting results.

further drops to 5.29 μm at 700 nm (raw data from [65]). Curve fitting turned out to be tricky in the regular operation of Filmetrics. This issue can be circumvented by running Filmetrics in the fast Fourier transform (FFT) mode; in Fig. 2.19 (B), it can be seen that the oscillation of wavelength-dependent reflection is quite subdued for a large spectral range, but in the lower FFT panel the thickness can be well fitted. If peak fitting becomes difficult even in the FFT mode, the fitting range can be further specified as in Fig. 2.19 (C), where only the range of 700 – 825 nm would be considered.

The top silicon layer can now be thinned down. There are various options for this purpose, such as the potassium hydroxide (KOH) solution, XeF_2 etching, etc. Plasma etching was chosen in this work because of its controllability and repeatability; moreover, it is readily applicable to whole-wafer processing. Although a regular RIE-type machine can also be used for this purpose if the chamber is kept clean for silicon-only operations, the DRIE etcher, an ICP-RIE machine at KNI, was selected for the thinning process because it allows a higher plasma power and a larger gas flow permitted by the mass flow controller (MFC). The etch was carried out at an SF_6 gas flow of 100 sccm, a chamber pressure of 20 mTorr, an ICP power of 2000 W, and a CCP power of 30 W. Figure 2.20 (A) shows the calibrated etch rate for such a recipe; the etch rate was approximately 2.14 μm/min, or about 36 nm/s. Since the control precision of the etch time is 1 second, such a resolution is more than enough for the thinning purpose. The parameters can be further optimized if an even faster etch is desired, especially the ICP power, the gas flow, and the chamber pressure. Increasing the CCP power would not help much since there is no passivation layer to mill through here, and the etching mechanism is mostly chemical in nature. Figure 2.20 (B) shows the photo of thinned-down SOG chips (chip size: 10 by 10 mm); although it may not be conspicuous enough in the photo, wavy patterns from interference could be seen when the chips were tilted at some specific angles to the indoor lighting due to the inhomogeneous thickness of silicon on the glass substrate. The chip on the right was diced from the edge of an SOG wafer, where the thickness of the silicon layer would be decreasing towards the wafer edge. Initially the silicon region would extend all the way to ~1 mm away from the edge, but after the plasma etching the thinner regions were totally gone already.

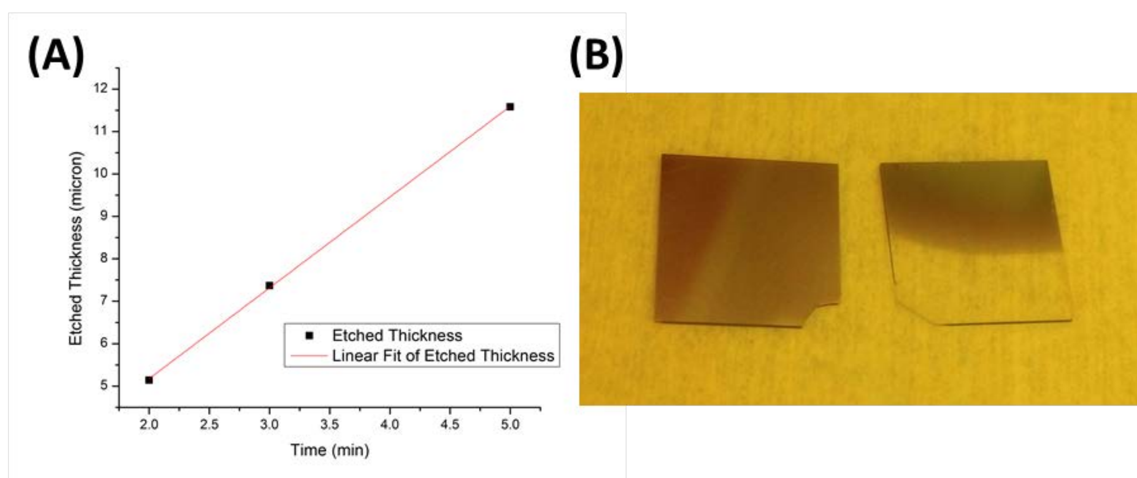

Figure 2.20 (A) Calibrated etch rate for thinning down the top silicon layer on SOG chips. (B) Photo of thinned SOG chips; the right one came from the edge of an SOG wafer. Chip size: 10 by 10 mm.

The rest of the fabrication steps are similar to those described in the section of SOS chips. The doping level of the silicon layer was sufficient to prevent charge buildup from happening during the e-beam lithography, and special techniques such as coating a conducting layer [23, 66], using conducting e-beam resist [67], or even adjusting the electron beam acceleration voltage [68] were not necessary. Figure 2.21 (A) shows the nanostructures on an SOG chip after pseudo Bosch etching; patterns of the original design were indeed preserved without distortion from surface charge buildup during the e-beam lithography. Figure 2.21 (B) shows

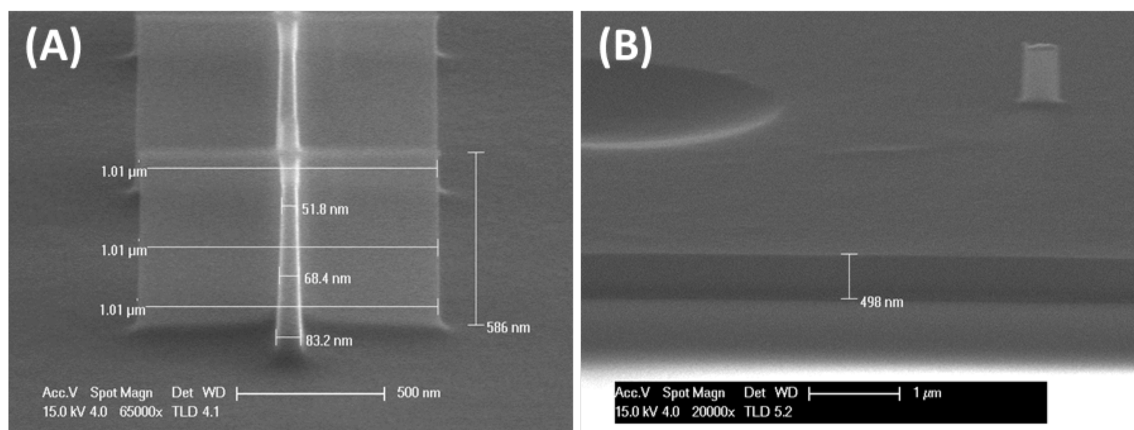

Figure 2.21 (A) Nanostructures on an SOG chip after pseudo Bosch etching. (B) Remaining thickness of the silicon layer after plasma thinning and pseudo Bosch etching.

the remaining thickness of the silicon layer after the pseudo Bosch etching; by controlling the initial thickness of the silicon layer after plasma thinning and the height of the nanostructures to be etched, this final thickness of Si can also be tailored to any desirable value.

2.2.3 Options for the Metal Layer

In addition to gold, aluminum is also demonstrated in this work for EOT nano-apertures. The fabrication procedures are similar to those described in Section 2.1.6, except that thermal reflow is not an option for aluminum since it would either evaporate away or react with the gas present in the annealing chamber. For the sputtering approach, again a resist layer can be spin-coated on the chip first, followed by oxygen plasma ashing to reveal the top of the nanostructures, similar to the procedures depicted in Figs. 2.14 (A) and (B). Examples of these results are shown in Figure 2.22.

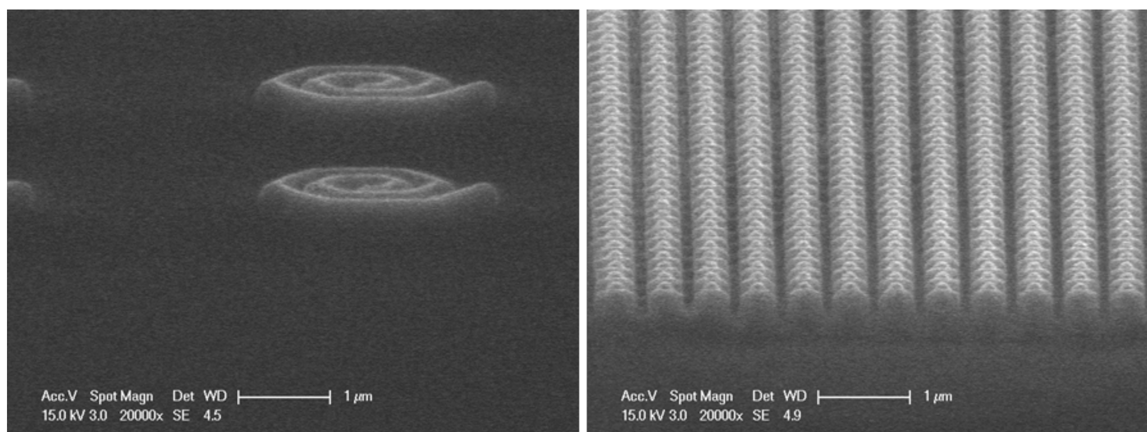

Figure 2.22 After a resist layer was spin-coated on the chip, oxygen plasma ashing could remove the right amount of resist to reveal the top of the nanostructures.

An etchant can now be useful in this scenario if it attacks aluminum but leaves alone silicon dioxide and the masking resist layer. The scenario is similar to Fig. 2.14 (C), except in this case the sidewall of nanostructures would be covered with Al as well. Tetramethylammonium hydroxide (TMAH) meets this requirement and happens to be commonly available in the cleanroom; it is the active ingredient in many types of photoresist developer. Since TMAH is diluted when used in photoresist developers (typically at a concentration of ~2.4%), it also

makes the etching time easier to control. In this work the Microposit MF CD-26 Developer from Dow was used, although other options such as Microposit MF-319 from the same company should also work. Figures 2.23 (A) and (B) show some examples of coated nanostructures with the aluminum sidewalls etched away already; the SiO_2 core and the resist layer were indeed still intact. The etching time has to be well calibrated, though, since there is no natural etch stop in this case. Figures 2.23 (C) and (D) are examples of when the etch time was not long enough, and Figs. 2.23 (E) and (F) illustrate the isotropic nature of wet etching when it was overdone. There are also Al etchants available at KNI that do not etch silicon dioxide, but their compatibility with e-beam or photoresist was not tested for this work. For readers' information, they typically consist of nitric acid (HNO_3), phosphoric acid (H_3PO_4), and acetic acid (CH_3COOH).

After pinpointing the correct time of etching, the nanostructures could then be mechanically snapped in the same way as described in Section 2.1.6. Since hydrofluoric acid etches away aluminum at a high rate [55], unfortunately there is no wet chemistry that removes the silicon dioxide core while keeping the aluminum part intact. Plasma oxide etch, such as the recipe described in Section 2.2.1, can be an option since chlorine-based chemistry is required to plasma-etch aluminum [16]. Figure 2.24 shows some examples of fabricated nano-apertures on a 200 nm thick Al film.

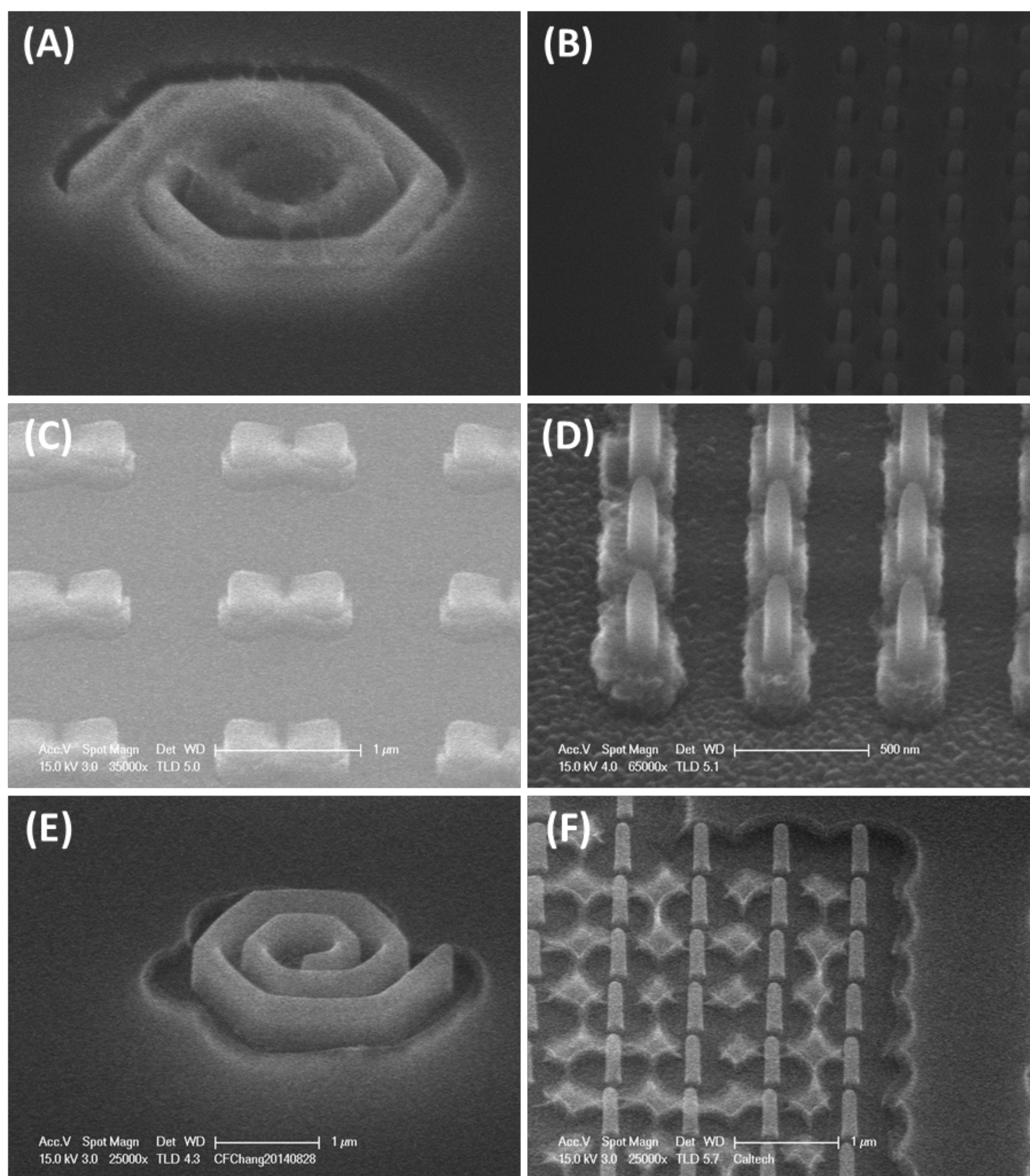

Figure 2.23 CD-26 developer would etch away aluminum without affecting silicon dioxide or the resist layer, as shown in (A) and (B). Without an etch stop, if the etch time was too short the results would look like (C) and (D), while over-etching would be like (E) and (F).

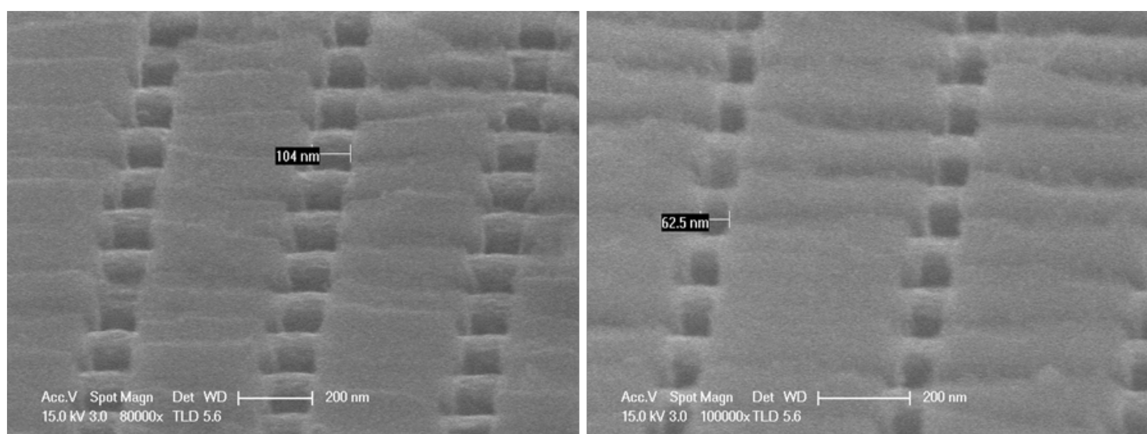

Figure 2.24 Examples of nano-apertures on an aluminum film.

Evaporation is also an alternative for aluminum deposition. Figures 2.25 (A) and (B) are examples of evaporated aluminum on SOS chips with nanostructures; again the nanostructure

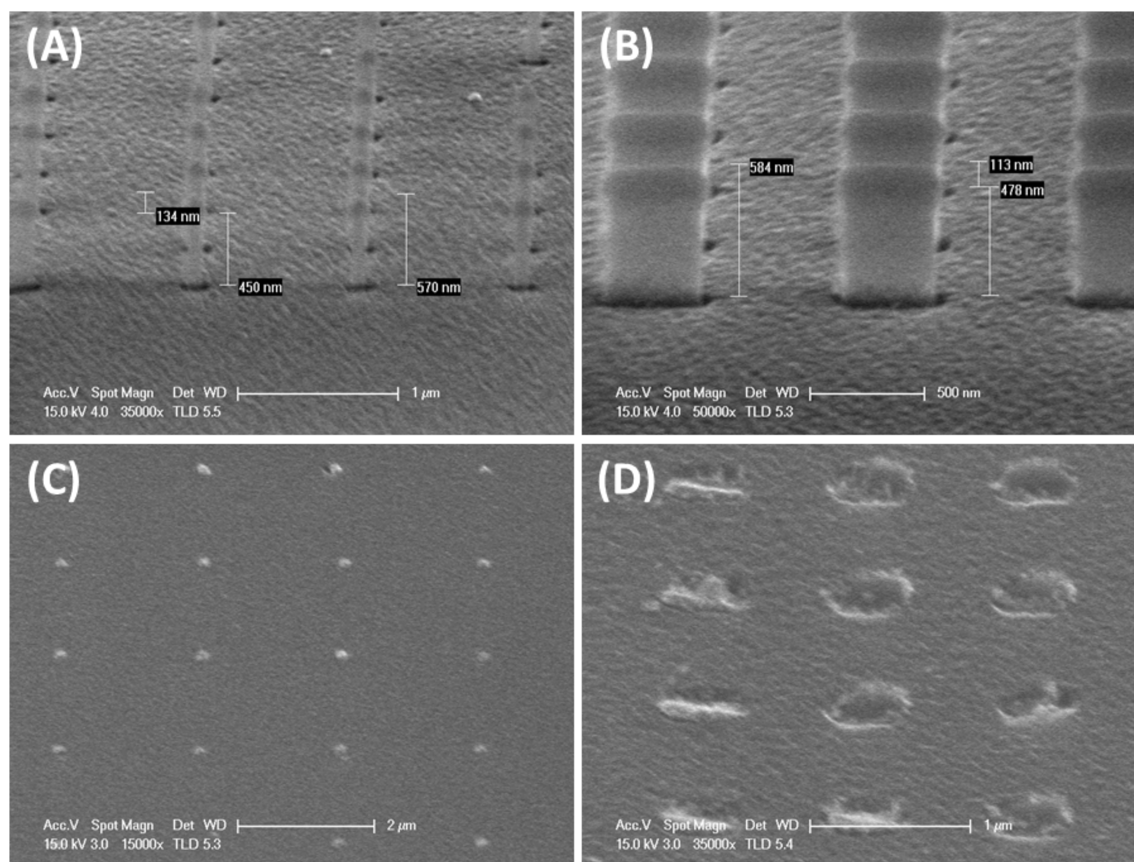

Figure 2.25 (A) and (B) show the feasibility of evaporating aluminum on SOS chips with nanostructures; (C) and (D) are results after the nanostructures are mechanically snapped.

height should be appropriate in order to avoid excessive shadowing effects around the base of nanostructures, since thermal reflow is no longer a remedy to seal up those tiny gaps. Compared with gold, aluminum does not provide so much tenacious connection on the nanoscale against mechanical snapping, and the nanostructures could be broken off with good results as shown in Figs. 2.25 (C) and (D).

2.3 EOT Characterization

The EOT characterization was done on a microscope with additionally attached optics and a fiber-based, liquid-nitrogen-cooled spectrometer. The use of spectrometer allows the illumination source to be regular broadband white light, and eliminates the necessity of expensive options such as tunable lasers or supercontinuum light sources. The effect of the incident polarization was investigated, and Au nano-apertures were compared with their Al counterpart for the transmission characteristics.

2.3.1 Experimental Setup

The schematic of the experimental setup is shown in Fig. 2.26. An Olympus BX 60 microscope was used as the main platform of measurement, which comes with a broadband white light source (roughly 400 – 1000 nm) that can illuminate the sample from below. A linear polarizer was inserted between the light source and the sample, so that the polarization direction can be rotated when necessary. In this work, the 0° polarization is defined when its direction is parallel with the long side of nanostructures that are rectangular in shape, as depicted in the figure. A 100X objective then collected the transmitted light, which was fed into an optical fiber attached to the top port of the microscope. A lower-magnification objective may also be used, as long as the fiber field of view does not include other groups of nano-apertures in addition to the one being measured. The optical fiber goes into an Acton SpectraPro 2300i spectrometer by Princeton Instruments, which can be cooled by liquid nitrogen to improve the sensitivity. The background spectra were taken at different spots on the metal film without nano-apertures, and then averaged. The chip was then removed for the measurement of the reference spectrum from the light source. If the detector saturates, one trick is to reduce the shutter time while increasing the total number of integration accordingly, so that the total exposure time remains the same as for the nano-aperture measurement. After

subtracting the averaged background spectrum from the transmitted spectrum, division by the reference spectrum will produce the transmission ratio through the nano-apertures.

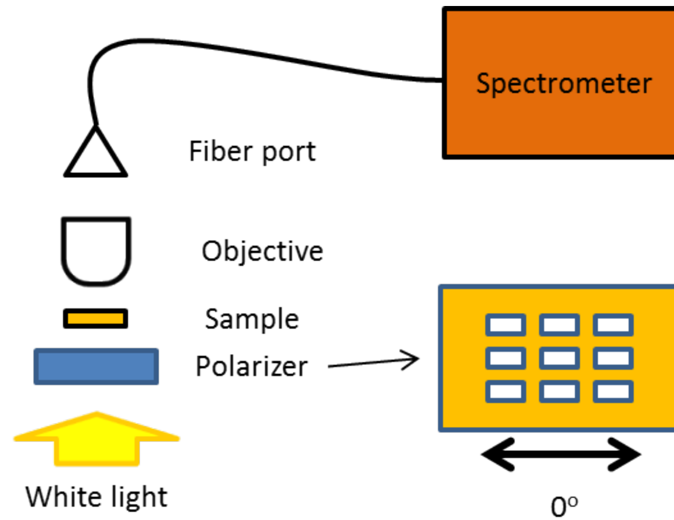

Figure 2.26 Schematics of the experimental setup for EOT measurement.

2.3.2 Polarization Measurement

For the first group of patterns to be investigated, the CAD file dimensions were: width = 50 nm (along the *y* direction), varied length (along the *x* direction) from 200 to 350 nm, and periodicity = 500 nm (for both the *x* and *y* directions). The polarizer was rotated to 0, 45, and 90 degrees for the measurement of transmitted spectra. Figure 2.27 shows the transmission ratios from these nano-apertures with various lengths; the Au thickness was 200 nm. One trend in the transmission spectra is that more light propagated through the nano-apertures when the polarization was perpendicular to the long side of the rectangles, i.e., when the polarization was at 90°. This is because plasmonic modes are more efficiently induced when the electric field of the light wave is perpendicular to the metal surface [69], so when it is at a right angle to the long side, more modes can be excited to propagate through the nano-apertures. As an analogy in the asymptotic limit, the wire grid polarizer would allow the polarization perpendicular to wire direction to pass through while rejecting the electric fields parallel with the wires [70]. It can also be observed that the transmission at 45° polarization is

roughly the superposition of those at 0° and at 90°, which is physically intuitive. As the nano-aperture became longer, the transmission peak at 90° polarization also shifted to a longer wavelength, while the peak associated with 0° remained roughly at the same wavelength. This observation supports the view that the plasmonic modes were better excited when the optical field is perpendicular to the metal surface, and hence there was more spectral shift when the polarization was at 90°. When the nano-aperture length became even longer, two local resonance maxima could be seen as in Figs. 2.27 (C) and (D). The wavelengths of transmission maxima for the 90° polarization were approximately 3 : 4 in ratio, while those for the 0° polarization were roughly 2 : 3. This probably indicates some relationship of harmonic resonance, although while closed-form solutions are available for EOT through elliptical nano-

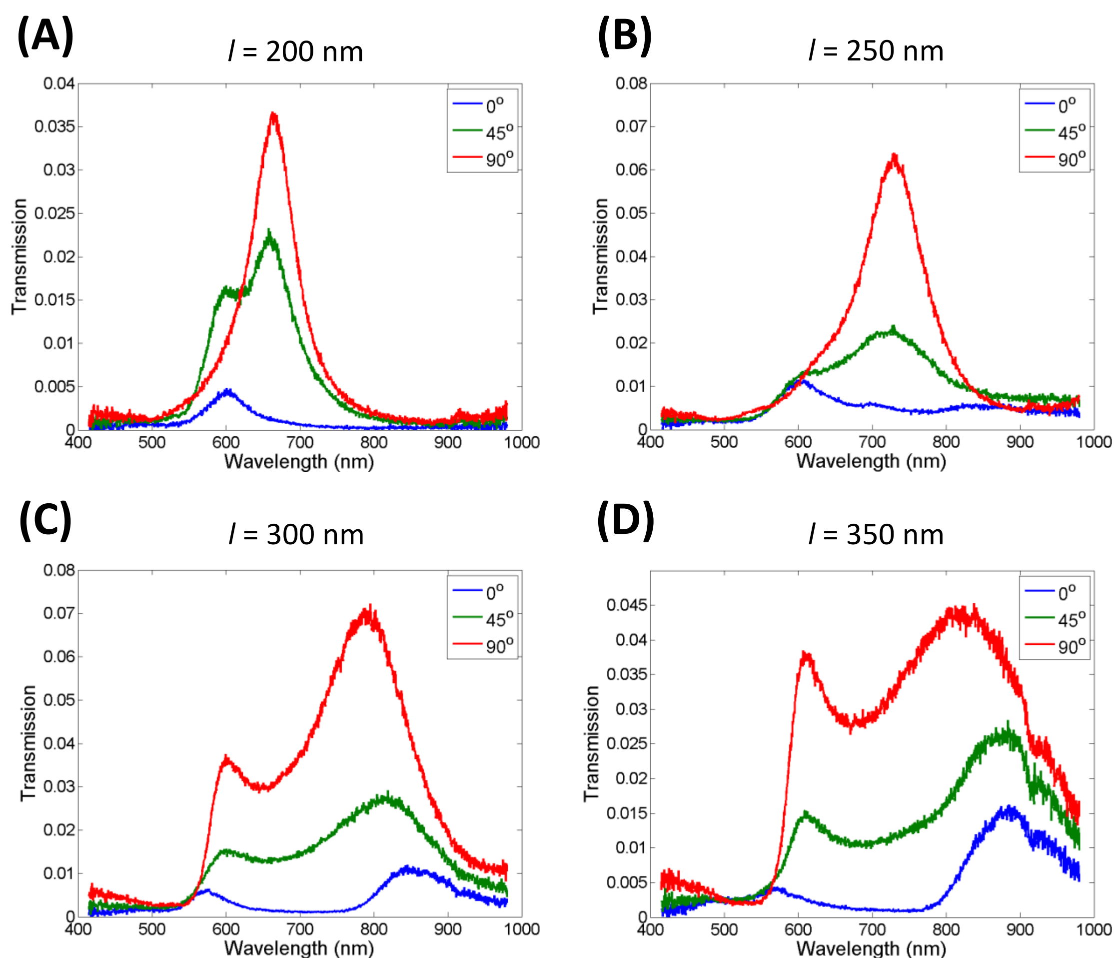

Figure 2.27 Transmission spectra of various nano-apertures on a 200 nm Au layer.

apertures, numerical simulation has to be utilized for rectangular apertures [71].

For the second group of patterns, each cell unit contains two components: one 250 by 50 nm, and the other 50 by 100 nm with a center-to-center offset with respect to the first one, as shown in Fig. 2.28 (A). The periodicity is still 500 nm for both directions. The spectral characteristics are more interesting with this kind of binary configuration: the transmission band at one polarization can be the forbidden range of the other, and vice versa. Figure 2.28 (E) is a particularly good example of this, which can potentially lead to super-resolution on-chip imaging that doubles the pixel number of the imaging sensor. The results here also illustrate the array effect of the nano-patterns; even though individual components have the same dimensions, by varying their relative positions the transmission spectra would change already. The EOT array can be considered as a kind of nano-grating that re-scatters the incident photons, and therefore it is physically intuitive that the change of the internal arrangements within the unit cell would alter the spectral characteristics of transmission. When the smaller component shifted upwards within the cell from (0, 150) to (0, 250) nm, the transmission peak at 0° polarization would shift to shorter wavelengths, and the peak strength would increase for both 0° and 90° polarizations. When the smaller component further shifted to the left from (0, 250) to (-100, 250) nm, the peak intensity for 0° polarization gradually decreased, thus moving farther and farther away from the sweet spot of orthogonal transmission bands at 0° and 90° polarizations. In the measurement it was also observed if the pattern was only halfway in the field of view for the signal collection, the transmission spectrum would also be different. The nano-apertures can therefore be regarded as an array of optical antennae, and collectively they have an antenna array pattern that may exhibit sharp angular variations around the edges.

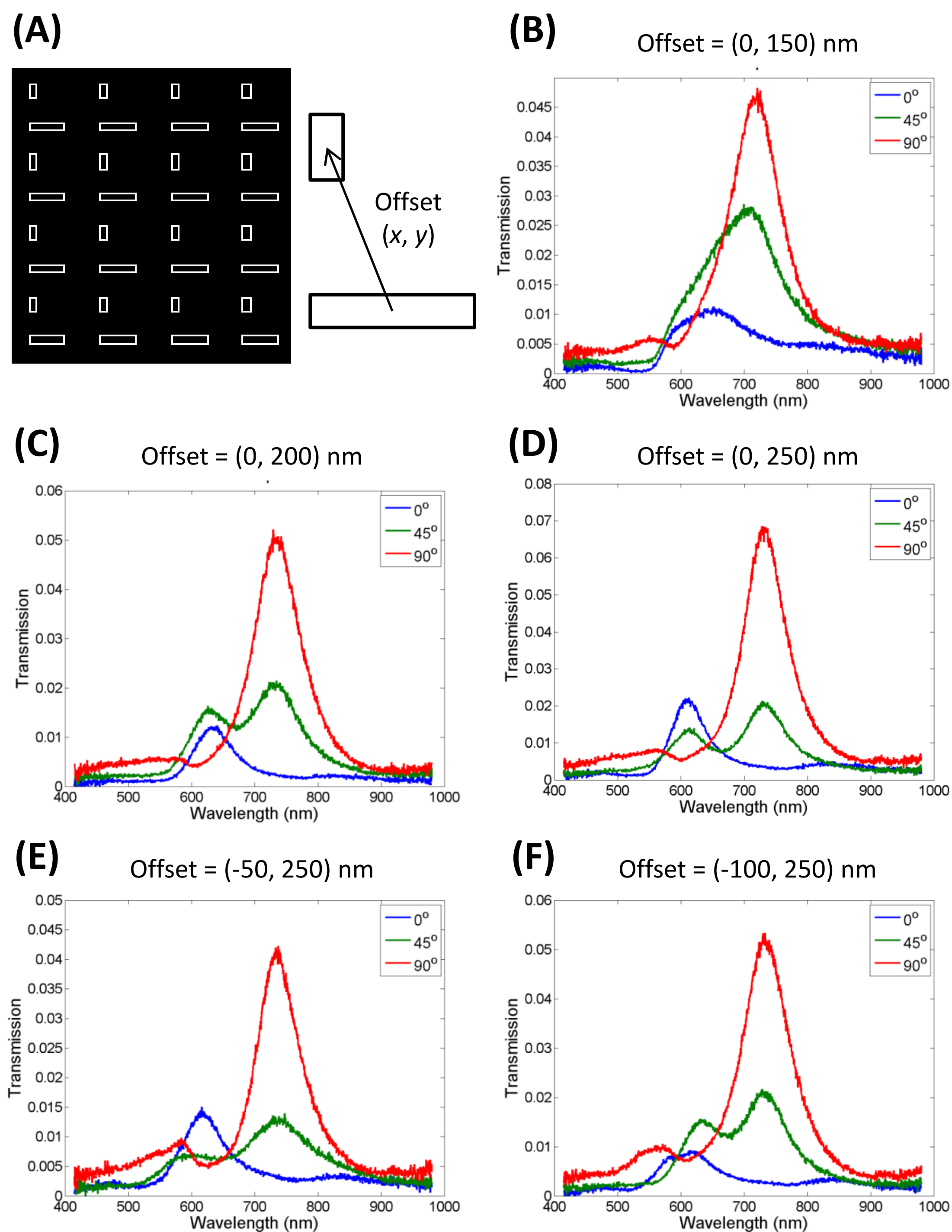

Figure 2.28 (A) One example of the CAD design for two-component nano-apertures; (B) – (F) are transmitted spectra for the patterns with different offsets between the components.

2.3.3 Comparison between Au and Al

Since plasmonics is also highly-dependent on the metal characteristics, a direct comparison of the EOT transmission spectra is illustrated here for the same pattern of nano-apertures and the same metal thickness. The patterns are those described for Fig. 2.27 (D), and the spectrum is re-plotted here as Fig. 2.29 (A) for the convenience of comparison. The metal thickness was 200 nm for both Au and Al. From Fig. 2.29 (B) it is clearly seen that the spectral shape is quite different from that in Fig. 2.29 (A), and more importantly, the transmission intensity is greatly reduced. This is because in plasmonics the attenuation coefficient is in the form of [72]

$$\alpha = 2k_0\sqrt{\omega_p^2/\omega^2 - 1}\,,$$

and therefore at the same wavelength the attenuation will be greater for materials with a higher plasma frequency. As previously mentioned in Chapter 1, the plasma wavelength of Au is 139 nm and that of Al is 98 nm, which correspond to the plasma frequency of 216 and 306 THz, respectively. Furthermore, aluminum has an interband transition around 800 nm, which results in a large imaginary part (i.e., loss) of its refractive index [11]. Since the attenuation coefficient decreases when the wavelength becomes shorter, aluminum is anticipated to fare better for plasmonic applications in the UV regime [11, 50]. Aluminum-based plasmonics in the UV regime, such as surface-enhanced fluorescence [73], has been demonstrated in the past.

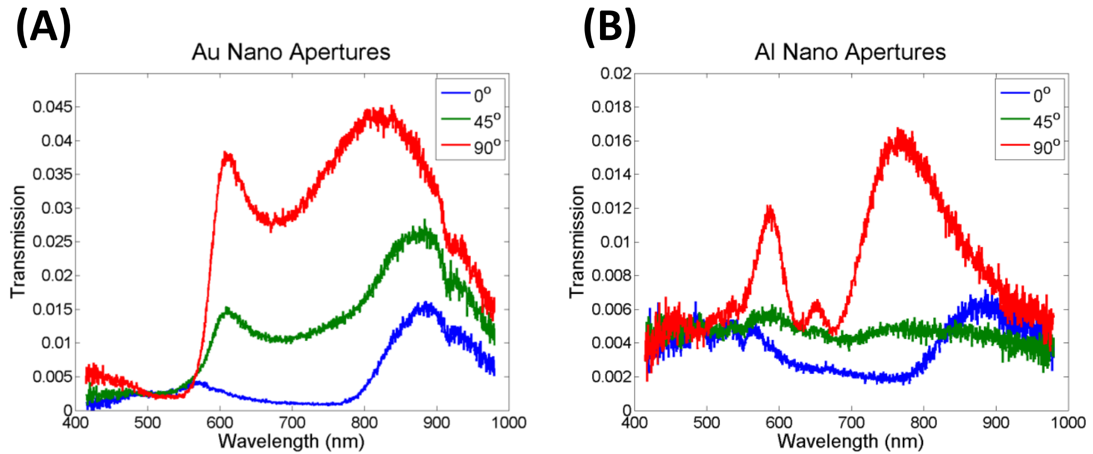

Figure 2.29 (A) Au and (B) Al EOT transmission spectra from the same pattern of nano-apertures and at the same metal thickness.

2.4 EOT Fluorescence Measurement

Tuning of spectral transmission is only one application of nano-apertures. Since light is forced to propagate through these tiny passages, if materials of interest are attached to the opening of the nano-apertures but not elsewhere, the signal-to-noise ratio will be greatly enhanced compared with other optical sensing methods. Such a device can be a sensor or bio-molecular assay with a high efficiency.

Fluorescence was chosen to prove the concept for its ease of optical readout, and the experiments were performed on SOS chips since they were robust enough to withstand the bio-molecular treatment. Glutamic acid caged in a variant of coumarin, 7-(N,N-diethylamino)-4-(hydroxymethyl) coumarin, was first coated on SOS chips, as shown in Fig. 2.30 (A). This compound, abbreviated as DECM-CG here, undergoes photolysis when exposed to wavelengths from ~350 to 410 nm [74]. This range happens to include the i-line wavelength (365 nm) and the h-line (405 nm) of typical photolithography machines, and therefore a photomask aligner can conveniently serve as an exposure source with very precise time control (down to 0.1 s for the MA/BA6 machines at KNI). The 365 nm wavelength was chosen to exposure the chips facing down on the holder; namely, the UV light was incident on the backside of the chips, as illustrated in Fig. 2.30 (B). Fluorescein isothiocyanate (FITC) was then applied onto the chip as in Fig. 2.30 (C). For the area that was "photo-uncaged" with the UV exposure, FITC would adhere onto the region and respond with fluorescence when excited, while the other areas should be FITC-free; the schematic is shown in Fig. 2.30 (D).

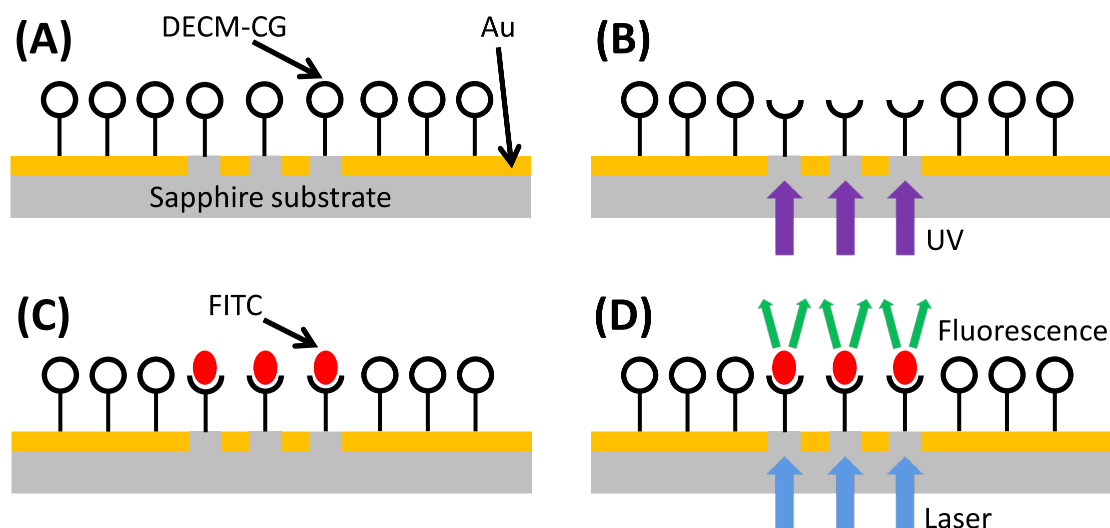

Figure 2.30 Procedures of photo-uncaging. (A) DECM-CG is first coated on the chip; (B) UV exposure from the backside photo-uncages the molecules at the nano-apertures; (C) FITC fluorophores are then attached to the photo-uncaged areas; (D) FITC fluorescence can now be excited from the backside.

The measurement was done with a Zeiss LSM 710 confocal microscope in the Beckman Institute at Caltech. For safety concerns, Zeiss only allows the laser illumination to be available from the bottom of the stage, and therefore the chip was placed facing upwards on the holder. Although the LSM 710 microscope has a sophisticated spectrometer system that allows the user to specify which range of wavelengths should be integrated, this feature is only available on the side where the laser comes from (here referred to as the reflection port for convenience). As a result, a 515 nm longpass filter (FGL515M from Thorlabs) was placed between the sample and the condenser on the detection side, i.e., the transmission port, in order to block the 488 nm laser source that was used to excite the FITC molecules. For comparison and for locating the nanostructures on the chips more easily, images were also taken at excitation wavelengths of 561 and 633 nm. The photonic signals were then collected by the photomultiplier tube (PMT) in the system and recorded by the control interface.

Previously it was mentioned that the backside of SOS wafers is typically unpolished since they were not designed for optical applications in the first place, and here it became a

prominent issue in the measurement. Figure 2.31 (A) shows the scanned image in the reflection port when the laser beam was focused at the sapphire surface on the backside; the roughness was faithfully recorded by the back reflection. In the transmission port, as shown in Fig. 2.31 (B) with the light source still being 633 nm, the surface roughness still degraded the image quality significantly even though the laser spot was focused to the sub-μm level already. When the focus was brought to the approximate level of the nano-apertures, as shown in Fig. 2.31 (C) when excited by 488 nm, the image quality was still undesirable.

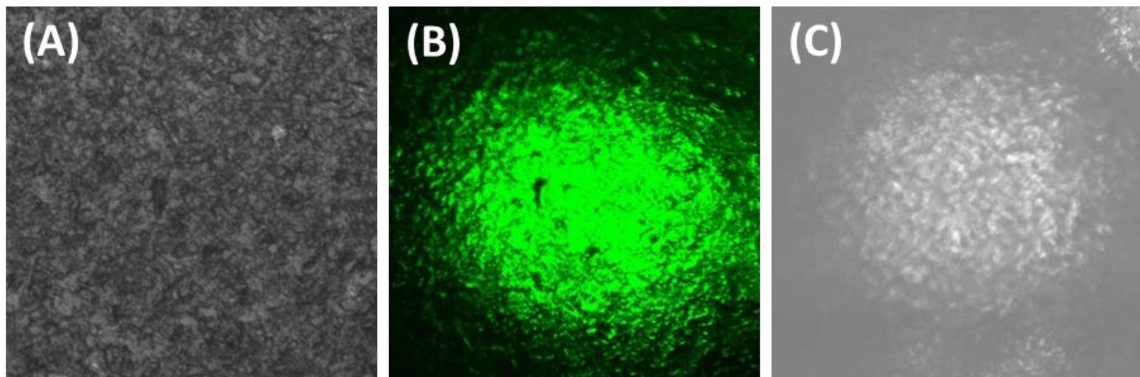

Figure 2.31 Scanned images of (A) reflection and (B) transmission from the backside sapphire surface at focus; laser: 633 nm. (C) Transmission image illuminated by the 488 nm source when the nano-apertures were roughly at focus.

The issue can be addressed by filling up the gap between the chip backside and the glass slide on the sample holder with some fluid that mitigates the dramatic contrast in refractive index between air and sapphire. Since sapphire has not been used widely enough in optics, there does not seem to be index-matching liquids commercially available that have the identical refractive index in the entire range of optical wavelengths. However, it was found out if a liquid was used with a refractive index close enough to sapphire, the image quality could be greatly improved already. Since the silicon layer was grown on the [0001] sapphire substrate, the polarization of the incident light would be perpendicular to this *c* axis and hence sees the refractive index in the extraordinary direction, following the Sellmeier equation as [75]

$$n_e{}^2 = 1 + \frac{1.5039759\lambda^2}{\lambda^2 - 0.0740288^2} + \frac{0.55069141\lambda^2}{\lambda^2 - 0.1216529^2} + \frac{6.59273791\lambda^2}{\lambda^2 - 20.072248^2},$$

where the wavelength is in μm. This refractive index is plotted in Fig. 2.32 (A) for the range of

400 – 1000 nm. In the lab there was a bottle of refractive index liquid with a nominal *n* = 1.70000, from the Series B liquid products manufactured by Cargille. Although this refractive index is still somewhat smaller than that of sapphire, the microscopy images already got much sharper when the liquid was added between the chip and the glass slide. Figure 2.32 (B) shows an example of when a group of nano-apertures were illuminated by the 561 nm wavelength with such a refractive index liquid below the backside of the chip; individual nano-apertures, 2 μm apart in this case, were able to be resolved.

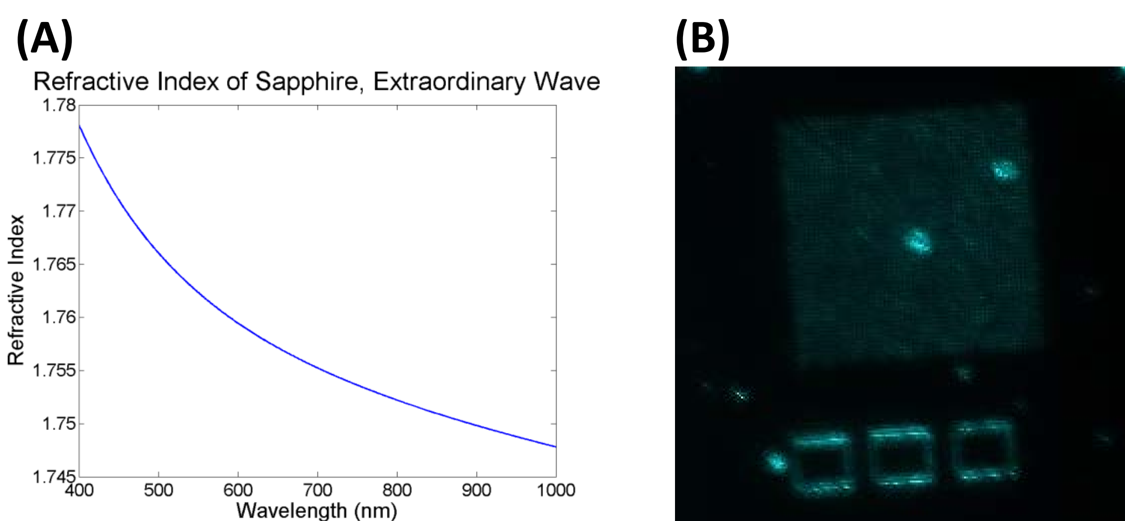

Figure 2.32 (A) Extraordinary refractive index n_e of sapphire as a function of wavelength. (B) Much sharper microscopy image when the refractive index liquid was used.

Further measurement results confirmed the fluorescence from FITC, and thus the concept of photo-uncaging for EOT sensors. Figures 2.33 (A), (B), and (C) show the microscopy images of nano-apertures from a laser wavelength at 488, 561, and 633 nm, respectively; the associated parameters of measurement are listed in Table 2.2. The nano-apertures were 400 by 80 nm in size, and the period was 1 μm in both directions. It should be noted that the actual PMT gain (i.e., the PMT current amplification) increases exponentially with the detector gain in the control interface, which adjusts the PMT voltage; when the voltage doubles, the actual gain is almost 300 times larger. Despite a lower laser power, a smaller PMT gain, and worse PMT quantum efficiency at longer wavelengths, Figs. 2.33 (B) and (C) are still of

approximately the same brightness as in Fig. 2.33 (A). As a result, the longpass filter indeed sufficiently blocked the laser light at 488 nm, and FITC fluorescence was observed. When the FITC molecules are replaced by other fluorophores that can respond to the environment, such as fluorescent antibodies, the chip can function as a sensitive and label-free bio-molecular assay.

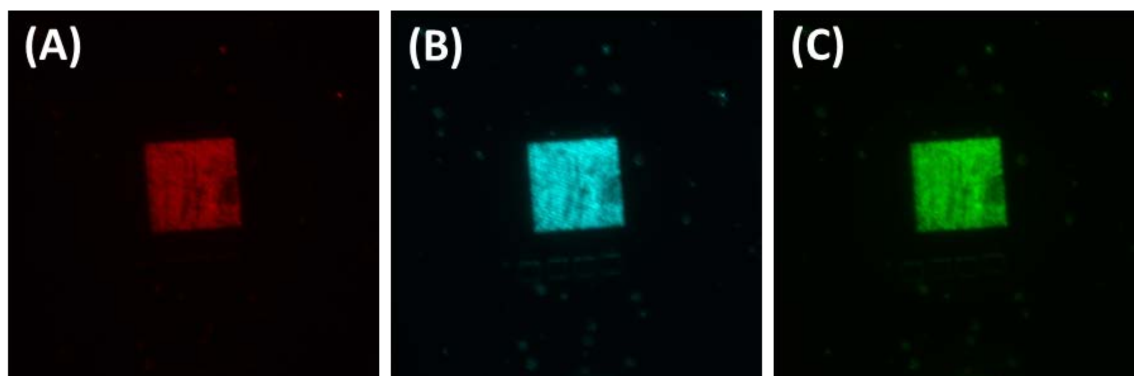

Figure 2.33 Microscopy images of nano-apertures when illuminated by a laser source at (A) 488 nm, (B) 561 nm, and (C) 633 nm.

Laser Wavelength (nm)	488	561	633
Laser Power (%)	28.6	2	4.6
Detector Gain	825	451	439
PMT Quantum Efficiency (%)	~12 (at ~515 nm)	~11	~7.5

Table 2.2 Measurement parameters of Fig. 2.33.

Chapter 3

Surface-Enhanced Raman Spectroscopy (SERS)

Raman scattering, named after Sir C. V. Raman for his discovery in 1928 [76], is a mechanism of inelastic photon scattering by optical phonons. The incident photons interact with molecular vibrational modes, and the photon energy changes accordingly. Figure 3.1 shows the Jablonski diagrams of Rayleigh scattering and two types of Raman scattering [72]. Rayleigh scattering is elastic, and no energy exchange takes place. In Raman scattering, most of the time the incident photons down-shift in frequency by donating energy to the vibration modes; the result is the Stokes waves, which follows the relationship of $\omega_{Stokes} = \omega_{pump} - \omega_{phonon}$ [72]. If the molecules are already in an excited state, for example from prior pumping, the photons can then obtain energy from the vibrational modes for the anti-Stokes emission, which follows $\omega_{anti-Stokes} = \omega_{pump} + \omega_{phonon}$ [72]; an important application is coherent anti-Stokes Raman spectroscopy (CARS) [77]. As a result, the spectrum of Raman scattering bears the unique signature from the molecular vibrational modes, including conformation, bonding types, etc., and can therefore uniquely identify molecules even at a trace amount. In typical applications, the detection range of Raman shift is around 200 – 4000 cm^{-1}, where the unit of cm^{-1} corresponds to 30 GHz. After the invention of lasers, Raman detection has been a popular choice since no sample tagging or staining is required; microscopy applications have also been demonstrated [78, 79]. Compared with fluorescence, where the excitation photons have to be above a certain energy threshold, Raman scattering is relatively insensitive to the incident wavelength; near-infrared illumination can therefore be used in Raman probing for deeper penetration, less photo-toxicity and less scattering loss. In addition, there is no blinking or bleaching in Raman scattering, another benefit over fluorescence measurement. Very little energy is deposited in the Raman process, which is another reason it is an attractive option in biomedical research. Portable or even hand-held Raman-meters are already commercially available, such as those manufactured by SciAps or B&W Tek, Inc.

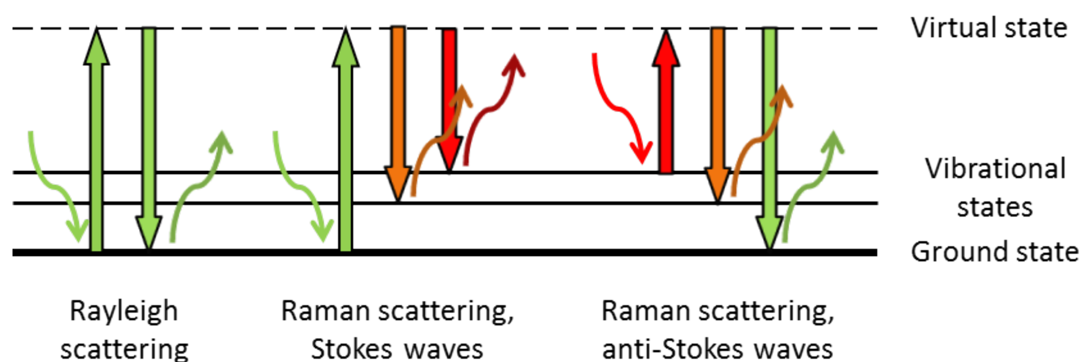

Figure 3.1 Jablonski diagrams of Rayleigh and Raman scattering.

Although electron energy loss spectroscopy (EELS) and far infrared (FIR) spectroscopy can also probe the molecular vibrational spectra, they are much harder to use than Raman spectroscopy. To perform EELS, a high-energy electron source such as a transmission electron microscope or even a synchrotron is needed, which is not straightforward to use and is in no way mobile enough for portable applications. Compared with lasers at optical frequencies, on the other hand, FIR sources are expensive, low-power, and sometimes cumbersome to use. Far-infrared detectors are also slower and less sensitive, and sometimes require deep cooling to the liquid nitrogen or even liquid helium temperature. In addition, materials for FIR optics are more lossy, and they are more difficult to handle since they can be hydroscopic and opaque, which causes issues in terms of shelf life and optical alignment. By contrast, excellent materials and detectors are available in the optical regime, such as quartz for optics and photomultiplier tubes for sensitive detection. Moreover, Raman scattering can take place for some vibrational modes that are not active for FIR absorption [80].

As a third-order nonlinear process, however, Raman scattering is extremely inefficient; the conversion efficiency is typically below 10^{-8} and the scattering cross section σ is on the order of 10^{-29} – 10^{-31} cm^2 [80]. It is arguable that in the face of all the benefits and commercial infrastructures, the only serious drawback of Raman measurement is its weak response. In 1974, Fleischmann *et al.* reported enhanced Raman signals from a silver surface corrugated by chemical etching [81], and subsequently surface-enhanced Raman spectroscopy (SERS) evolved into an important research area. In short, SERS utilizes highly-curved metallic

surfaces to enhance local electromagnetic fields with the help of localized surface plasmon resonance; the Raman efficiency can therefore be greatly increased since the Raman scattering cross section is proportional to the intensity of excitation [80]. With increased efficiency, the required laser power can also be greatly reduced to prevent thermal or photo-toxic damage; larger signal-to-noise ratios and faster acquisition time would also become possible. As a result, SERS substrates have found applications in material sciences, pharmaceutical studies, fine art analysis, biochemical sensing, and so on; even single-molecule detections have been demonstrated [82-84]. For similar reasons, the same kind of metal nanostructures are also used in other applications to enhance fluorescence [85], surface second-harmonic generation [86], and so on.

Similar to the scenario of EOT, in the past the options of making SERS nanostructures were quite limited. Lift-off is one approach [19], but again it is restricted by the lithography resolution, and the metal thickness cannot really exceed one quarter of the patterning polymer. Bottom-up synthesis [21, 83], on the other hand, has achieved good success since various shapes of noble metal nano-clusters could be prepared consistently. The issue with the synthesis approach is that substrates prepared in this way are not uniform; the distance between nano-clusters has a certain distribution, while SERS would only be prominent when the spacing is within a certain range. An exhaustive search on the surface is therefore required to identify the hot spots on the substrate, which can be a huge cost in terms of time and additional equipment. Typically, the SERS-active particles could be fewer than 1% and this number can be as low as $< 0.1\%$ [87]. Designer's freedom is also seriously truncated since it is not known in the design phase where the hot spots would exactly be. Furthermore, a lot of these metal nano-clusters have to be in the liquid phase, which limits their applicability in many occasions. Lots of them are also made of silver, which has a short shelf life since Ag can either oxidize or react with sulfur-based compounds.

To make SERS substrates really cost-effective, a wafer-scalable production method is called for and the SERS-active spots have to be deterministic instead of stochastic. Although some researchers were attempting top-down fabrication of SERS structures, none of them has really achieved uniform enhancement areas so far. For example, Schmidt *et al.* started with

nanopillars coated with metal, and then drew the pillars together with capillary force from liquid in order to create the tiny gaps required for effective SERS [88]. While the process can be done on the whole wafer, the search for stochastic hot spots (i.e., where pillars collapse together) is still unavoidable. In this work, a uniform and wafer-scalable approach is presented; within each area of nano-patterns, the SERS enhancement can be equally large and the hot spot search is no longer necessary, which corroborated the reproducibility of the approach. Although Ag has slightly better plasmonic response due to its lower material loss [11], Au was chosen as the metal of choice since it is more stable and inert, and therefore enjoys a much longer shelf life and better compatibility with various bio-molecules. Furthermore, Ag does not work with the step of thermal reflow, which is essential in creating extremely small gaps uniformly in an area.

This chapter first shows the nanofabrication of SERS structures. The starting point is similar to the method as used in EOT nanofabrication, and the critical step of thermal reflow is discussed. The Raman enhancement is then demonstrated with thiophenol as a bench mark; with numerical simulation to confirm the configurations of SERS-active spots, enhancement factors can then be properly defined and calculated. To prove the generality of the platform, the Raman spectrum of tracheal cytotoxin was measured without any sample preparation. With chip functionalization, on the other hand, the binding dynamics and temperature response could be easily resolved between thrombin and anti-thrombin aptamers. Finally, the detection of hydrogen sulfide, an extremely hazardous gas, is discussed with experimental data from ethyl mercapatan, a similar molecule. Some part of the contents in this chapter was presented on the Inaugural Caltech Medical Engineering Industry Day (October 29th, 2014) and in the 2014 IEEE EMBS Micro and Nanotechnology in Medicine Conference [52].

3.1 Fabrication

The fabrication sequence is shown in Fig. 3.2, the first part of which is similar to the EOT nanofabrication in Fig. 2.13: (A) e-beam lithography with Al_2O_3 deposition as the hard mask, (B) pseudo Bosch etching, (C) thermal oxidation, (D) Au sputtering, and (E) thermal reflow of gold. The thermal reflow is the most critical part in the fabrication, and will be explained in detail in the following section. While the top-down lithography process allows various shapes

of nanostructures to be created, it was found out that nanopillars performed better for the SERS applications. Nanopillars are thus the structures to be discussed in the following sections.

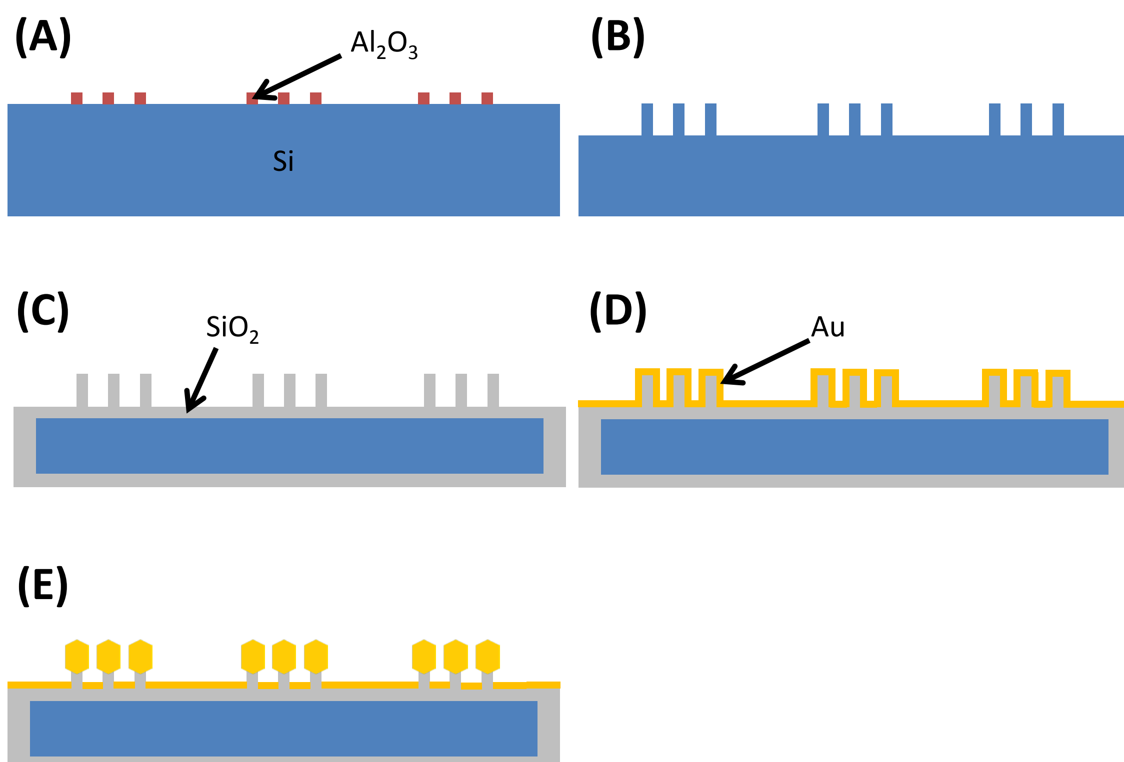

Figure 3.2 Fabrication sequence of SERS nanostructures on silicon.

3.1.1 Thermal Reflow of Au

Gold does not adhere well on many substances, including silicon dioxide. Without an adhesion layer such as Ti or Cr, deposited Au would easily come off from other materials. In the case of silicon dioxide, even a thin layer of Ti does not make the adhesion extremely durable, and Au would start to reflow at an elevated temperature [89]. The temperature and duration of the treatment turned out to be within the capabilities of common rapid thermal annealing (RTA) machines, and in this work the processing was done with a Jipelee Jetfirst 150 Rapid Thermal Annealer. Although the machine has the ability to pump down the chamber

into rough vacuum, such an additional step was not necessary thanks to the chemical inertness of Au. The forming gas of 95% nitrogen and 5% hydrogen was used instead.

A few parameters are now available for fine-tuning: pillar diameter, pillar spacing, pillar height, Au thickness, RTA ramp-up speed, thermal reflow temperature, thermal reflow duration, and RTA ramp-down speed. Depending on the optimization of these factors, various results of thermal reflow would be possible. Typically 675 °C for a few minutes would be enough for satisfactory reflow. In Fig. 3.3 (A) the reflow was incomplete, so that there is still some sidewall connection between the Au portions on the pillar top and the bottom Au layer. In Fig. 3.3 (B) the separation was complete, although the gold on the sidewall did not further aggregate into spherical shapes. Figure 3.3 (C) is a good example of thermal reflow

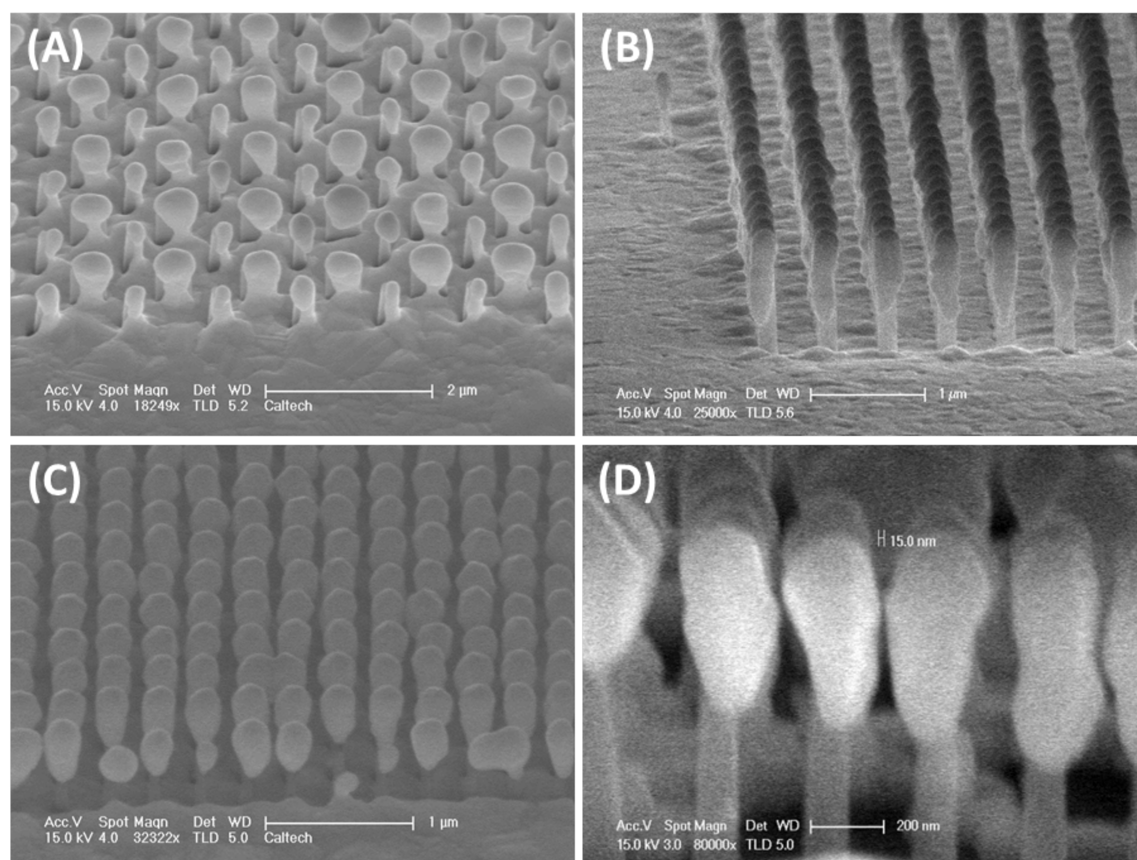

Figure 3.3 Different results from various parameters of thermal reflow. (A): incomplete separation; (B): separated but not bulbed; (C): good examples of nano-bulbs; (D): a 15 nm gap between nano-bulbs.

when the gold layer on the nanostructures turned into nano-bulbs; this is the desirable result for SERS applications. This bottom-up process makes it possible to fabricate Au nanostructures with features that go beyond the resolution of lithography tools; moreover, by tweaking the process parameters, the spacing between nano-bulbs can be tailored to the designer's choice. The spacing can be easily made anywhere between 5 and 50 nm, and in Fig. 3.3 (D) a 15 nm gap was easily identified in the SEM micrograph. It should be noted that such a small gap was repeatable across the entire pattern, and there is no need to perform an exhaustive search in order to find a good spot as in the case of synthesized metal clusters.

Figure 3.4 further illustrates the bottom-up nature of the thermal reflow process. The chip was exposed to liquid before Au sputtering, so some nanopillars were bent by the capillary force. In Fig. 3.4 (A), some nanopillars leaned to the neighboring one, and therefore after the RTA processing it can be seen that some nano-bulbs were "shared" by two nanopillars. When one nanopillar tilted to the side, as shown in Fig. 3.4 (B), it was still able to wick the gold nano-bulb to its tip.

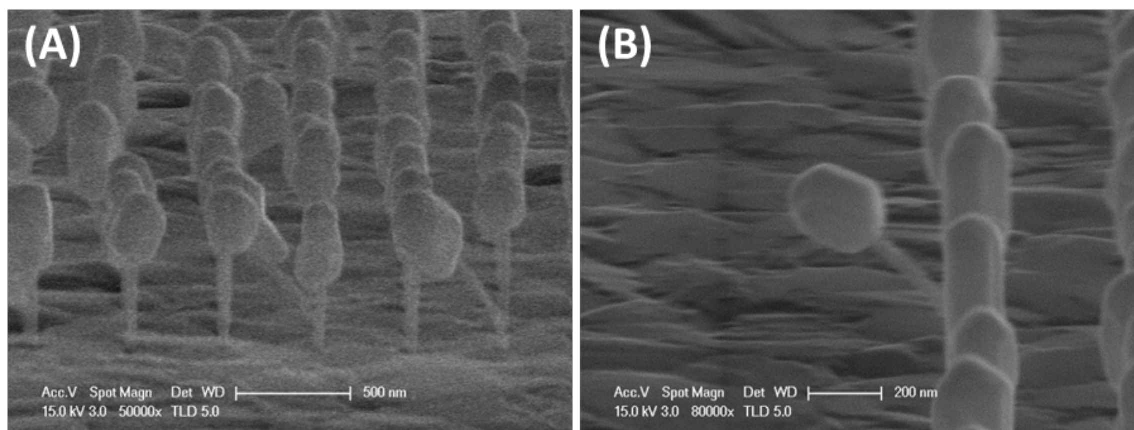

Figure 3.4 Formation of nano-bulbs when (A) some nanopillars tilted to the other one, and (B) one nanopillar leaned to the side.

Again, if the annealing temperature was excessively high, the bottom Au layer would congregate together and openings would result, as shown in Fig. 3.5. If the gap between Au nano-bulbs remains small enough, however, the chip is still usable since the integrity of the Au layer is not so critical as in the case of EOT applications.

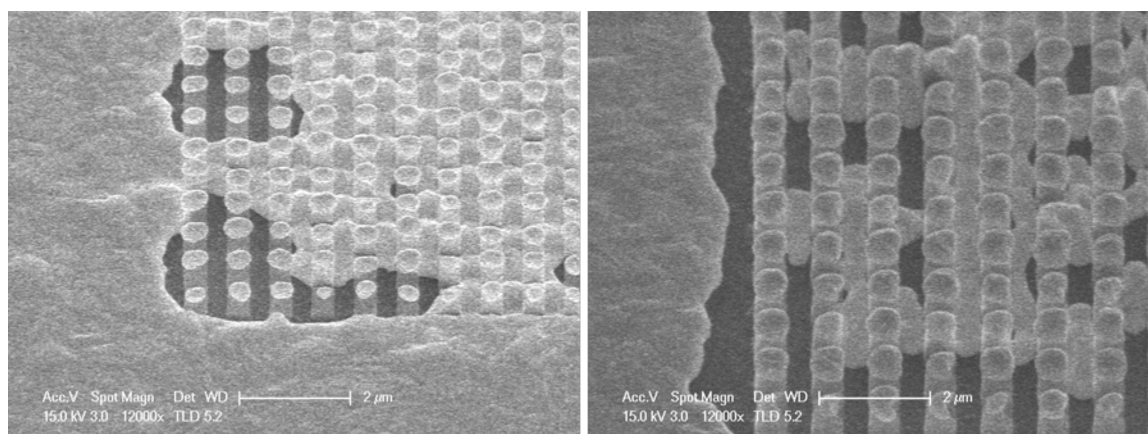

Figure 3.5 Results of excessive thermal processing on SERS chips.

3.1.2 Facilitating the Thermal Reflow

In addition to 3D sculpting with the pseudo Bosch etch, there is also a technique that alters the shape of nanopillars to facilitate the thermal reflow. After thermal oxidation, the chip can be dipped very briefly in BHF to round out the edges of the pillar top, which would be etched faster than the other regions due to its larger surface-to-volume ratio. Figure 3.6 (A) shows the result when the chip was immersed in BHF for about 2 seconds, and Fig. 3.6 (B) ~6 seconds. The pillar top is obviously more rounded in Fig. 3.6 (B) than in (A).

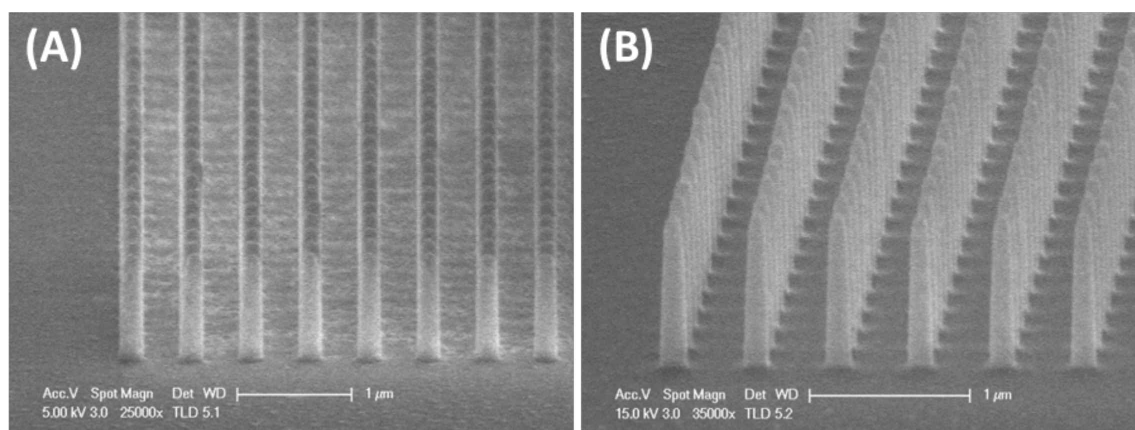

Figure 3.6 Oxidized nanopillars after a brief immersion in BHF for (A) ~2 seconds and (B) ~6 seconds.

Such a treatment was found out to help the annealing process, which is illustrated in Fig. 3.7. In the figure, (A), (C), and (E) are from a chip that was dipped in BHF for ~2 seconds, while (B), (D), and (F) for ~6 seconds before Au sputtering and annealing. Figures 3.7 (A) and (B) are from the same nano-pattern; so are (C) and (D), and (E) and (F). Since both chips

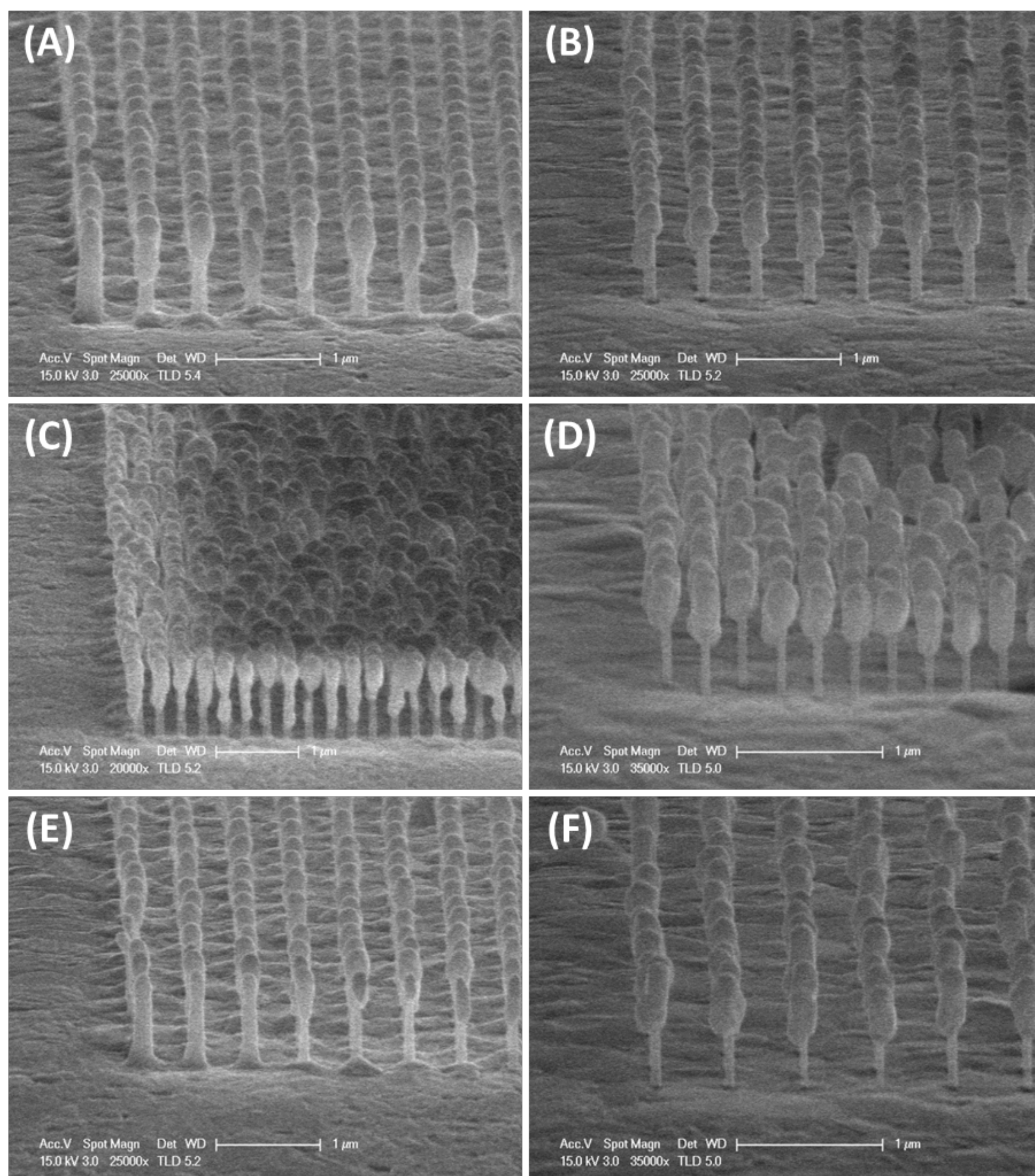

Figure 3.7 Thermal reflow results from chips that were treated in BHF for different durations of time.

were in the same batch for pseudo Bosch dry-etching, Au sputtering and thermal reflow, the only difference would be the immersion time in BHF. By comparing the figures, the reflow was indeed more complete for the chip with ~6 seconds of BHF treatment. In particular, in Figs. 3.7 (A) and (E) there is incomplete separation of Au on the nanopillars around the corner, while in the counterparts of Figs. 3.7 (B) and (F) there is no such an issue. Depending on the design of nanopillars, however, this technique should be used with caution. If the pillar diameter is small in the first place, excessive exposure to BHF may etch away the thin pillars completely from the side.

3.1.3 Optional Masking of Substrate

Sometimes it may be preferable to mask the general Au substrate for a certain applications; for example, if the Au nano-bulbs are to be functionalized by bio-molecules, masking the substrate could improve the binding efficiency and specificity since the flat Au layer does not contribute to SERS signals. This can be easily done in a similar way as described in Section 2.1.6 by coating a resist layer onto the chip, followed by oxygen plasma ashing to the desired level. Figure 3.8 shows some examples where only the Au nano-bulbs are exposed while the rest of the chip is covered in PMMA.

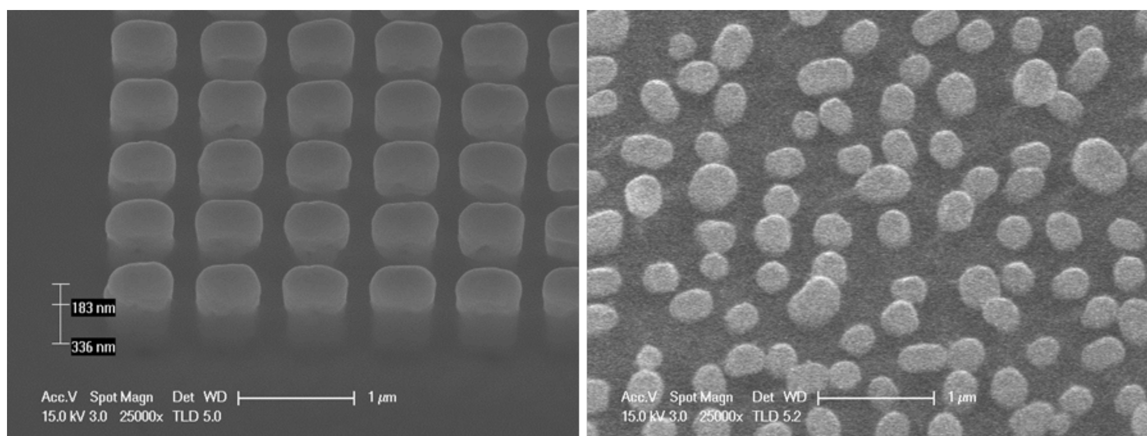

Figure 3.8 SERS structures with a PMMA layer masking the bottom substrate.

3.2 Characterization with Thiophenol

Thiophenol (C_6H_6S), also known as benzene thiol, is a common model system to demonstrate SERS due to the high affinity of the –SH group to noble metal surfaces and its formation of relatively stable monolayers on such surfaces [90]. Moreover, it has several distinct Raman peaks that can be easily identified for numerical analysis. SERS chips were first treated with oxygen plasma for 5 minutes to remove any possible organic compounds remnant on the surface, followed by 6 hours of immersion in 1 mM of thiophenol in ethanol. After the incubation was done, chips were rinsed with ethanol and then deionized (DI) water, and allowed to dry under a nitrogen flow. For reference samples without SERS nanostructures, 65 μl of undiluted thiophenol was added onto the chips, which were then placed in a Bio-Rad incubation chamber after being sealed with a piece of cover glass.

For commercially available systems, common choices of the laser wavelength for Raman measurements are 532, 633, and 785 nm. The wavelength of 633 nm was chosen for this work since 532 nm is too close to the absorption band of Au nanostructures [91], and the choice of 785 nm would potentially limit the detection range of Raman shifts. For example, if a wide scan for up to 3500 cm^{-1} is desired, this would correspond to the optical wavelength of 1082 nm, and the quantum efficiency of commercial detectors (typically made of Si) would drop significantly already. Furthermore, while Raman scattering does not have a cutoff excitation wavelength as in the case of fluorescence, its efficiency rolls off as a function of λ^4 [72]. The use of longer excitation wavelengths then becomes a trade-off; it provides less photo-toxicity in bio-molecules and better penetration depth for *in vivo* applications, but the Raman efficiency also decreases. Increasing the excitation wavelength to the blue or even UV region, on the other hand, helps with the Raman scattering but would potentially damage the sample and excite fluorescence. The use of 633 nm is thus a good middle ground in terms of all these considerations. For Raman applications, the laser linewidth is to be as small as possible so that the measured spectra would not be a convolution between the laser bandwidth and the molecular vibrational modes. A gas laser is therefore a very good option here, and for the wavelength of 633 nm the He-Ne laser is readily available, which emits at 632.8 nm with a narrow linewidth of ~1.5 GHz (or 0.05 cm^{-1}) [92] without special arrangements such as

additional line narrowing optics. If a He-Ne laser is unavailable, a diode laser may be substituted if a high-quality line filter can be used to reduce the linewidth.

The measurements were done on a Renishaw inVia Raman microscope with a 50X objective and a He-Ne laser as the excitation source. The Raman Stokes waves were first steered through an edge filter to block the backscattered laser beam, then spectrally scattered by a 1800 line/mm grating, and finally recorded by a CCD detector that can be thermoelectrically cooled to -70 ^{o}C to increase the sensitivity. A spectral resolution of 0.2 cm^{-1} is available from such a system. Raman shifts in the range from 100 to 3200 cm^{-1} were collected, and for thiophenol signals from SERS nanostructures, typically only 0.01 – 1 % of the laser power (out of 100 mW) would be sufficient for an integration time of 10 s or even shorter. This is stark contract with regular Raman measurements without SERS, where a single scan could take minutes at a laser power of 500 mW [93]. The raw signals counts from SERS and regular Raman measurements, both at an integration time of 10 s, are plotted in Fig. 3.9; the laser power was 0.1% for the SERS curve and 5% for the regular Raman. Despite the huge contrast in laser power and thiophenol concentration, the signal strength was still comparable in raw counts. The peak at 2568 cm^{-1}, which corresponds to the –SH stretching mode [94], was only observed in the regular Raman measurement but not in the SERS, since during the formation of the Au-S bonds the hydrogen atoms were donated [95]. In the SERS spectrum, on the other hand, vibrational modes associated with the Au-S bonding could be observed at 473 and 1469 cm^{-1} [96-98]. The rest of the spectra were similar between regular and SERS signals, like those peaks associated with the C-S bonds around 412 cm^{-1} [99] and 700 cm^{-1} [100], out-of-plane C-C-C and C-S stretching around 615 cm^{-1} [90], C-C bonds around 992 cm^{-1} [101] and 1580 cm^{-1} [102], out-of-plane C-H stretching around 1021 cm^{-1} [90], and in-plane C-C-C and C-S stretching around 1072 cm^{-1} [90]. As will be explained with further details in the following section, numerical simulation indicated that the only a very small portion on the nano-bulbs would be SERS-active, while for the regular Raman scattering the entire laser spot contributed to the signals.

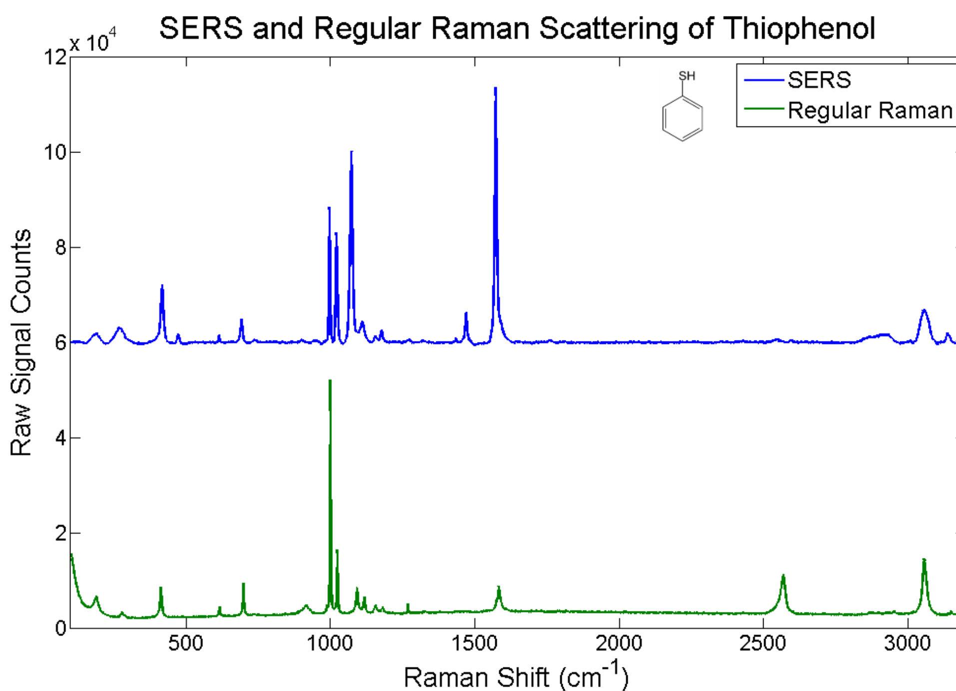

Figure 3.9 SERS and regular Raman spectra of thiophenol with an offset between data; the skeletal formula of thiophenol is shown next to the legend.

To double check the homogeneity of the SERS nanostructures, a raster scan was performed on the region of nano-patterns at a step size of 5 μm, and the signal strength at 1575 cm^{-1} was recorded, which corresponded to the breathing mode of the aromatic ring [103]. The variation of signal strength across the active region, which is 50 by 50 μm in size, was less than an order of magnitude. This result corroborated the advantage of top-down designing over stochastic assembly, in which the deterministic process ensures controllable and consistent features in a large area instead of scattered hot spots.

3.3 Simulation and Enhancement Factors

3.3.1 MEEP Simulation

Before the enhancement factor can be appropriately discussed, FDTD simulation was performed to investigate and define the regions that are SERS-active on the nano-bulbs since the area will be directly related to the numerical value of the enhancement factor. MEEP, a finite-difference time-domain (FDTD) simulation package for photonics developed at

Massachusetts Institute of Technology, was used in this work to simulate the behaviors of SERS nanostructures. Intrinsically MEEP can be installed on a computation cluster with multiple cores or even multiple processors, and is therefore very convenient for pinning down the simulation conditions fast before running a large-scale parameter scan. The nano-bulbs were simulated as Au spheres on top of SiO_2 nanopillars; relevant physical dimensions, such as the sphere diameter and the pillar width, were statistically acquired from the SEM micrographs from which the SERS data were obtained. For the dielectric permittivity dispersion of Au, the Lorentz-Drude model was used with parameters from [104]. A linearly-polarized plane wave at 633 nm was defined to be the excitation source, and the simulation was repeated for the excitation wavelengths of 675 and 724 nm to verify the spatial overlapping of local field enhancement in the Raman process, which correspond to 983 and 1986 cm^{-1}, respectively. The former corresponds to the thiophenol C-C mode [101], and the latter was to test the degree of field enhancement when the wavelength was sufficiently away from the excitation. A plain Au surface without nanostructures was also simulated (not shown here) for the same conditions to double check the lack of local field enhancement. The simulation grid size was 2 nm. For periodic structures like these, only one unit cell has to be simulated and automatic cascading in MEEP can be achieved by specifying

```
(set! k-point (vector3 0 0 0))
(set! ensure-periodicity true)
```

in the control file. Moreover, the perfectly matched layer (PML) was only specified in the z directions. Here the `k-point` command specifies the (k_x, k_y, k_z) components so that the field will follow the relationship of

$$\mathrm{E}(x + d_x, y, z) = e^{ik_x d_x}\mathrm{E}(x, y, z) ,$$

where d_x is the cell size in the *x* direction. A similar relationship holds for *y* and *z* directions. In this case the PML was only placed in the *z* directions, so effectively an infinite 2D array would be simulated in MEEP. If the pattern and the polarization direction would allow it, symmetry in MEEP can be invoked to accelerate the computation.

Figure 3.10 (A) shows the *xz* cross section of the electric field strength $|E|$ from an excitation source of 633 nm polarized along the *x* direction; local field enhancement was indeed observed between nano-bulbs. Since the Raman scattering efficiency is proportional to

$|E_{excitation}|^2|E_{emission}|^2$, which is usually approximated as $|E_{excitation}|^4$ [105], only a small region between the nano-bulbs would be really SERS-active as a hot spot, compared with the entire area within the laser focal spot as in regular Raman scattering. Figure 3.10 (B) shows the *xy* cross section with the highest $|E_{633\ nm}|$ on the nano-bulb surface; again it is evident that for linearly-polarized excitation, there would be only two small hot spots on each nano-bulb. In Fig. 3.10 (C) the excitation of 675 nm was simulated, and there is decent overlap between the local field enhancement at 633 nm and 675 nm, which is a good indicator of efficient Raman scattering. When the $|E|^2$ peak strength are compared, the value at 675 nm was calculated to be ~14.5% of the value at 633 nm, while the value at 724 nm was only ~0.77% of that at 633 nm. These numbers indicate that for a specific SERS nano-bulb structure, there is a range of wavelength that would be well enhanced.

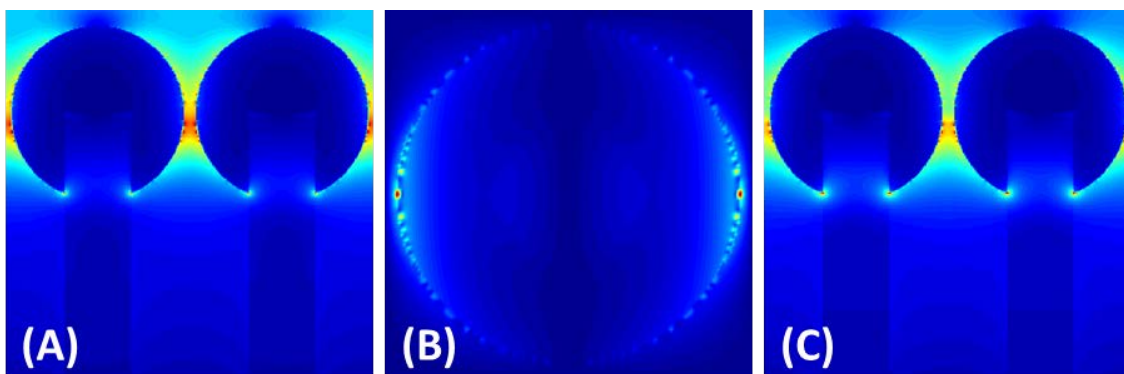

Figure 3.10 Electric field strength from MEEP simulation results of nano-bulbs with dimensions from actual chips. (A) and (B) are the *xz* and *xy* cross sections from an excitation source of 633 nm; (C) is the *xz* plot from 675 nm.

The grid points were identified for further calculation if they sit right on top of the Au nano-bulb surface. If the spherical coordinates are defined with the center of the Au nano-bulb as the origin, the region between $\theta = 30^\circ$ and $\theta = 150^\circ$ was selected to be the range of interest. The values of $|E_{633\ nm}|^4$, $|E_{633\ nm}|^2|E_{675\ nm}|^2$, and $|E_{633\ nm}|^2|E_{724\ nm}|^2$ were then calculated and summed in this range of θ and for the whole φ of $0^\circ - 360^\circ$. Since there are two hot spots on each nano-bulb for linearly-polarized light, the summed number was divided by 2. The effective SERS area A_{eff} can then be defined as

$$A_{eff} = \frac{1}{2}\frac{\sum_{\theta,\varphi}|E_{633\ nm}|^4}{|E_{633\ nm}|^4{}_{peak}},\ \text{or}\ A_{eff} = \frac{1}{2}\frac{\sum_{\theta,\varphi}|E_{633\ nm}|^2|E_{emission}|^2}{|E_{633\ nm}|^2|E_{emission}|^2{}_{peak}}.$$

The calculated areas are then around 1700, 1900, and 1500 nm^2 for the scenarios of $|E_{633\ nm}|^4$, $|E_{633\ nm}|^2|E_{675\ nm}|^2$, and $|E_{633\ nm}|^2|E_{724\ nm}|^2$, respectively. The numbers agree well with each other, which again indicate decent overlapping of local field enhancement between the excitation and the emission wavelengths. These values also provide a good estimate of the SERS area from each nano-bulb for the calculation of the enhancement factor, as discussed in the next section.

3.3.2 Definition and Calculation of Enhancement Factors

In the SERS literature different enhancement factors from ~10^6 to ~10^{14} have been reported [82, 106], which resulted in some debate regarding how much enhancement would be necessary for SERS to be usable without being buried in the background noise. One reason for such a discrepancy is due to different definitions of enhancement factors, so that there was no common bench mark for comparing different results of experimental measurement or theoretical calculation. For numerical values to be fairly discussed and compared under the same framework, the definitions of enhancement factors from [107] are used in this section.

Referring to [107], definitions of enhancement factors include the single molecule enhancement factor (SMEF), the SERS substrate enhancement factor (SSEF), the analytical enhancement factor (AEF), and other less common definitions. The SMEF is defined as [107]

$$SMEF = \frac{I_{SERS}^{SM}}{\langle I_{RS}^{SM}\rangle},$$

where the numerator is the SERS intensity seen from a molecule's point of view, and the denominator is the average molecular response from unenhanced regular Raman scattering. As a result, the SMEF is more convenient for theoretical calculation or *ab initio* simulation. The SSEF is defined as [107]

$$SSEF = \frac{I_{SERS}/(\mu_M \mu_S A_M)}{I_{RS}/(c_{RS} H_{eff})} \Rightarrow \frac{I_{SERS}/N_{Surf}}{I_{RS}/N_{Vol}},$$

where μ_M is the surface density of SERS-active nanostructures, μ_S is the molecule density on the metal surface, A_M is the surface area of the metal substrate, c_{RS} is the molecular concentration for regular Raman measurement as the reference, and H_{eff} is the effective height

of the scattering volume. This corresponds to the widely-used definition of the enhancement factor, listed as the final term in the equation, where the ratio is calculated between the average signal intensity seen by the SERS molecules, N_{Surf}, and the counterpart in the interaction volume of regular Raman, N_{Vol}. The SSEF definition is useful in experiments since the maximum enhancement from individual molecules is typically not measured, and instead a collection of molecules are probed for the averaged signal. The SSEF is, however, dependent on the substrate of measurement (and hence the namesake), and may not offer a straightforward comparison between different experiments. The AEF is thus introduced to determine the expected SERS enhancement compared with regular Raman when other experimental conditions are identical, such as the laser power, microscope objective, and so on. It is defined as [107]

$$AEF = \frac{I_{SERS}/c_{SERS}}{I_{RS}/c_{RS}},$$

where c_{SERS} represents the possibility of a different concentration of measurement compared with the value of c_{RS} in unenhanced Raman.

For the calculation of enhancement factors, some experimental parameters have to be obtained. To determine the laser spot size, the knife-edge method [108] was used with a piece of silicon wafer as the "knife." The silicon piece was placed on the sample holder, brought to focus, and moved laterally to be slightly outside of the field of the view. The sample holder, which was motorized and could be remotely actuated by the control interface, then started to shift laterally and bring the Si sample closer to the laser focal spot in small steps. The control interface would record the Raman signal in the meantime, especially the strong peak around 520 cm^{-1} for silicon [109]. By analyzing the curve, the size of the focal spot can be determined by the abruptness of signal increase when the silicon wafer was brought back to the laser spot; the diameter was calculated to be 1.5 μm. With this value available, the total number of thiophenol in the focal region could then be calculated for the normal Raman measurement. After taking consideration of other parameters such as the effective SERS area size on nano-bulbs, difference in laser power and thiophenol concentration, etc., the SSEF was calculated to be greater than 10^{10}. For the SSEF calculation, the result was ~3.5 x 10^{10} if the Raman peak at

1575 cm^{-1} was considered, and the value would be around 1 – 5 x 10^{10} if other peaks in the spectra were selected instead.

3.4 Tracheal Cytotoxin (TCT) Measurement

To prove the generality of this SERS platform, tracheal cytotoxin (TCT) was selected to demonstrate the easy and straightforward use of these chips. TCT is a glycopeptide secreted by a certain pathogenic bacteria, such as *Bordetella pertussis* (causing whooping cough) and *Neisseria gonorrhoeae* (causing gonorrhea) [110, 111]. In gram-negative bacteria like these, TCT is also a component of the cell walls [111]; this arrangement and the TCT structure can be found in Figs. 1 and 3 of [111], respectively. Tracheal cytotoxin kills ciliated cells and causes them to protrude from the epithelium; it can also disrupt the mechanism of the immunity system or the deep sleep phase [112]. If early detection of trace amounts of TCT can be available, treatment can be administered before the damage and the symptoms get serious. In the past, however, the full Raman spectrum of TCT was unavailable.

The TCT samples were obtained from the laboratory of Prof. Edward Ruby from the Department of Medical Microbiology & Immunology, University of Wisconsin-Madison. Droplets of 2 μl from this 100 nM of TCT in buffer solution was dispensed onto the SERS chips, which were allowed to dry on a hot plate set to 75 ^{o}C. The use of a hot plate was only to accelerate the drying process, and played no other role in the sample preparation. Raman spectra from the chips were then acquired as usual. The measured Raman spectrum, extending from 100 to 3200 cm^{-1}, is shown in Fig. 3.11. To the author's best knowledge, this is the first time a full scan of Raman spectrum from TCT was obtained; furthermore, no special sample preparation or chip functionalization was required. Several vibrational modes expected from the TCT structures could be observed: glycoside-related peaks at 594 cm^{-1} [113], 704 cm^{-1} [114], and 1124 cm^{-1} [115]; peak at 843 cm^{-1} attributed to alanine [116]; amide III at 1285 cm^{-1} [115, 117, 118]; amide II at 1572 cm^{-1} [117-119]; amide I at 1635 cm^{-1} [117-119]. Descriptions and diagrams about the amide I, II, and III modes can be found in [120]. This spectrum can be further compared with those obtained from gram-negative bacteria such as *Escherichia coli*, *Klebsiella oxytoca*, *Klebsiella pneumonia*, and *Citrobacter freundii*. The spectra share some common features, such as the structures from ~1200 to ~1800 cm^{-1} (see Fig. 3 in [31]), the humps

around 700 cm^{-1} (see Figs. 1-3 in [114]) and around 500 cm^{-1} (see Figs. 8 & 9 in [121]), and so on, thus authenticating the measured spectrum was truly from TCT. The Au nano-bulbs therefore serve as a generic platform of SERS measurement with excellent bio-compatibility.

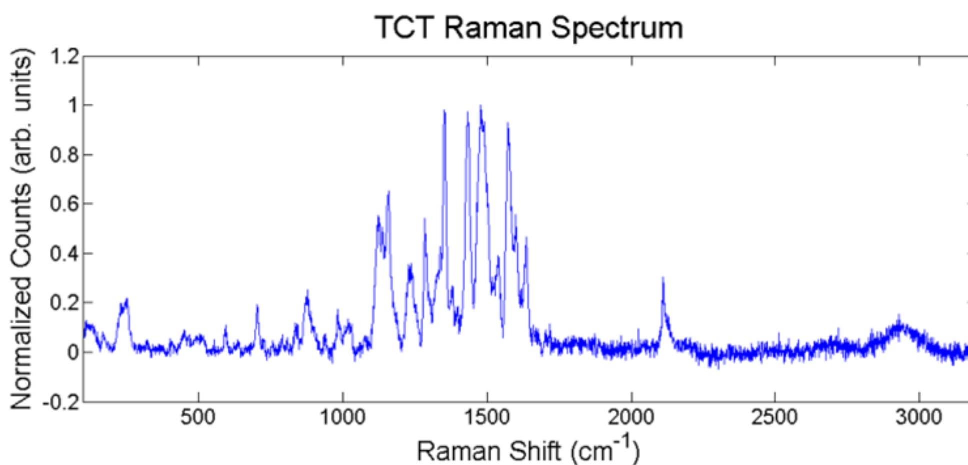

Figure 3.11 Extended Raman spectrum of tracheal cytotoxin.

3.5 Aptamers and Thrombin

Even though the TCT spectrum could be obtained simply by drying up the sample on the chip, specificity of these SERS chips can be further enhanced by functionalizing the chip surface. The choice of Au offers many advantages in this case, since Au does not react with bio-molecules and change their chemical composition. On the other hand, the strong affinity between gold and sulfur provides a good opportunity to attach bio-molecules to the Au nano-bulbs if they can be thiolated. Since Raman scattering picks up vibrational modes from molecules, it is anticipated that details of conformation changes, binding events, etc. would be reported in the spectrum. This is one distinct advantage of Raman spectroscopy over other methods like refractive index sensor [122] or electronic potentiostat [123], whose reading is only one-dimensional.

3.5.1 Aptamer Attachment

Aptamers are short strands of oligonucleotides or peptides that have found wider and wider use in bio-sensors in recent years [124]. There are several advantages of using aptamers: they can be chemically synthesized for mass production; they can be designed and selected for

various affinity, specificity and functionalization to various molecules; they are stable (especially when compared with antibodies) with a long shelf life; and finally, once their sequence is known the information can be passed out for reproduction elsewhere, just like the dissemination of computer codes. For bio-compounds of clinical interest, aptamers have been developed to target thrombin [125] for monitoring coagulation and dopamine [126] for probing the endocrine system. For assessing the possibility of immunity issues or tumor growth, aptamers are also available for lysozyme [124], interferon γ [127], prostate specific antigen (PSA) [128], vascular endothelial growth factor (VEGF) [129], and heat shock factor 1 (HSF1) [130].

In this work, anti-thrombin aptamers were chosen so that their binding with thrombin could be studied at the same time. Two types of anti-thrombin are available: TBA [125] and HD22 [131]; the former was used for the experiments in the following sections. The TBA aptamers are 15-mer single-strand deoxyribonucleic acid (ssDNA), originally developed as the sequence of 5'-GGTTGGTGTGGTTGG-3' [125] to bind onto the exosite I of thrombin when they form the quadruplex structure [132]. For attachment to the Au nano-bulbs, thiolated TBA aptamers were purchased from Genelink for the sequence of (5'-SH-$(CH_2)_6$-GGTTG GTGTG GTTGG-3'), which was used to make a stock solution at 1 mM. The solution was kept in a fridge at 4 ^oC until used, when 5 μl of this solution was added to 95 μl of 0.1 M phosphate buffer (K_2HPO_4) at pH = 8 and 10 μl of 0.1 M dithiothreitol (DTT) in 0.1 M phosphate buffer. After thorough mixing, the solution was incubated at room temperature for 2 hours, and then passed through a desalting column purchased from Fisher Scientific. Deionized water was added to the buffer exiting the column for three times; during the third rinse, 400 μl of DI water was added to 110 μl of the mixed solution of aptamers, DTT and phosphate buffer. When the column was almost empty, 510 μl of the aptamer solution was slowly added into the column drop by drop, and the solution was eluted with 500 μl of DI water. The final result would be ~1 ml of 5 μM aptamer solution.

The SERS chips were first treated with oxygen plasma to ash away any possible organic residues, rinsed with IPA and then DI water, incubated with the aforementioned aptamer

solution for ~12 hours, and cleaned rigorously with IPA and then DI water for the removal of excess ligand. To promote the aptamers into the stable G-quadruplex structure, the chips were in 100 mM of potassium chloride (KCl) in phosphate buffer, heated to 80 ^{o}C, and allowed to cool to room temperature. It is know that potassium ions not only stabilize the TBA structure [133], but also increases its effect to inhibit thrombin [131, 134].

3.5.2 Thrombin Binding

Thrombin is a protease that plays a critical role in the coagulation process. Physiologically the presence of thrombin indicates the existence of a blood clot somewhere, and this information may potentially predict the onset of heart attacks or ischemic strokes in the near future [135]. For patients taking medicine for anticoagulation (also a side effect of aspirin), knowing the thrombin level in blood can also help with determining the amount of medication to take. When coagulation starts, however, thrombin is released very rapidly when triggered by the tissue factor into a "thrombin burst [136]," as can be seen in the amplification phase of the coagulation pathways in 3.12, which is an excerpt version replotted from Fig. 8 of [137]. For a blood sample to work, as a result, a decent amount of volume has to be drawn into a tube with clot-preventing chemicals in order for the true thrombin level in the body to be reported, or otherwise it may be buried in the additional signals contributed by the cut. Since this is not desired for constant, long-term monitoring of thrombin level, a probe in the body with non-invasive interrogation would be preferred. Optical readout provides such an opportunity, and hence the motivation of using SERS for thrombin detection.

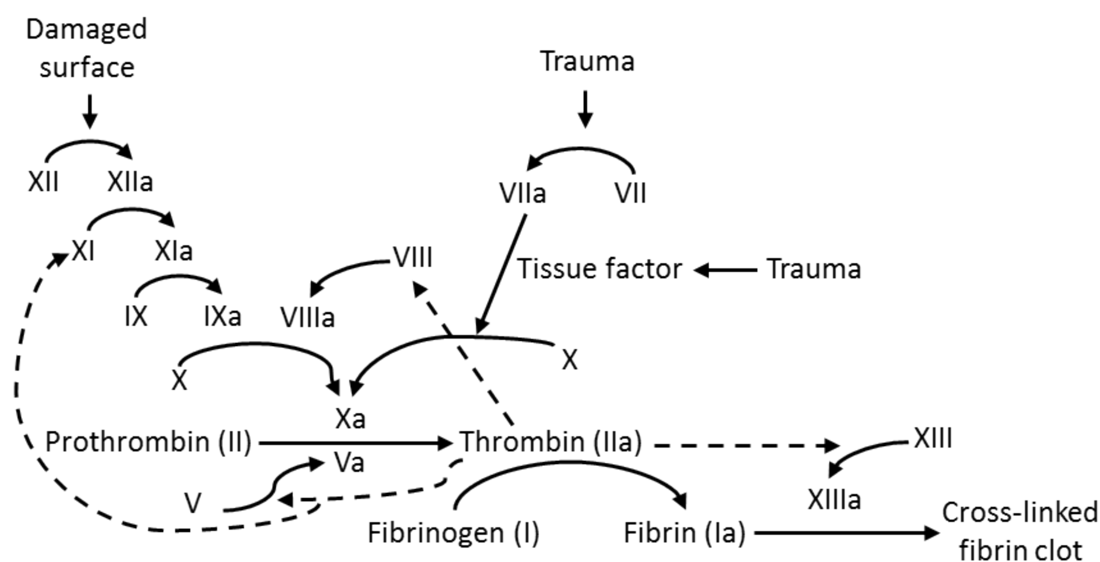

Figure 3.12 Role of thrombin during coagulation *in vivo*.

Figure 3.13 (A) shows the home-built microfluidic chamber for the Raman measurement at different thrombin concentrations. Each SERS chip, functionalized with TBA aptamers, was placed onto a piece of glass slide. Two pieces of Frame-Seal incubation chambers from Bio-Rad, each with inner dimensions of 1.5 cm by 1.5 cm by 300 μm, were stacked on top of each other to make a microfluidic chamber on the glass slide; two Luer stubs (i.e., blunt needles) with an outer diameter of ~630 μm were sandwiched in between on opposite sides as the inlet and outlet of fluid. Since the chip height is ~325 μm, it could be well accommodated in the chamber and a piece of cover glass could be directly placed on top to seal up the chamber without disturbing the chip. Plastic tubes were used to connect one metal microtube to a syringe and the other to waste disposal; since the inner diameter of the plastic tube was 0.023 in., or ~585 μm, the connection remained leakproof during the experiments. The entire module was then placed onto the microscope holder, and the Au nano-bulbs were brought to focus. Human α-thrombin was purchased from Sigma-Aldrich and mixed in bovine serum albumin (BSA) solution (0.1% volume ratio, pH = 6.5) for the stock solution at a concentration of 100 NIH units per ml. The stock solution was stored in a freezer at -20 °C in plastic microcentrifuge tubes before use. After the injection of 0.1% BSA solution or

diluted thrombin solutions at 1, 10, or 100 pm, the Raman spectra were measured with the usual procedures. Figure 3.13 (B) shows the normalized spectra at different conditions. The presence of thrombin immediately changed the Raman spectrum; as can be seen in the figure, the top curve of pure aptamers differs dramatically from the other three, especially in the range of 1200 – 1400 cm^{-1}. When a higher concentration of thrombin was in the chamber, the

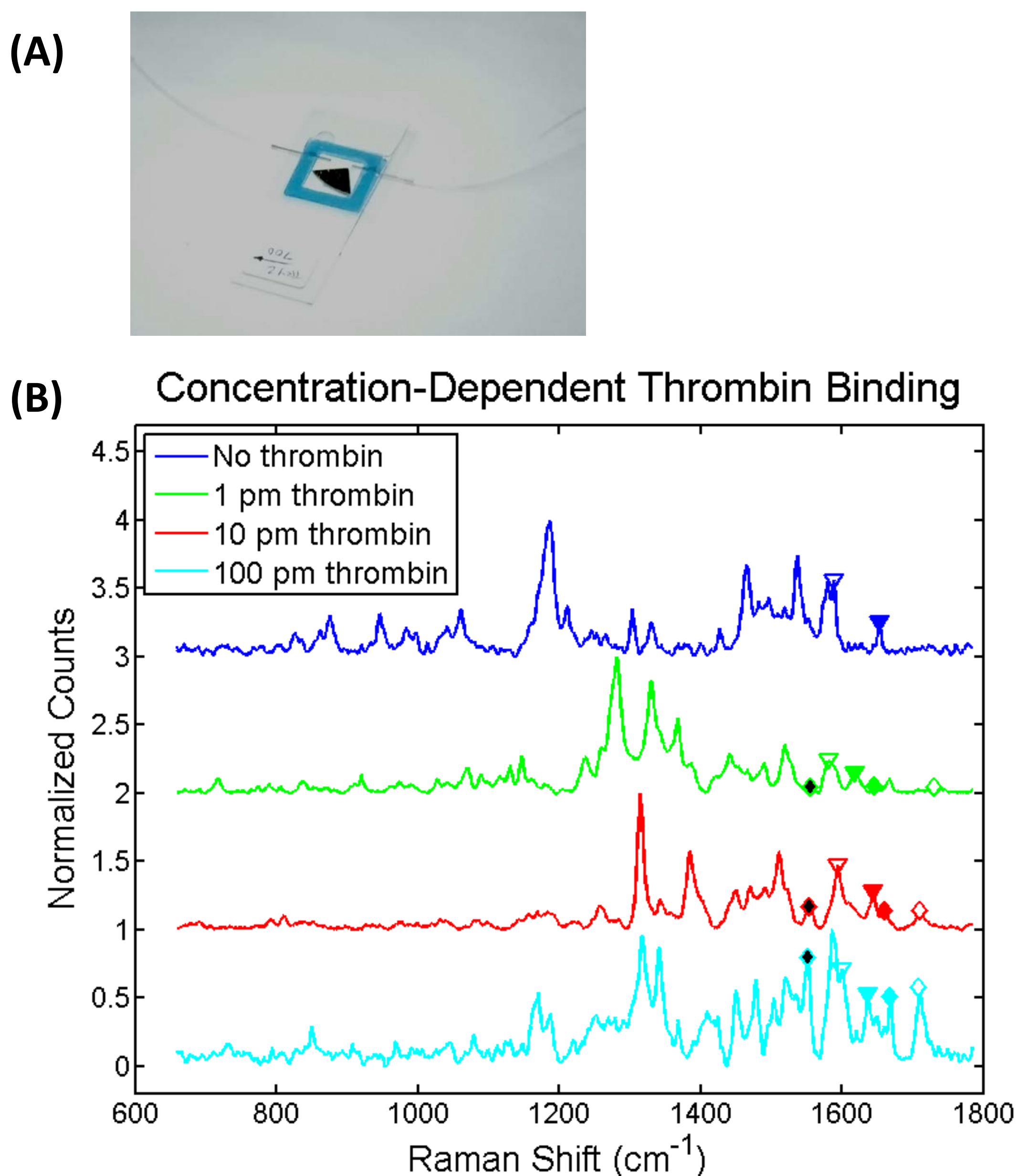

Figure 3.13 (A) Customized chamber on glass slide for injection of thrombin solution at various concentrations. (B) Raman spectra of TBA aptamers with no thrombin and different thrombin concentrations of 1, 10, and 100 pm.

Raman spectrum would experience a general redshift since now a larger number of thrombin molecules were attached to aptamers. Intuitively, this is equivalent to the condition when additional mass (i.e., thrombin molecules) is attached to a mechanical oscillator (i.e., vibrational modes) with a fixed spring constant (i.e., bonding strength), and the natural oscillation frequency of $\omega = \sqrt{k/m}$ would decrease as a result.

Quantitative analysis is also possible in SERS when peaks corresponding to known vibrational modes are compared against each other. This technique eliminates the necessity of a separate measurement on a control sample for calibration, and will be very convenient for applications like *in vivo* sensing. Referring to Fig. 3.13 (B), two peaks from aptamers (labeled by inverse triangles) and three peaks from thrombin (labeled by diamonds) were chosen for this comparison. The peaks chosen for aptamers were related to the guanine C2=N3 mode around 1580 cm^{-1} [138], and the guanine C6=O6 mode around 1650 cm^{-1} [138]; the peaks for thrombin were amide II around 1550 cm^{-1} [117-119], amide I around 1645 cm^{-1} [117-119], and another C=O mode around 1710 cm^{-1} [139] attributed to thrombin (see Fig. 3 in [140]). Since the chips were functionalized with TBA aptamers in the same way, this kind of comparison eliminated the influence of fluctuations in experimental parameters between different runs, such as the distance between the Au nano-bulbs and the microscope objective. The results are plotted in Fig. 3.14; ratio 1 is the comparison between the peak marked in black diamond and the peak in transparent inverse triangle; ratio 2 is between the peak in solid diamond and the peak in solid inverse triangle; ratio 3 is between the peak in white diamond and the peak in solid inverse triangle. As can be seen in the log-log plot, the ratios approximately follow a straight line, which is anticipated. It is also observed that as the concentration got lower, the 3 calculated ratios would be more spread out. This is because at concentrations like 1 pM, statistically there would only be a few molecules in the laser spot and the signal fluctuation would be greater due to the discrete nature of molecular presence. At a higher concentration enough molecules could be probed at once within a single laser spot, and the signal would be averaged by itself and therefore more consistent among different peak strengths.

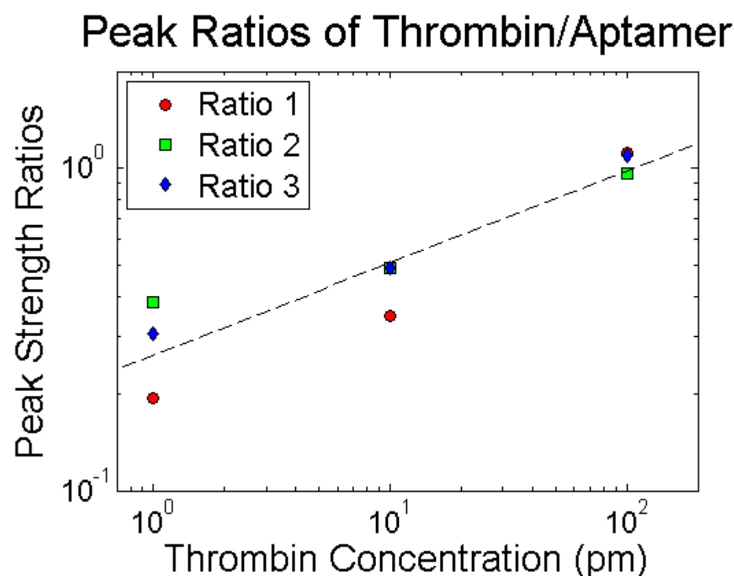

Figure 3.14 Relative peak strength between Raman modes of thrombin and TBA aptamers.

It was already mentioned that due to the enormous enhancement SERS can provide over regular Raman scattering, the measurement time can be greatly reduced in addition to keeping the laser power low. In this work, usually 1 or 2 seconds would be sufficient to finish one scan. Such an improvement in measurement time would make it possible to probe the molecular dynamics, which is something totally unavailable in normal Raman when each scan may take minutes. As an example, the binding dynamics of thrombin onto TBA aptamers was investigated. After repeated dilution, 500 fM of thrombin was injected into the microfluidic chamber at focus, and the Raman spectrum was acquired at 15 s, 30 s, 60 s, 90 s, and 120 s after the injection of thrombin. The results are plotted in Fig. 3.15. Comparing the curves before injection and at t = 15 s, clear difference can be observed already, indicating the ongoing binding within such a short time. This signal would simply be buried in the minutes-long acquisition process of regular Raman. Initially before the injection, peaks could be observed around 1463 cm^{-1}, which corresponds to the stretching modes of N1-C2 and N1-C6 in guanine [141], and around 1561 cm^{-1}, which is the guanine C2=N3 mode [138]. Within 15 s after the addition of thrombin, these peaks red-shifted to ~1427 and ~1526 cm^{-1}, respectively, indicating the binding between thrombin and the TBA aptamer through hydrogen bonds.

These additional bonding, along with the presence of thrombin as a large molecule, may have caused some slight conformation change of the TBA aptamer, which goes into the chair formation through the Hoogsteen-type interaction between guanines [138]. The conformational change was likely to be slight compression that brought the guanine components closer, resulting in stronger interaction of internal hydrogen bonds. Referring to Scheme 1 in [138], since the bonds of N1-C2, N1-C6, and C2=N3 are close to these hydrogen bonds, the increased force of internal hydrogen bonds probably dampened the restorative force of these vibrational modes and caused the red shift in the Raman spectra. It is also evident that 500 fM of thrombin could be easily resolved by the Au nano-bulbs, which again corroborates the extremely high enhancement factor these chips can provide. As the time went on, the spectral shape kept evolving until t = 90 s. The spectra of t = 90 s and t = 120 s were quite similar already, probably indicating the binding equilibrium already. The additional peak at ~1143 cm^{-1}, which corresponds to the C-N stretching of thrombin [119], further indicated the presence of thrombin binding.

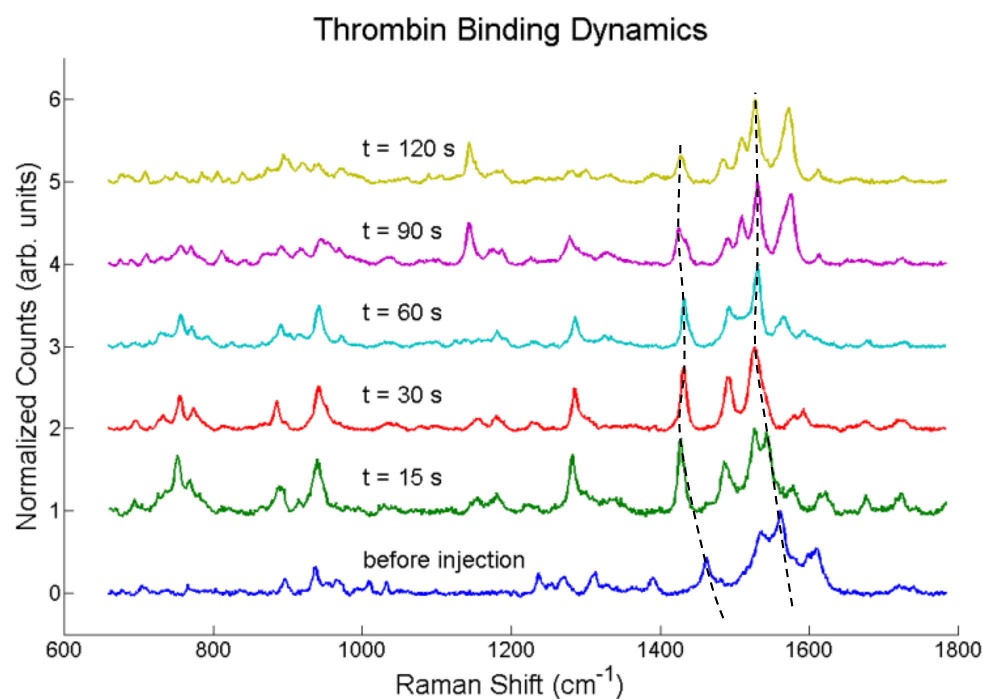

Figure 3.15 Time evolution of the Raman spectra from the binding dynamics of 500 fM thrombin onto TBA aptamers.

To estimate the number of molecules in the laser focal spot at such a low concentration, a few assumptions are made to get an upper bound of this number. Assuming no molecule was freely floating in the microfluidic chamber or adsorbed on any sidewall, when all thrombin molecules from the 500 fM injection are bound on the chip surface, the corresponding surface density would be ~9.96 x 10^{-17} mol/cm^2, or 6.00 x 10^7 molecules/cm^2 after considering all the physical dimensions of the chip and the chamber. On the other hand, the surface density of thiolated aptamers on Au is at least 10^{-11} mol/cm^2 [142], so it is not the limiting factor here. For the laser spot diameter of 1.5 μm, as a result, even in the scenario of 100% binding of thrombin onto aptamers there would be only ~1.06 molecules in the focal region, not to mention the maximal binding efficiency was at most only ~12% for 15-nucleotide aptamers similar to those used in this experiment [142]. As a result, statistically single-molecule response was resolved by the SERS nanostructures. This is probably also the reason that while the SERS response from thiophenol had been quite uniform among the entire region of nano-patterns, in the measurement of 500 fM thrombin some search had to be done to look for spots that would return some signal: while there were Au nano-bulbs everywhere in the region, thrombin was not found everywhere, not to mention the molecule has to be in the vicinity of the hot spots on Au nano-bulbs in order to be seen (see Fig. 3.10). Direct proof of single-molecule observation, however, would require a different experimental setup like fluorescence for immobilized molecules as in this scenario [143].

3.5.3 Temperature Response

The melting temperature of TBA aptamers in the presence of potassium ions is 53 ºC, which rises to 70 ºC when thrombin is also around at the same molar ratio [144]. Figure 3.16 shows the possible conformations of TBA aptamers; they can transition from unraveled ssDNA structures to the quadruplex "chair formation," and then get attached to thrombin [138].

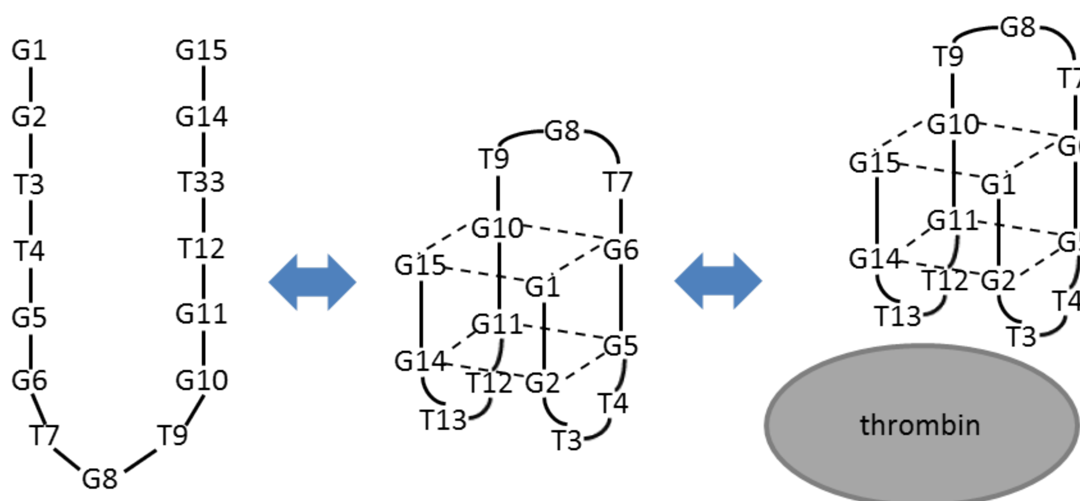

Figure 3.16 Schematics of different conformations of TBA aptamers, when they are unraveled, folded in quadruplex, or attached to thrombin.

To investigate the dynamics from the temperature change, a thermoelectric heater (Minco HM6807R3) was attached to the backside of the glass slide on which the microfluidic chamber was home-built. A thermocouple gauge (Omega STC-KK-K-20-36) was attached to the front side to read out the actual temperature. Raman spectra were then recorded a few minutes after the thermoelectric heater was adjusted to a new setting, when thermal equilibrium across the glass slide would be established already. Figure 3.17 (A) shows the Raman spectra from 1 pm of thrombin at various temperatures when the entire glass slide was heating up. Initially before the temperature went up, there were local peaks at ~1147, ~1535, and ~1631 cm^{-1}, which correspond to the C-N stretching, amide II and amide I modes of thrombin [117-119], respectively. This intensity of these peaks gradually diminished as the sample was heated up since thrombin was no longer so well bound on to the aptamers. Comparison between the curves indicates that thrombin was released at a temperature higher than 50 ^{o}C, since the curves can be divided into two group of above and below 51 ^{o}C in terms of their spectral shape. The original peak at ~1429 cm^{-1}, which was related to the red-shifted N1-C2 and N1-C6 modes of guanine as discussed earlier, also disappeared from this temperature on. Eventually, a local peak at 1461 cm^{-1} appeared, which is the un-shifted vibrational mode of N1-C2 and N1-C6 in guanine when there was no longer steric hinderance. Above 90 ^{o}C the

buffer in the microfluidic chamber was actually boiling already, and bubbling could be observed under the optical microscope. The chamber was then allowed to cool down by dialing back the power level of the thermoelectric heater, and the associated Raman spectra are shown in Fig. 3.17 (B). It can be observed that thrombin did not readily attach to the aptamers during the cooling process, and a distinct spectral change can be observed when the

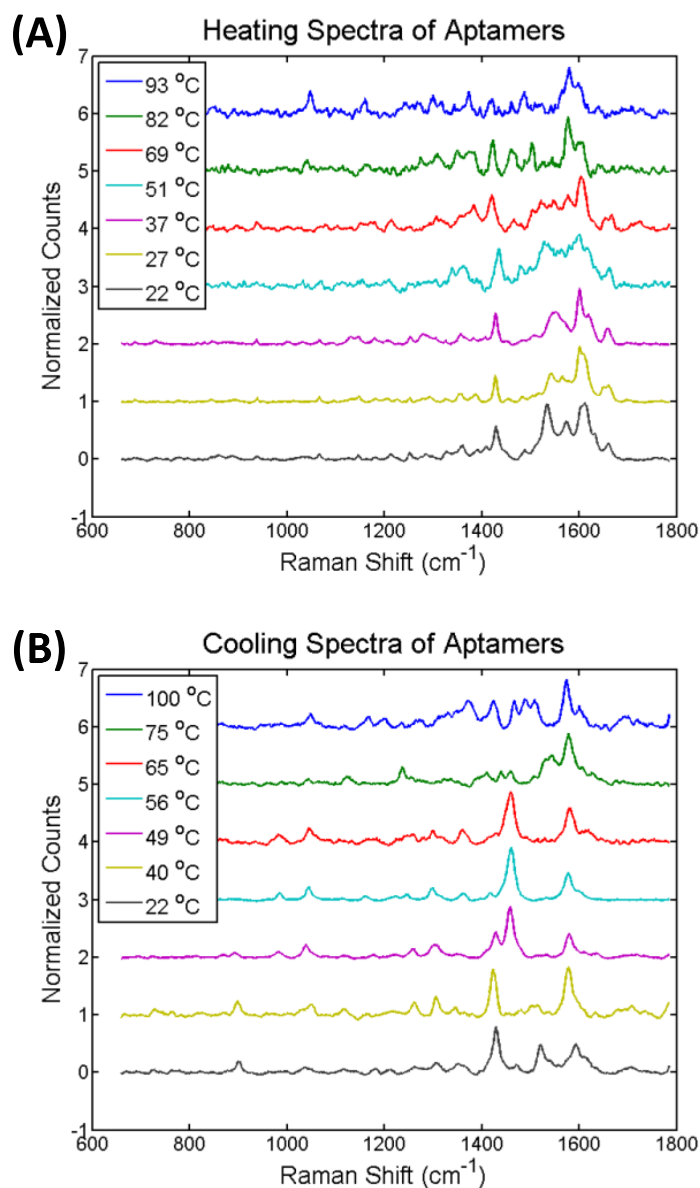

Figure 3.17 Raman spectra of thrombin and TBA aptamers when the solution was (A) heating up and (B) cooling down.

temperature dropped from 75 ºC to 65 ºC. The un-shifted N1-C2 and N1-C6 guanine mode, initially at ~1459 cm^{-1} when the temperature was high, eventually red-shifted again to ~1430 cm^{-1} at T = 22 ºC; this red-shift peak could be observed when the temperature dropped below 49 ºC. This indicates that the TBA aptamers started to fold into the quadruplex structures from unraveled strands, and this temperature range agrees well with the literature [144].

3.6 Hydrogen Sulfide and Ethyl Mercaptin

Since many sulfur-based compounds are hazardous to human health, the strong affinity between sulfur and gold opens up a good opportunity for the SERS Au nano-bulbs to detect trace amounts of these harmful substances. Among these molecules, hydrogen sulfide (H_2S) is of particular interest since it is detrimental in a very wide range of concentrations for different results. It can be generated by bacteria through anaerobic digestion, and hence the strong smells in sewers or swamps. It is denser than air, and therefore would accumulate at the bottom of poorly ventilated regions like basements or mine tunnels. The olfactory threshold of the human nose for H_2S is at least 130 parts per billion (ppb), and the threshold value as low as 0.5 ppb has been reported [145]. Above this threshold level, H_2S gives the characteristic foul odor of rotten eggs. In the work environment with potential H_2S exposure, the alarm is typically set to 5 or 10 parts per million (ppm) at least, with 15 ppm as the high alarm; nausea, coughing, eye irritation, a sore throat, shortness of breath, and other symptoms can already occur around this concentration. Eye damage starts to happen around 20 – 150 ppm [146], and at 100 – 150 ppm the sense of smell can be deadened so that the victim would fail to know the upcoming danger. A concentration above 300 – 350 ppm would overwhelm the oxidative enzymes in the human body designed to process the trace amounts of H_2S for metabolic functions, and the gas becomes poisonous from this point on by affecting the nervous systems or by preventing cellular respiration through bonding with iron in mitochondrial cytochrome enzymes. From this concentration to 530 ppm, pulmonary edema and possible death would occur. The central nervous system would be over-stimulated when exposed for 30 minutes to 500 pm H_2S, and breath regulation begins to fail if the concentration goes higher to 800 – 1000 ppm [146]. A concentration greater than 1000 ppm can lead to immediate loss of consciousness and breath, damage to the brain, or even death in just one single inhalation. More reviews on the toxicity of hydrogen sulfide can be found in

[147]. Beyond physiological hazards, hydrogen sulfide is also corrosive for various types of metals including copper, steel, etc. [147, 148]. It is flammable in the concentration range of ~4 – 46%, and can be explosive at an even higher concentration. When exposed to alcohol, it forms thiols compounds and is one reason that the taste of wine goes bad.

A convenient and sensitive detector for hydrogen sulfide is thus very desirable to provide early warning before its concentration gets too high. Commercial portable detectors, however, typically have a detection floor of only 0.1 ppm. In the past, detection of trace amounts of H_2S was achieve by fluorescence [149], gas chromatography [150], and so on. These methods, however, are not suitable for in-field applications. SERS detection can provide an alternative since Raman-scopes have been miniaturized for portable use, which will be discussed more in Section 4.3. A bottle of 2.16 ppm hydrogen sulfide was ordered from Praxair; the balance of the gas was chosen to be nitrogen, since H_2S is known to decompose slowly in the presence of oxygen [151]. While waiting for the approval and arrival of the purchase, proof-of-concept tests were done with ethyl mercaptan, a similar compound also with an –SH group, since it behaves analogously to hydrogen sulfide.

Ethyl mercaptan (CH_3CH_2SH), also known as ethanethiol, has a strong odor and as a result is commonly added to liquefied petroleum gas at a very small concentration as a caution in case of gas leaks. Similar to hydrogen sulfide, it is also found naturally in crude oil. For industrial production, ethanethiol can actually be derived from the reaction between ethanol and hydrogen sulfide [152]. In this experiment, a propane bottle for a portable stove, which contained 17 ppm of ethyl mercaptan, was used as the source. The SERS chips were brought to a few centimeters away from the bottle outlet, and exposed to the propane flow for ~20 seconds. Since the propane flow was not collimated and guided in any manner onto the chip, the effective concentration was likely to drop below the ppm level already when reaching the chip. Even at such a low concentration, the Au nano-bulbs were still able to resolve the Raman spectra from the interaction, as shown in Fig. 3.18. Right after the exposure, the ethanethiol molecules were mainly adsorbed onto the Au surfaces, and the spectrum consisted of a strong peak at 2650 cm^{-1} [94] corresponding to the –SH vibrational mode and a central portion around 1250 – 1750 cm^{-1} related to the ethyl group [153]. In 30 seconds the

ethanethiol molecules began to re-orient themselves onto the Au surface, and Raman peaks around 523 cm^{-1} and lower frequencies, attributed to vibrational modes associated with the Au-S bonding [97, 98], began to appear. The –SH mode, on the other hand, was diminishing since the hydrogen atoms were donated during the formation of Au-S bonds [95, 98]. At the one minute mark, the re-orientation was roughly complete and the Au-S Raman peaks thus dominated; the –SH mode disappeared as a result [154]. A peak at 945 cm^{-1}, corresponding to the ethane C-C stretching mode [155], could also be observed now. Again, the fast acquisition time enabled by the gigantic SERS enhancement factor made it possible to resolve the binding dynamics. As will be described in Chapter 5, the next step is to push for the detection limit by further diluting the 2.16 ppm standard of H_2S that was ordered. The wafer-scalable nature of the Au nano-bulb fabrication can make the chips cost-effective and disposable; if the chips have to be reused, oxygen plasma can effectively strip H_2S from the chip surface.

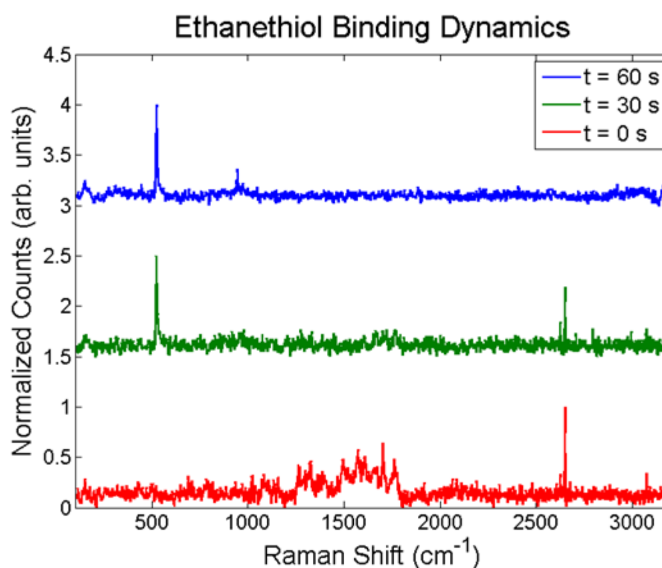

Figure 3.18 Time evolution of Raman spectra of ethyl mercaptan on Au nano-bulbs.

Chapter 4

Integration into Systems

So far the concepts of EOT and SERS have been well proved on the chip level. For applications outside of a laboratory, especially for in-field applications, the dependence on lab infrastructures and the degree of sophisticated alignment have to be minimized. Otherwise, the benefit of wafer-scalable fabrication would only lead to cheap consumables in the laboratory, calling for well-trained operators instead of reaching a broader spectrum of users.

In this chapter, it is demonstrated how further fabrication and assembly can push these devices into the levels of sub-systems or systems so that the overall operation can be more user-friendly. First, it is shown how the microfluidic structures can be built-in on the chip for easier sample preparation and chip usage. Furthermore, the final substrate does not have to be silicon anymore, but can be a flexible substrate for better conforming abilities. In a same vein of nanofabrication, nanocups are now also available in a wafer-scalable way and with much greater design flexibility than possible in the past. Finally, the entire system can be made fiber-based, and free-space optical alignment can be totally eliminated. In addition to tabletop configurations, it is also possible for the whole system to be portable and mobile. These modifications would open the door for various applications, including clinical investigation and oil drilling.

4.1 Variations for Integrated Microfluidics or Implantation Applications

The home-built microfluidic chamber, as shown in Fig. 3.13 (A), while doing the job, is not the best option for easy and straightforward measurement, especially for in-field applications. More integrated fabrication is thus desirable. Previously, polydimethylsiloxane (PDMS) has been a very popular choice for the fabrication of microfluidics on a chip [156]. For the SERS applications, however, the traditional approach of bonding fabricated PDMS micro-channels onto a chip may result in some issues. First of all, PDMS is not entirely impermeable to gas or liquid; the permeability is small enough for regular microfluidic experiments, but since long hours of incubation may be necessary for the functionalization of SERS chips (see Section 3.5), the PDMS layer may be soaked with reagents as a result. Furthermore, if the bonding takes place first, the small passage of microfluidic channels may introduce additional difficulty

in the functionalization process; if the functionalization is done first, the bonding quality may degrade. In addition, if focusing optics such as a microscope objective is used in the measurement, the PDMS thickness has to be smaller than the working distance of optics, which would cause additional difficult in the handling and bonding for such a thin layer.

This issue can be properly addressed if the microfluidic channel is part of the Si structures from the beginning, as shown in the fabrication diagrams of Fig. 4.1. First, recessed regions are defined and etched on the silicon chip, as in Fig. 4.1 (A). Nanostructures are then defined and etched as usual in the recessed regions, as depicted in Fig. 4.1 (B). For typical microfluidics the channel height is from ten to tens of μm, which is still well within the capability range of the Leica EBPG 5000+ system since it allows the beam writing to proceed if the chip surface height is within ± 100 μm of the reference plane. The rest of the process flow is the same as in Fig. 3.2. After the whole structure is fabricated, the chamber can be

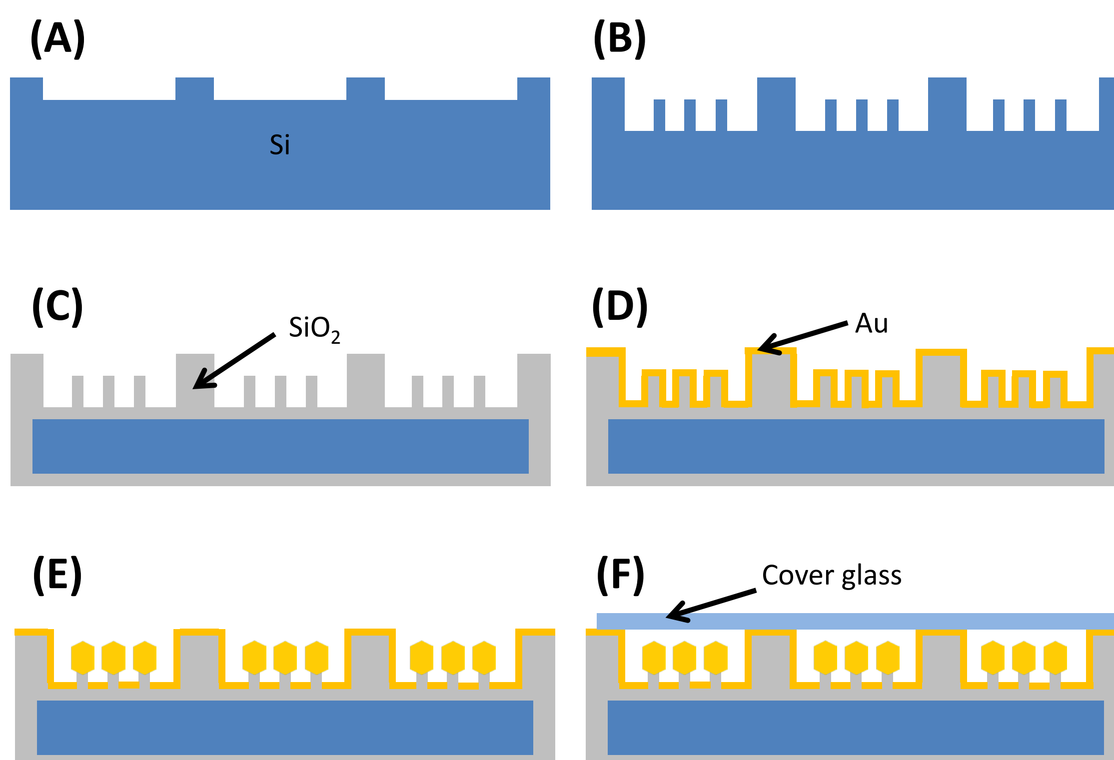

Figure 4.1 Fabrication sequence of SERS nanostructures in a recessed region on silicon.

easily sealed by placing a piece of cover glass on top, as illustrated in Fig. 4.1 (F). Such a configuration would be convenient for subsequent measurement, either with a microscope or with a portable Raman-meter.

While peuso Bosch is a great tool for nano-etching, its etch rate of ~250 nm/min is too slow for defining recessed regions that can go as deep as 50 μm. Regular SF_6 etching (plain SF_6 or chopping Bosch), while faster, would require a thick layer of mask for such an etch depth. For scenarios like this, the cryogenic etch with SF_6 and O_2 is a good option. The etch rate can reach a few microns per minute; the verticality of sidewalls can be controlled, and there is no scalloping as in chopping Bosch; finally, the required forward power (CCP) is small, so mask erosion is minimized. The cryogenic etch, like the pseudo Bosch, is a mixed mode etch that SF_6 and O_2 are simultaneously in the chamber. At a low temperature, typically at least -85 ^oC and sometimes even lower at -140 ^oC to fine-tune the etch [53], SiO_xF_y is no longer volatile and can act as a passivation layer [157]. This mixed-mode operation is then similar to the mechanism of pseudo Bosch mentioned in Section 2.1.3, where the passivation layer on the sidewall improves the aspect ratio and the plasma CCP mills open the layers directly facing the ions. Since SiO_xF_y is fragile, only a small forward power is needed to go through this passivation layer, so the etching process is more chemical than milling and the etch rate is much higher than in pseudo Bosch. Because of the small CCP power, moreover, only a thin layer of Al_2O_3 would be needed as the etch mask, which can save the deposition time. (For nanofabrication with the cryogenic etch, the thinner layer of Al_2O_3 also means better lift-off resolution.) Depending on the etch depth to be obtained, sometimes photoresist, usually a poor masking material in plasma chemistry, would be enough already in the cryogenic etch [53]. By changing the temperature, the oxygen flow or the plasma forward power, different levels of effective passivation can be achieved and the sidewall verticality can be well controlled. When properly tuned, the cryogenic process can easily etch pillars with an aspect ratio of 1 : 100 and a height of 10 μm [158]. If the oxygen flow is insufficient for the temperature, CCP power or the chamber condition, however, black silicon would start to occur [159], with Fig. 4.2 being an actual example from a particular etch. More details and reviews on the cryogenic etch can be found in [157, 159].

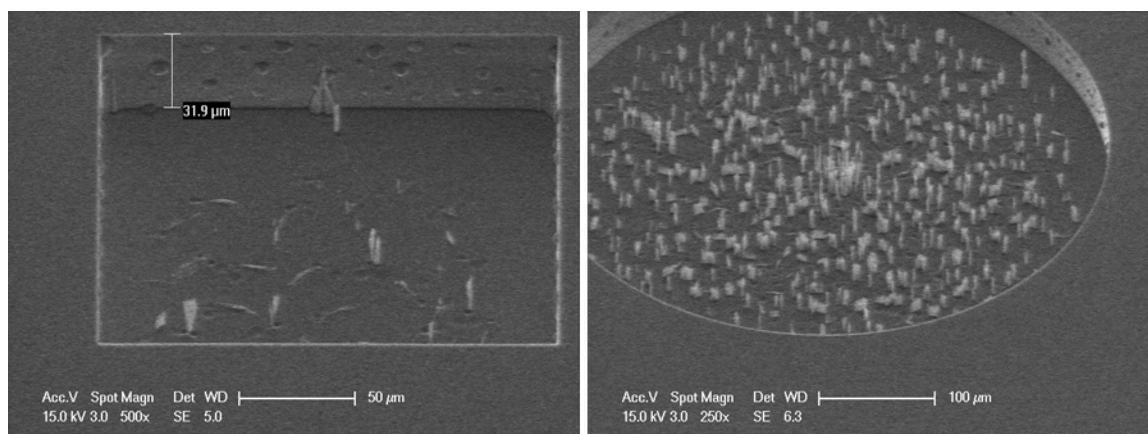

Figure 4.2 Black silicon was about to occur since the passivation level was not enough in the cryogenic etch.

The fabricated nanostructures are shown in Fig. 4.3; it can be seen that when the cryogenic etch was properly tuned, no black silicon would occur at the bottom of the channels. Around the top-right corner in Fig. 4.3 (A), a microfluidic conduit can be clearly seen. Since the SEM micrographs were taken at an angle of 45°, the actual channel depth would be ~47 and ~68 μm, respectively. In addition to microfluidics-based Raman measurement, such a structure is also ideal for implanting the chips *in vivo* for monitoring specific molecules in the body [160]. A few research groups have been working on the Raman readout of physiological signals *in vivo*, such as the glucose level [161]. Due to the weak nature of regular Raman scattering, the signal of interest is usually deeply buried in noise and complicated post-processing of spectra is

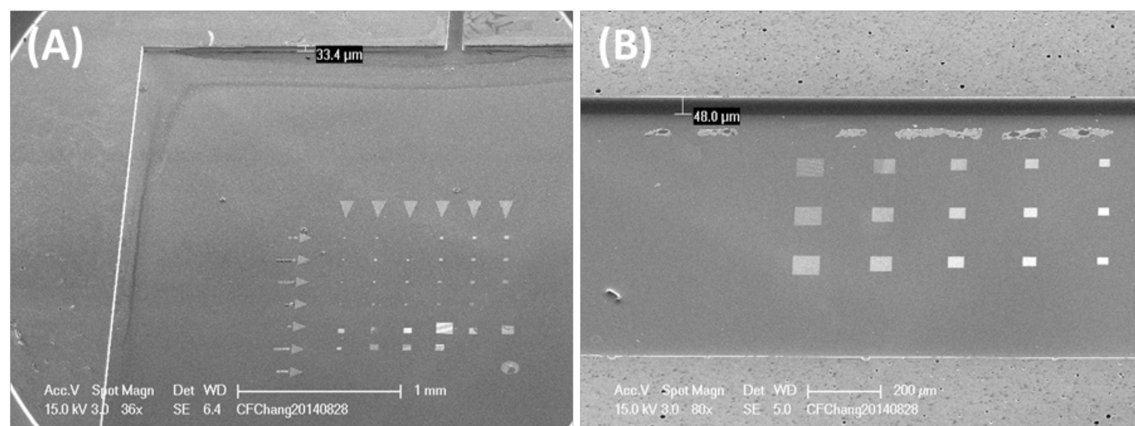

Figure 4.3 Fabricated nanostructures in recessed regions on silicon.

called for. If a SERS probe with these Au nano-bulbs can be implanted, there is a better chance of resolving the actual signal at a shorter time and less laser power. By fabricating the nanostructures inside a recessed region, they can be well protected from being knocked over during the implantation process.

Strictly speaking, electron-beam lithography is not a canonical option in commercial semiconductor foundries yet, but since it is only used to define the regions of nanopillars, the process would take a short time instead of being a process bottleneck. For large-scale production, the wafers can be outsourced to commercial companies specializing in e-beam lithography. If immersion photolithography has to be used, the nanostructures can be fabricated first as in Fig. 3.2, and appropriate materials can be deposited to define the micro-channels. If the material can handle the temperature of thermal oxidation, it can be added between the steps of Fig. 3.2 (B) and (C); if not, it can be deposited at the end. Since the deposition thickness is on the order of tens of μm, a good choice would be a foundry for microelectromechanical systems (MEMS).

4.2 Plasmonic Structures on Flexible Substrates

While silicon as a substrate enables the top-down fabrication, its rigidity may be an issue if the final device has to conform onto a curved surface, if immunity rejection has to be minimized for implantation applications, and so on. For many sensing and implantation applications, it would be preferable if the substrate can be flexible. This can be done by transferring the fabricated nanostructures onto a flexible layer [162]. Starting with SERS nanostructures after thermal reflow as in Fig. 4.4 (A), a flexible layer is deposited on top as shown in Fig. 4.4 (B). In this work PDMS was used as an example, but the flexible layer can also be other kinds of polymers or plastics. The top flexible layer could then be peeled off from the substrate for the structures shown as the upper half of Fig. 4.4 (C); if suitable etching chemistry (ex: BHF and XeF_2) is chosen to remove the SiO_2 and Si regions while preserving Au and the flexible material, the whole structure can also end up as the lower half of Fig. 4.4 (C). The hollow interiors of the Au nano-bulbs, previously attached to the SiO_2 nanopillars, are now accessible as nanocups. In the past, the methods of fabricating nanocups included nano-indentation [163], lift-off with sacrificial layers [164], metal deposition onto nano-beads

[165], substrate treatment for self-organized structures [166], and so on. None of these methods has the all advantages of the top-down process described in this work, including designer's freedom, availability of high aspect ratios, etc. Furthermore, 3D sculpting enabled by pseudo Bosch allows the fabrication of various nanocups with different interior cavity shapes – even on the same chip – like oval, rectangular, and so on. In comparison, only nanocups of highly symmetric shapes were available in the literature [163-166]. The process of thermal reflow furthermore allows an additional degree of freedom, since various level of annealing can be achieved as shown in Fig. 3.3. Moreover, the previous methods only allowed the metal layer to be either everywhere or nowhere between the nanocups, while here it can be

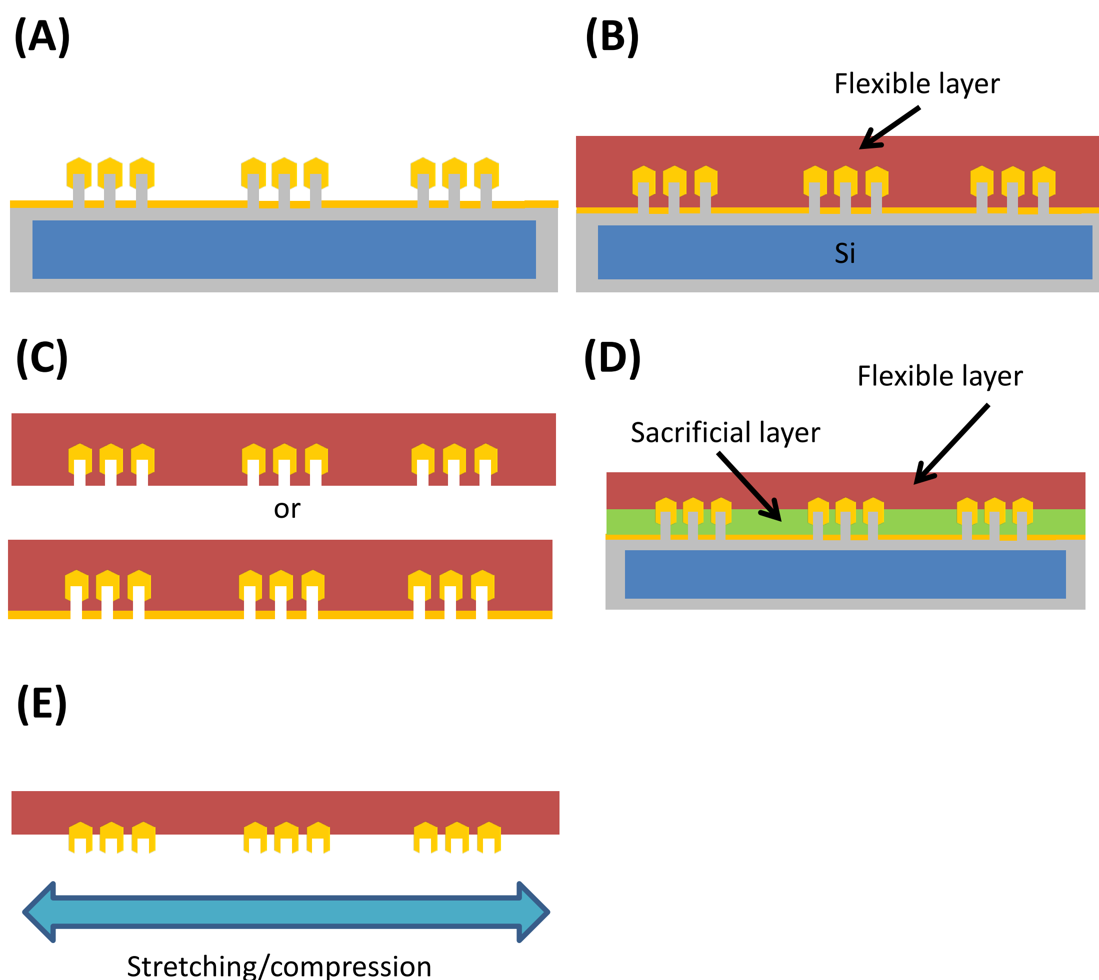

Figure 4.4 (A) – (C): Fabrication sequence of SERS nanostructures on a flexible substrate; the amount of embedding of Au nanocups in the substrate can be controlled as in (D) and the final device can be compressed or stretched as in (E).

optional as depicted in Fig. 4.4 (C). With a few additional steps, furthermore, it can be precisely controlled how deep the nanocups are embedded in the flexible layer. Starting from Fig. 4.4 (A) again, a sacrificial layer is deposited on top to be precisely etched later; for example, oxygen plasma ashing can thin down a photoresist layer with good precision. The flexible substrate is then coated on top, as illustrated in Fig. 4.4 (D). The separation of the flexible layer with embedded nanostructures could now proceed in the methods described earlier for the final device like Fig. 4.4 (E); for this configuration, the small gaps between Au nano-bulbs are now also accessible for SERS or other applications. Moreover, now that the substrate is flexible, it can be either compressed or stretched to modify the distance between nanocups.

Figure 4.5 shows the fabricated results in the configuration of Fig. 4.4 (E), so that the nanocups are closer to the PDMS surface for easier SEM imaging. The PDMS elastomers used here were Sylgard 184 from Dow Corning. Figures 4.5 (A) and (B) show the ability to design the shape of the interior cavity; here one was from a pillar, and the other a rectangular post. In Figs. 4.5 (C) and (D), it can be seen that the original tiny gaps between Au nano-bulbs are still available for molecular detection. If the interior cavity is intended to be made smaller than allowed by the lithography resolution, it can be done by partially oxidizing the nanostructures as in Fig. 4.6 (B), followed by the removal of the outer layer of SiO_2 as shown in Fig. 4.6 (C), such as by BHF. Since the process of thermal oxidation can be controlled with great precision – when necessary, the oxidation temperature can be even lowered for greater resolution – the thickness of the remaining Si parts can therefore be well defined. Another thermal oxidation then converts all the nanostructures into SiO_2, as shown in Fig. 4.6 (D), followed by the rest of the nanofabrication steps as described earlier. This method of partial oxidation can also be applied to make ultra-small EOT nano-apertures if necessary.

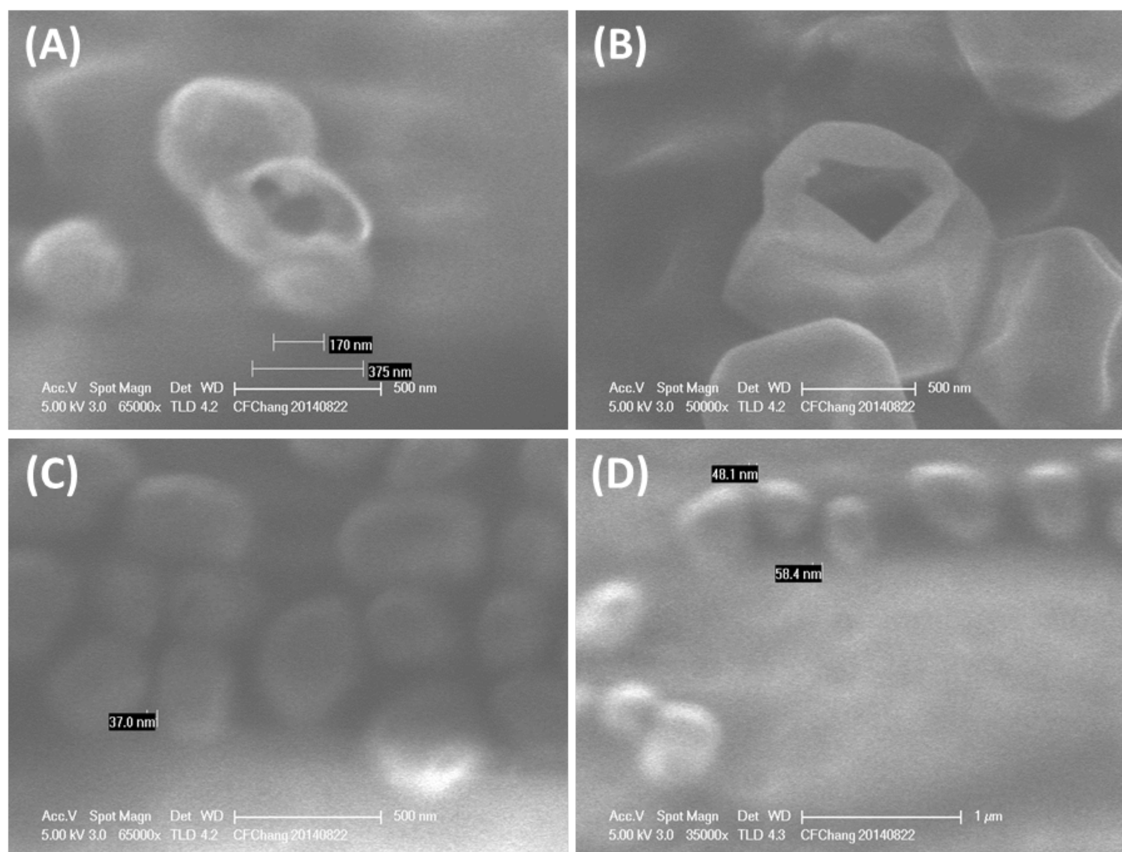

Figure 4.5 Various SEM micrographs of fabricated Au nano-cups.

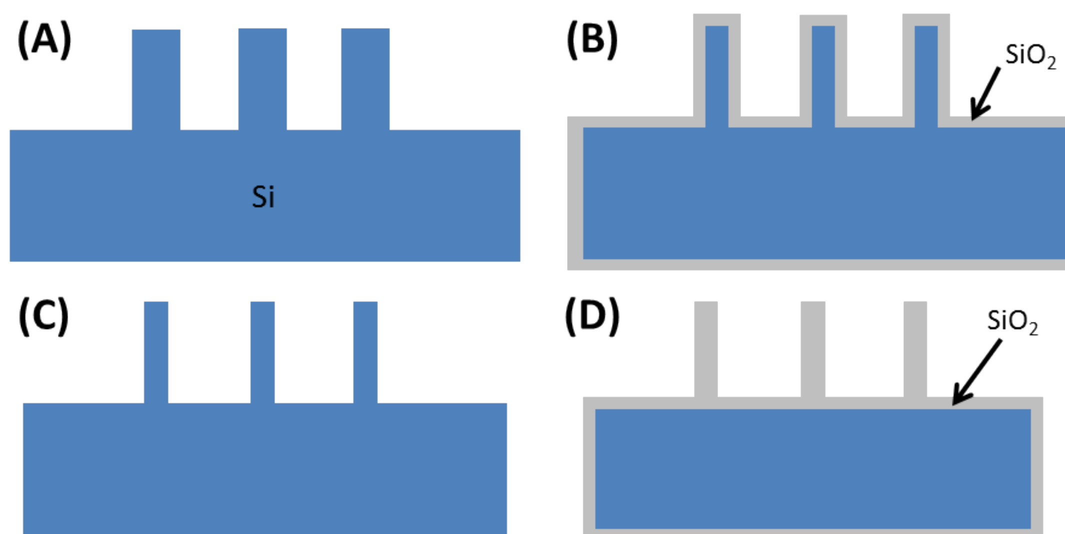

Figure 4.6 Fabrication steps to shrink the nanostructure size beyond the lithography resolution limit. After Si nanostructures are defined in (A), they are partially oxidized as in (B). After the removal of the outer SiO_2 layer as in (C), the structures can be oxidized again as in (D).

If desired, the nanostructures can also be transferred in an upright orientation [162], as illustrated in Fig. 4.7. In Fig. 4.7 (A), a sacrificial layer is first coated on top for a carrier chip to be attached, which would provide mechanical support for the subsequent chip processing. The Si region right below the nanostructures is then removed, as shown in Fig. 4.7 (B); for example, it can be done with the BHF etch first to remove the SiO_2 layer on the backside of the chip, followed by XeF_2 or SF_6 etch to remove Si. An optional adhesion layer can be deposited onto the newly exposed SiO_2 layer right below the nanostructures if it is needed for the flexible material, which is then applied or bonded onto the entire stack as in Fig. 4.7 (C). The sacrificial layer can now be released to get rid of the carrier chip for the final device like

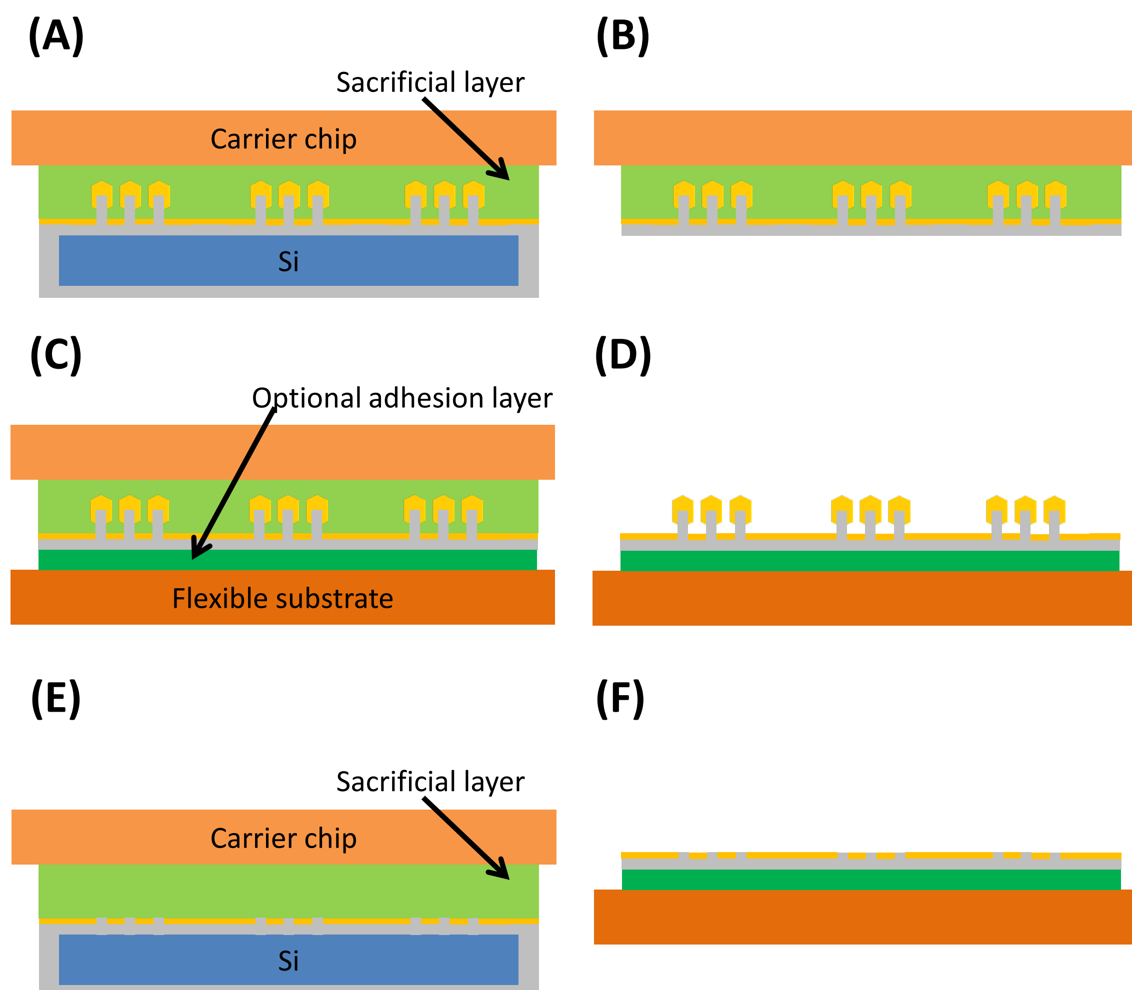

Figure 4.7 Fabrication sequence of SERS or EOT nanostructures on a flexible substrate in an upright orientation.

Fig. 4.7 (D). A similar process flow can also be applied to EOT nanostructures, which is depicted in Figs. 4.7 (E) and (F).

Figure 4.8 shows the transferred Au nano-bulbs in an upright position onto a PDMS substrate; the PDMS material was RTV 615 from Momentive Performance Materials Inc. (formerly GE Silicones). In Fig. 4.8 (A), it can be observed that the small gaps between nano-bulbs were still well preserved after the transfer. When zoomed out in the SEM, seen in Fig 4.8 (B), the integrity was seen to be maintained for the entire area with nano-patterns.

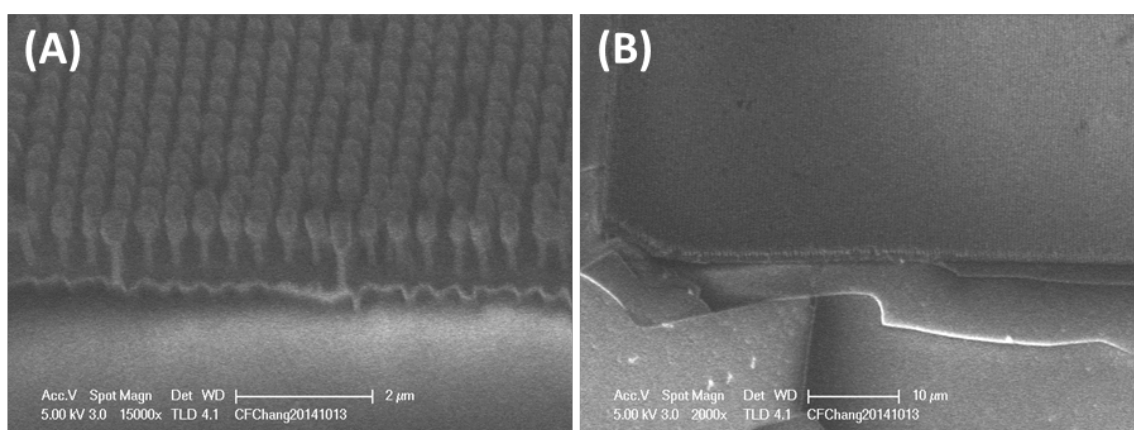

Figure 4.8 SEM micrographs of SERS Au nano-bulbs transferred onto PDMS in an upright position.

Again it is optional for the designer's choice to keep the bottom Au layer or not [162]. If the layer is to be removed, a patterning layer like photoresist is first deposited and defined around the region of nanostructures, as shown in Fig. 4.9 (A). The Au layer can then be etched away if the etchant does not attack the patterning layer, as in Fig. 4.9 (B). After the removal of the patterning layer, the entire structure as in Fig. 4.9 (C) can now go through similar fabrication steps to be transferred onto a flexible substrate. The final configuration would look like Fig. 4.9 (D); with the Au layer gone, the laser beam can now come from the other side as long as the flexible material is transparent. This etching technique is the most critical step in constructing a fiber-based SERS system, which will be discussed in more details in the next section.

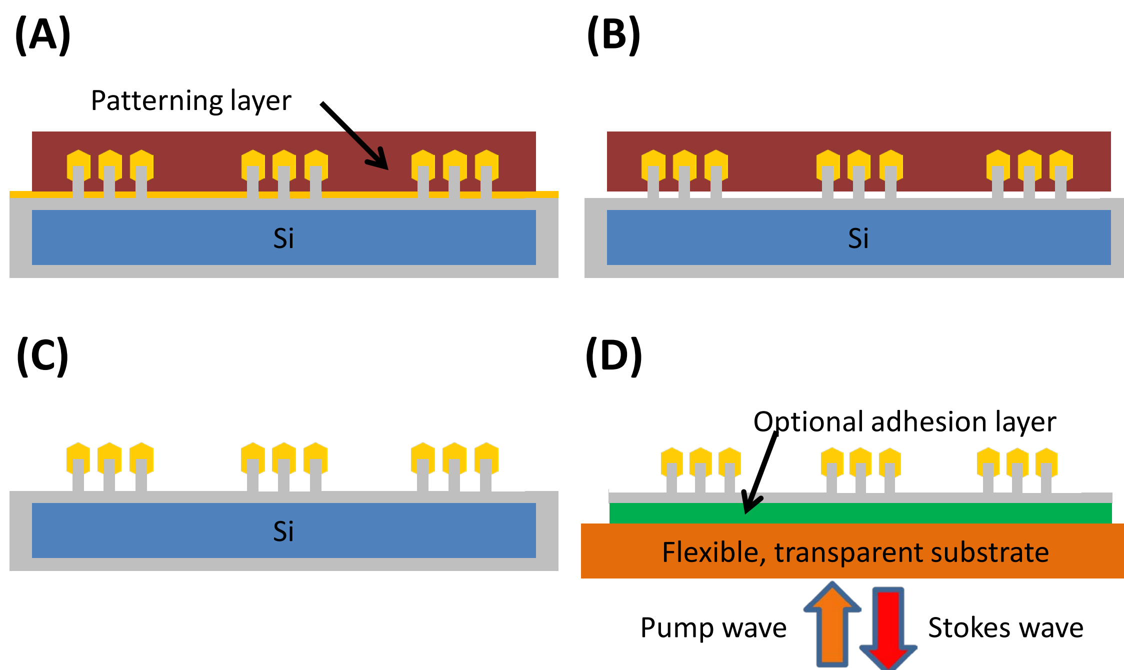

Figure 4.9 Fabrication sequence of SERS Au nano-bulbs on a flexible substrate with the bottom Au layer removed.

Figure 4.10 shows the fabricated results of Au nano-bulbs with the bottom Au layer removed. The bottle of TFA gold etchant from Transene lists an etch rate of 28 Å/s, although the actual etch rate seemed to be faster than this number. In Figs. 4.10 (A) and (B), it can be clearly seen that only the Au nano-bulbs at the top of the nanopillars remained, while the rest was etched away already. Figs. 4.10 (C) and (D) further illustrate the insensitivity of this method to fabrication defects, such as regions of missing nanopillars. One added benefit of this approach is the elimination of Au nano-bulbs that are not entirely separated from the bottom Au layer in the thermal reflow process; this can also be seen in Figs. 4.10 (C) and (D), where bare SiO_2 nanopillars without any gold can be observed. Since the Au separation was incomplete on those pillars, the gold etchant would then remove the partial Au nano-bulbs on them as well.

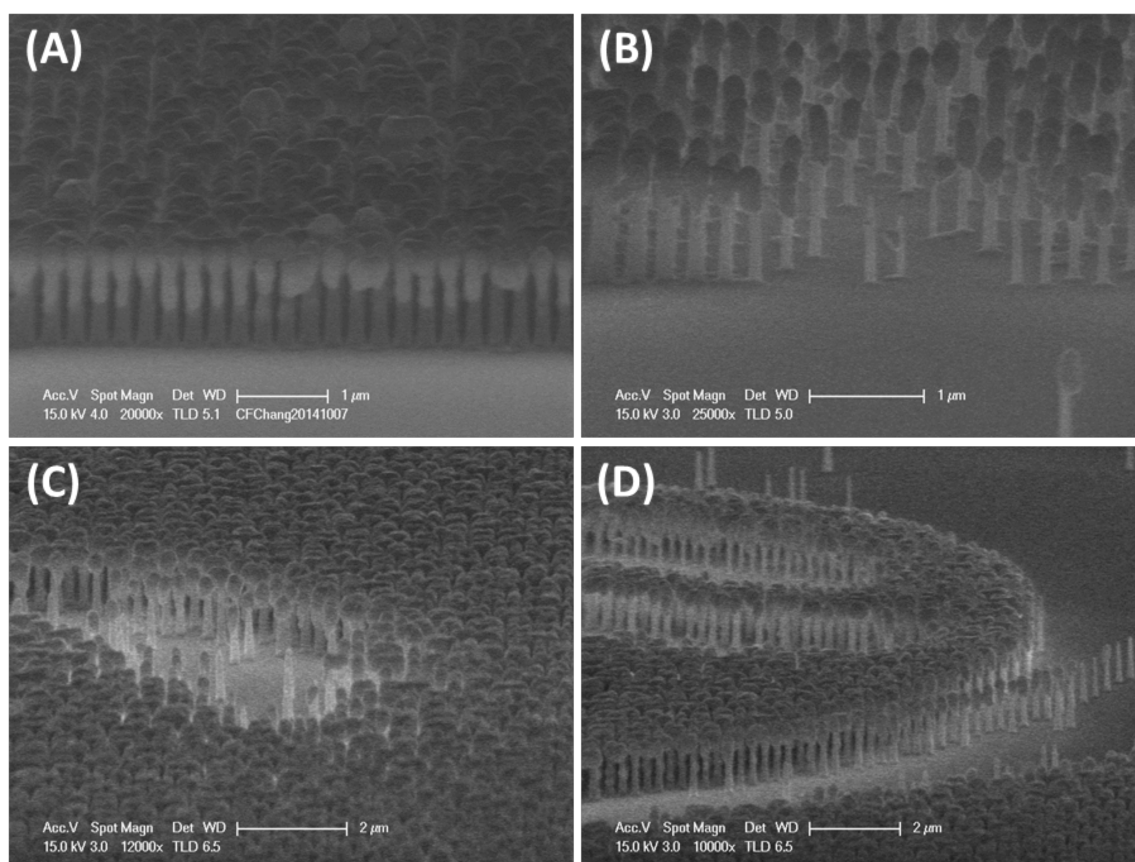

Figure 4.10 SEM micrographs of Au nano-bulbs with the bottom Au layer removed.

4.3 All-Fiber Sensors and Systems

With further improvement such as integrated microfluidics or flexible substrates, the devices are now easier to use outside of a laboratory setting. However, they still need a certain amount of optical alignment, which may be time-consuming. A fiber-based system is thus very desirable, since the alignment can be done once and for all, and the operation does not need dedicated microscope support. Without re-alignment every time of use, the measurement would also be more consistent and easier for comparison.

Starting from the structure as shown in Fig. 4.9 (C), where the bottom Au layer has been removed, the Si region right below the nanostructures is then etched away in similar ways as described in Section 2.1.7. To accommodate the wide spectral range associated with the

Raman Stokes waves, 50/125 μm multimode fibers (FG050LGA from Thorlabs) were chosen for the work; with a low –OH concentration, the attenuation of the silica core stays low for the range of 400 – 2400 nm. The jacket of the fiber was first stripped, and a thin layer of photopolymer, Norland Optical Adhesive 63 from Norland Products Inc., was applied to the fiber tip. After the tip was brought into contact with the backside of the Au nano-bulb membrane, as illustrated in Fig. 4.11 (A), the photopolymer could then be cured with UV light in a few minutes. After being fully cured, the adhesion layer becomes transparent in the range of 320 – 3000 nm, which is more than enough for the SERS applications. The pump wave can now be delivered from the other end of the fiber, which also acts as the waveguide for the back-reflected Stokes wave, as shown in Fig. 4.11 (B).

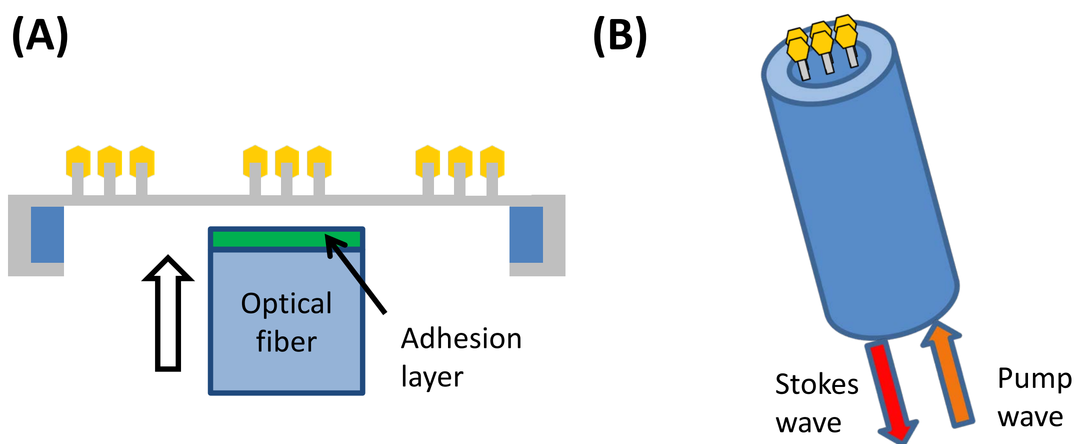

Figure 4.11 Schematic diagrams of (A) the transfer of Au nano-bulbs onto a fiber tip and (B) the working principle of a SERS fiber.

Figures 4.12 (A) and (B) show the optical micrographs of a fiber chip before and after the removal of the bottom Au layer, respectively. Small areas of missing pillars were due to fabrication defects. The microscope camera, Sentech STC-TC83USB-AS, would adjust the gain and contrast automatically, and therefore it can be seen that the optical contrast between the region of nano-patterns and the general background was different between these two figures, which indicated the presence and absence of the bottom Au layer. Figure 4.12 (C) is the SEM micrograph of Fig. 4.12 (B); again the contrast could be seen between the background, Au nano-bulbs on nanopillars, and bare pillars due to incomplete thermal reflow.

Figure 4.12 (D) shows the optical micrograph after the Si region below the Au nano-bulbs had been etched away with XeF_2; the chip was ready for bonding at this moment.

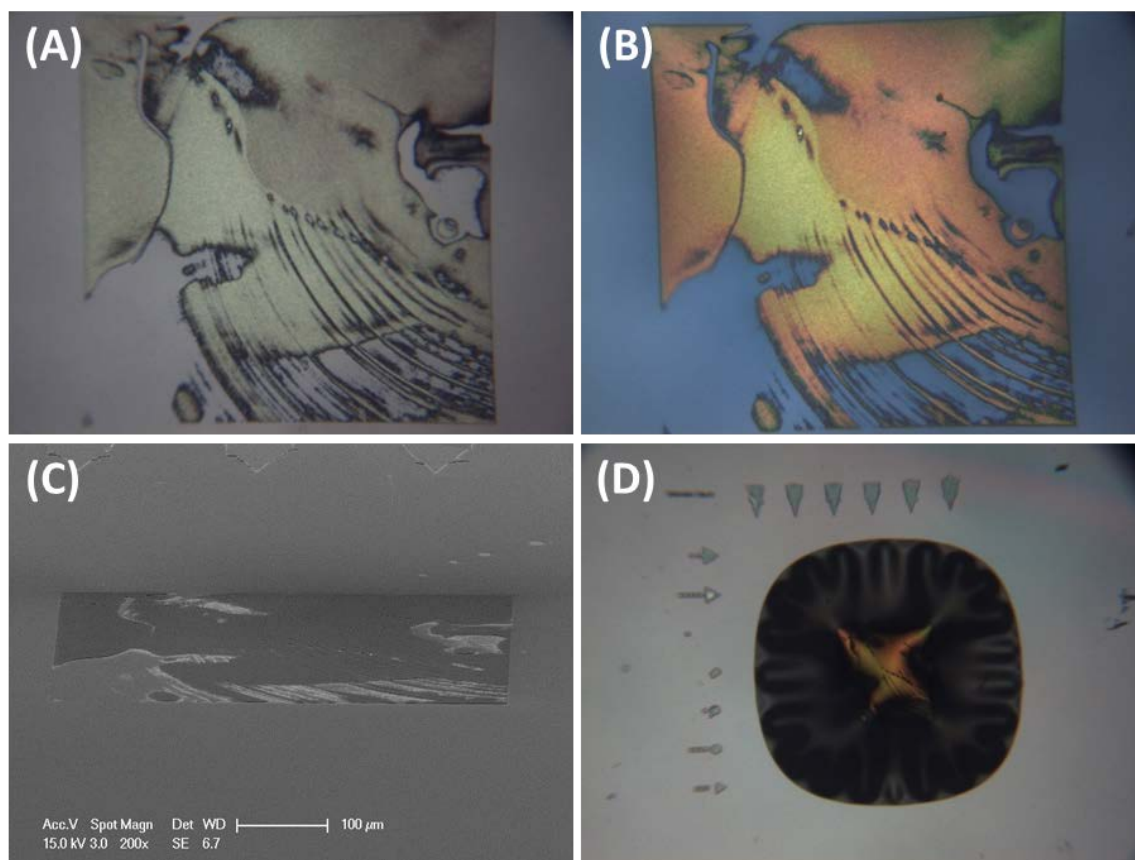

Figure 4.12 Optical micrograph of a fiber chip (A) before and (B) after the removal of the bottom Au layer. (C) shows the associated SEM micrograph after the Au layer was removed. (D) is an optical micrograph after the Si region below the patterns was already etched.

Figure 4.13 (A) shows the SEM micrograph of SERS nanostructures bonded onto the tip of a 50/125 μm multimode fiber. The zoomed-in SEM image at the edge of the nano-patterns is shown in Fig. 4.13 (B); again it can be seen that the bottom Au layer had been removed, and the nanopillars were not knocked over during the transfer process. Figure 4.13 (C) shows the central region of the nano-patterns on the fiber tip; the tiny gaps between Au nano-bulbs were indeed well preserved, thus proving that this method can transfer the patterns with fidelity and integrity. Figure 4.13 (D) was taken at an angle of 80° in order to show the

lateral dimensions. The adhesion photopolymer was not exactly flush along the sidewalls of the optical fiber, and the total diameter increased to almost 150 μm eventually. Even at this diameter, the entire fiber can still fit into a gauge 30 needle (inner diameter 159 μm) for applications like intravenous sampling; the needle provides the sharp tip for drilling and the mechanical protection for the Au nano-bulbs, and once the needle is in place in the body, the fiber can be pushed forward so that it goes beyond the needle tip if necessary.

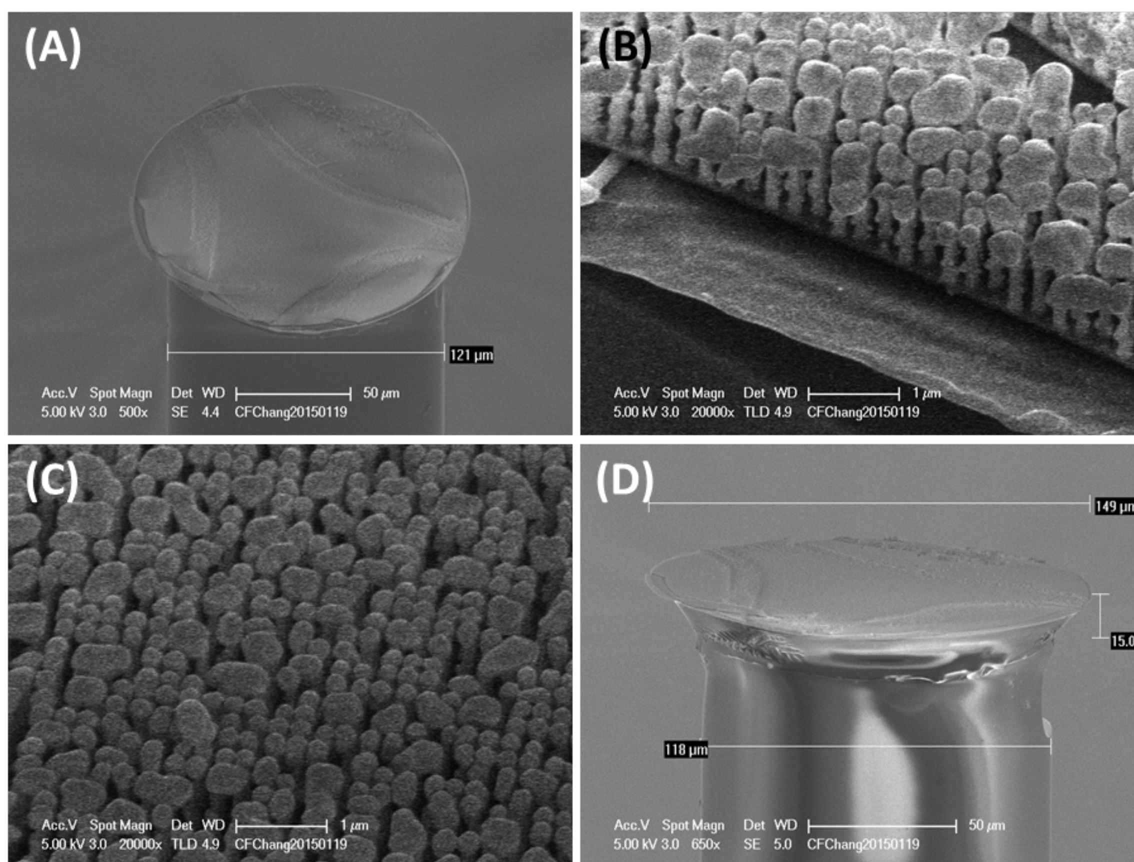

Figure 4.13 (A) SEM micrograph of a fabricated SERS fiber showing the nanostructures on the tip; (B) and (C) show the zoomed-in images at the edge and at the center of the nano-patterns, respectively. (D) shows the lateral dimensions when imaged from the side.

The corresponding optical micrographs can be seen in Fig. 4.14 (photo credit: Keith M. Russell). Figure 4.14 (A) shows the photo from looking into the fiber end; due to the limited availability of nanopillar regions from this chip, there was a small portion of the fiber core that

was not covered by the Au nano-bulbs, but the percentage was small and the fiber is anticipated to be a working device. Figure 4.14 (B) shows the optical micrograph from the side; with further improvement of the bonding recipe, the total diameter can be expected to be even smaller. The cladding region can also be reduced, either mechanically or chemically, if a thinner SERS-fiber is desirable.

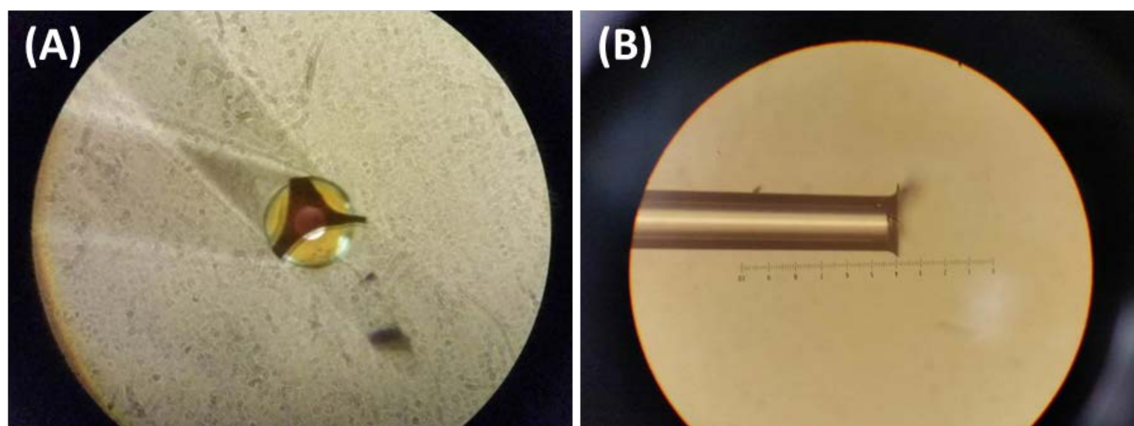

Figure 4.14 Optical micrographs of the SERS fiber (A) from the end and (B) from the side.

From Fig. 4.13 (D) it can be seen that the thickness of the adhesion layer was about 15 μm. The thickness can be made even smaller with further fine-tuning of the boding process, but the device characteristics should not be affected already even at a thickness of 15 μm. Here are some numerical estimates: since the numerical aperture (NA) value of the fiber is 0.22, suppose the exiting laser beam also diverges at this angle (worst case) due to tight coupling from the other end; the beam diameter would then expand from 50 to ~56.8 μm after traveling for 15 μm, so the optical energy would still concentrate around the nano-bulb areas. On the other hand, suppose the laser light emitting from the fiber tip is approximated as a Gaussian beam, then at a wavelength of 633 nm and a beam waist of 50 μm, the Rayleigh length $z_R = \pi {w_0}^2/\lambda$ would be 1.24 cm, where w_0 is the beam waist diameter. This value is already much longer than the thickness of the adhesive, and it can therefore be expected that the Au nano-bulbs at the fiber tip would be well illuminated by the laser source. The adhesion layer, on the other hand, has a nominal refractive index of 1.56. The refractive index of the

fiber core is Thorlabs proprietary information and thus unavailable, but as an estimation it can be treated as regular SiO_2. Now that the entire stack consists of an adhesive sandwiched between silica layers, the addition of the adhesion layer would introduce the following Fabry-Perot effect to the overall spectral transmission [9]:

$$T = \frac{(1-R)^2}{(1-R)^2 + 4R\sin^2\left(\frac{2\pi n d}{\lambda}\right)},$$

where n = 1.56 is the refractive index of the epoxy, d = 15 μm is the epoxy thickness, and R is the reflectivity between SiO_2 and the adhesion layer: $R = (n - n_{glass})^2/(n + n_{glass})^2$. The refractive index of SiO_2 was calculated with the associated Sellmeier equation of [167],

$${n_{glass}}^2 = 1 + \frac{0.6961663\lambda^2}{\lambda^2 - 0.0684043^2} + \frac{0.4079426\lambda^2}{\lambda^2 - 0.1162414^2} + \frac{0.8974794\lambda^2}{\lambda^2 - 9.896161^2},$$

where λ is in μm here. The anticipated Fabry-Perot effect is plotted in Fig. 4.15, which corresponds to the wavelength range of 650 – 950 nm. Since SiO_2 and the epoxy have very similar refractive indices, the Fabry-Perot modulation from the adhesion layer can basically be ignored here.

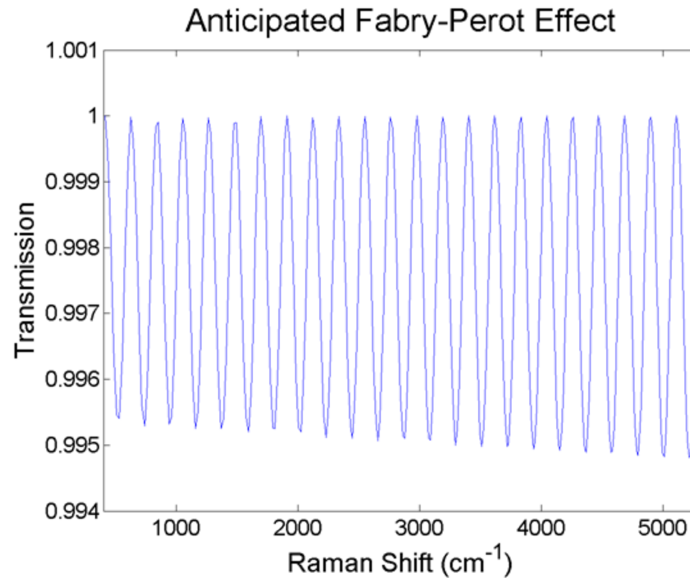

Figure 4.15 Anticipated Fabry-Perot effect due to the adhesion layer at the fiber tip; excitation: 633 nm.

To demonstrate that the entire device can fit into a hypodermic needle, Fig. 4.16 shows the SEM micrographs of a SERS fiber in a needle at different magnifications. A gauge 26 needle (inner diameter 260 μm) was used here for the convenience of inserting the fiber into the needle from the tip in order to protect the Au nano-bulbs, but if a fiber segment is threaded

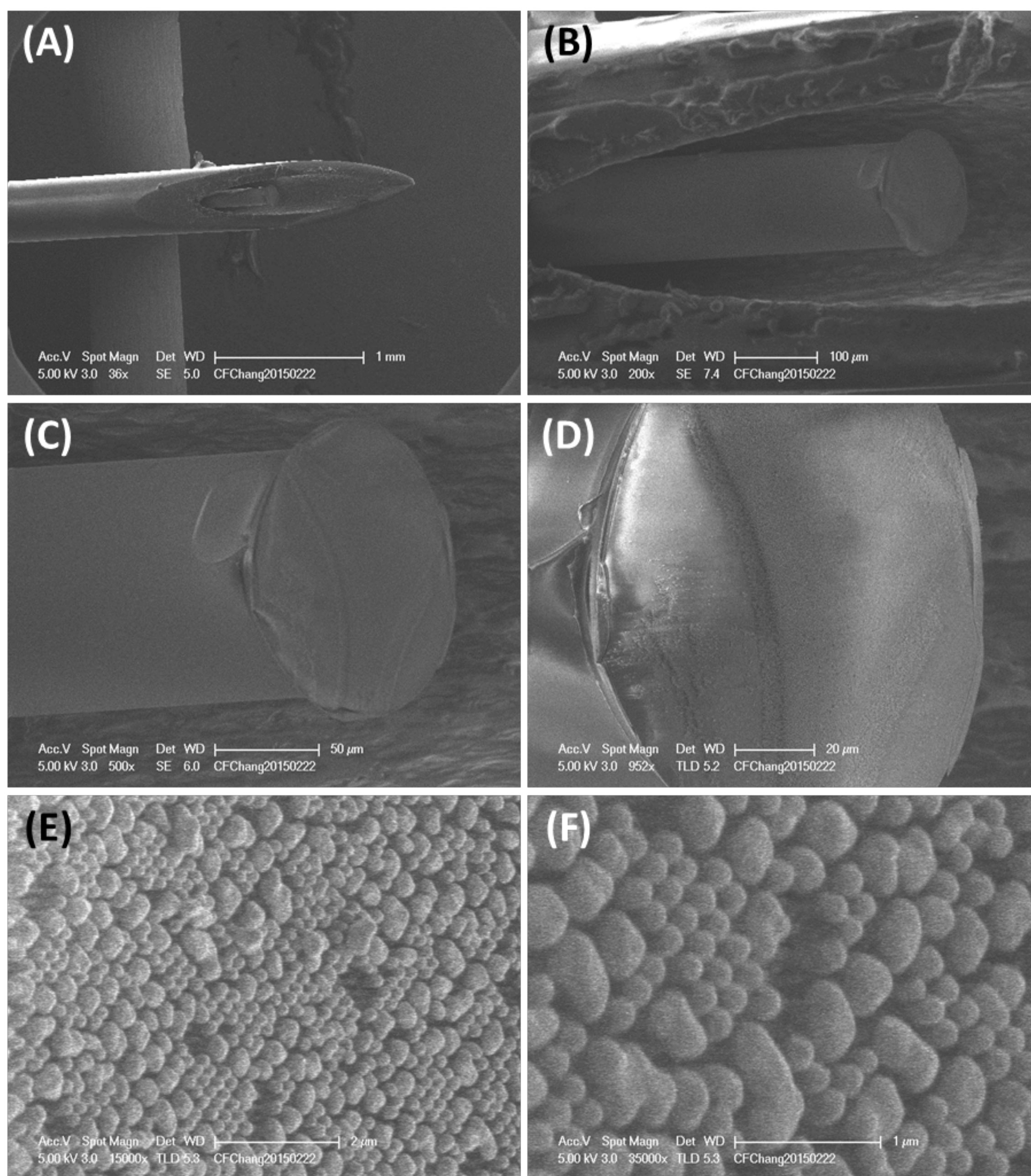

Figure 4.16 SEM micrographs of a SERS fiber in a hypodermic needle.

through a needle first before the bonding process, a gauge 30 needle can be readily used here.

With the SERS fiber ready, the all-fiber system can now be assembled. The system diagram is shown in Fig. 4.17 for the benchtop configuration, taking advantage of the Acton SpectraPro 2300i spectrometer already in the laboratory. To eliminate free-space optical alignment entirely, a fiber-based filter holder (Oz Optics REF-11-650-50/125-M-35-55-3-1-NF) is used for the edge filter (Semrock BLP01-633R-25). A notch filter blocking 632.8 nm can also be used instead of an edge filter. Even if the spectrometer can well resolve small Raman shifts not far away from the laser wavelength, it is still desirable to use a filter for a Raman system. First, the slight imperfection of the grating surface may scatter the pumping wavelength onto unrelated pixels as fake signals. Since the signal strength of the laser wavelength is strong, moreover, it would saturate the sensor chip immediately and force other signals to be integrated at a much shorter duration than otherwise allowed. The fiber input of the spectrometer consists of a bundle of 19 fibers with a total diameter of ~1.23 mm; to improve the coupling from the 50/125 μm multimode fiber to this fiber bundle, a 1000 μm core fiber patch cable (Thorlabs M35L01) was connected in between. All connectors are

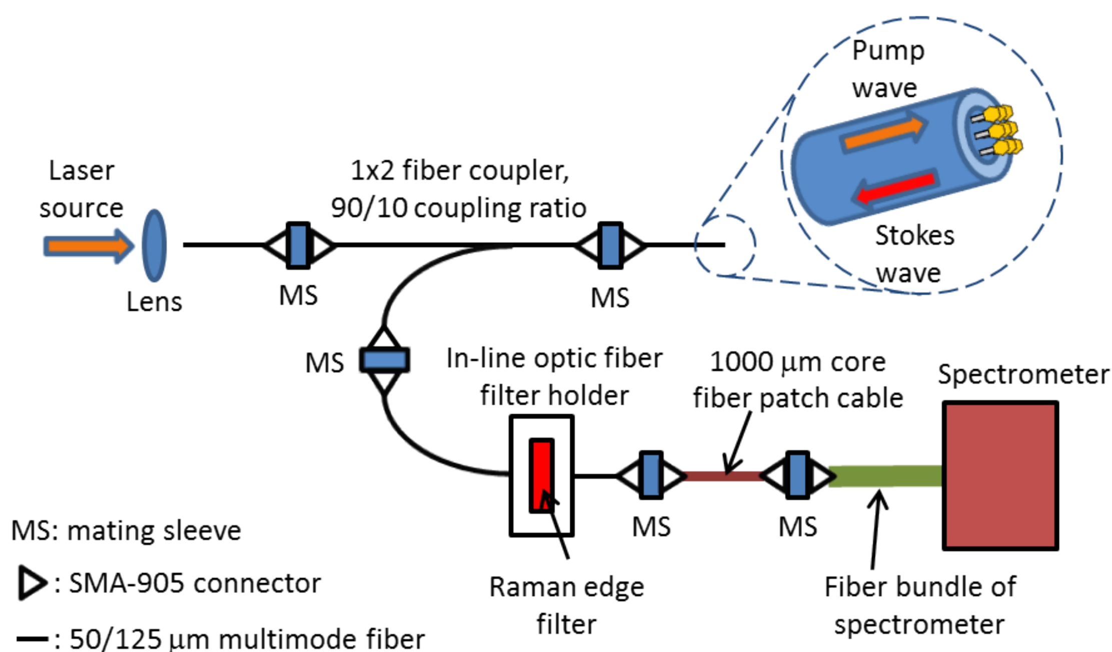

Figure 4.17 Schematic diagram of a benchtop all-fiber SERS system.

SMA-905 for convenience, and each SERS fiber can be mounted with an SMA connector for a quick change of SERS tips.

An important component in the whole system is the fiber coupler, which is the counterpart of a beam splitter in the free-space setup. In addition to the convenience of inherent alignment, it also circumvents the awkward situation for commercially-available beam splitters that the spectral range is either 400 – 700 or 700 – 1100 nm. Since the spectral range of interest for SERS applications is 400 – 2800 cm^{-1} to cover the Au-S and S-H virbrational modes, which corresponds to the wavelength range from ~650 to ~770 nm, typical beam splitters would not satisfy the requirement here. Multimode fiber couplers based on the fused biconical tapered (FBT) technology [168], on the other hand, can be designed for a wide range of central operation wavelength (at least 500 – 1500 nm), a large bandwidth (a few hundreds of nm), and various coupling ratios (from 50/50 to 1/99). As an example, the fiber coupler purchased for the system, Idealphotonics IDP-MS-1/2-1/9, can operate at least from 600 to 1100 nm. The availability of asymmetric coupling ratios is furthermore a big plus, since the back-reflected Stokes waves can now be mostly directed to the spectrometer instead of being lost at the other arm of the optical path. Figure 4.18 shows the two possible configurations of a 90/10 coupler. In Fig. 4.18 (A) 90% of the power would go to the opposite side, while in Fig. 4.18 (B) 90% of the power would stay along the same side. In either case, the spectrometer can be connected to the side to receive 90% of the signal, and this percentage can be further increase by choosing a 5/95 or 1/99 coupler. Due to the extremely high enhancement factor of SERS, the excitation power can be kept quite low; therefore, even only 10% of the illumination light would reach the SERS fiber tip, there would still be more than enough power for the SERS detection.

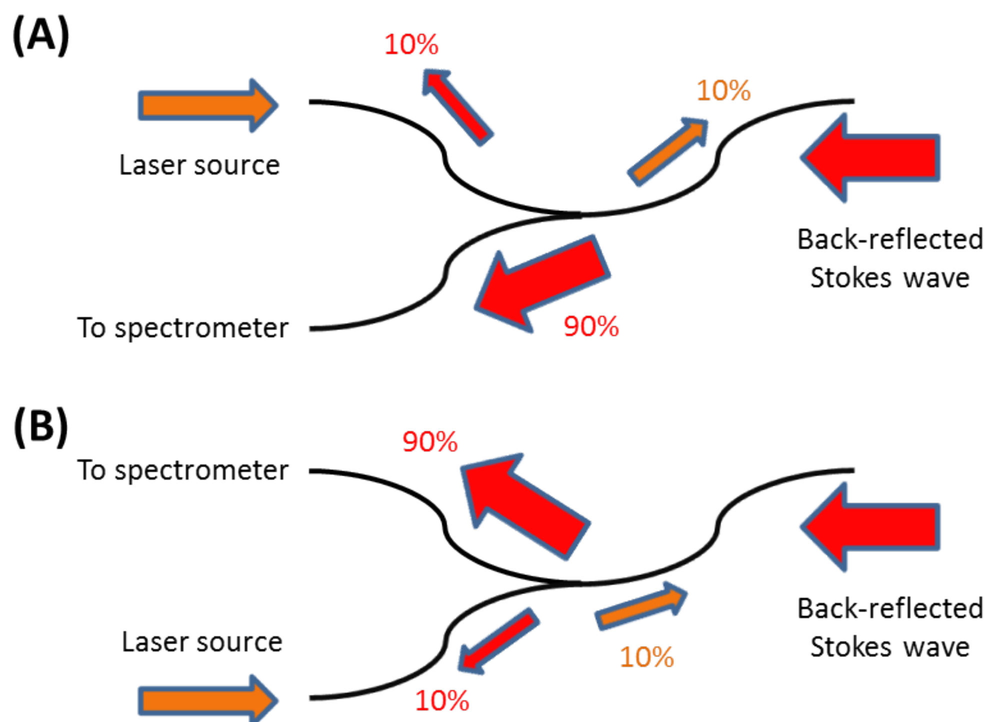

Figure 4.18 Working mechanism of 90/10 optical fiber coupler.

For in-field applications, a portable all-fiber SERS system can also be constructed. The system diagram can be seen in Fig. 4.19. The portable Raman spectrometer (Raman-HR-TEC), portable laser source (Ramulaser-638), and Raman probe (Raman-Probe-638) were purchased from StellarNet. Raman-HR-TEC covers the range of 200 – 3000 cm^{-1}, and can be thermoelectrically cooled for a resolution of 4 cm^{-1}. Raman-Probe-638 provides 50 mW of output at 638 nm, and can be battery-operated for 8 hours for mobile applications. By attaching the SERS fiber to the commercial Raman probe with a customized adapter, the whole system can be mobile and ready to use at any location.

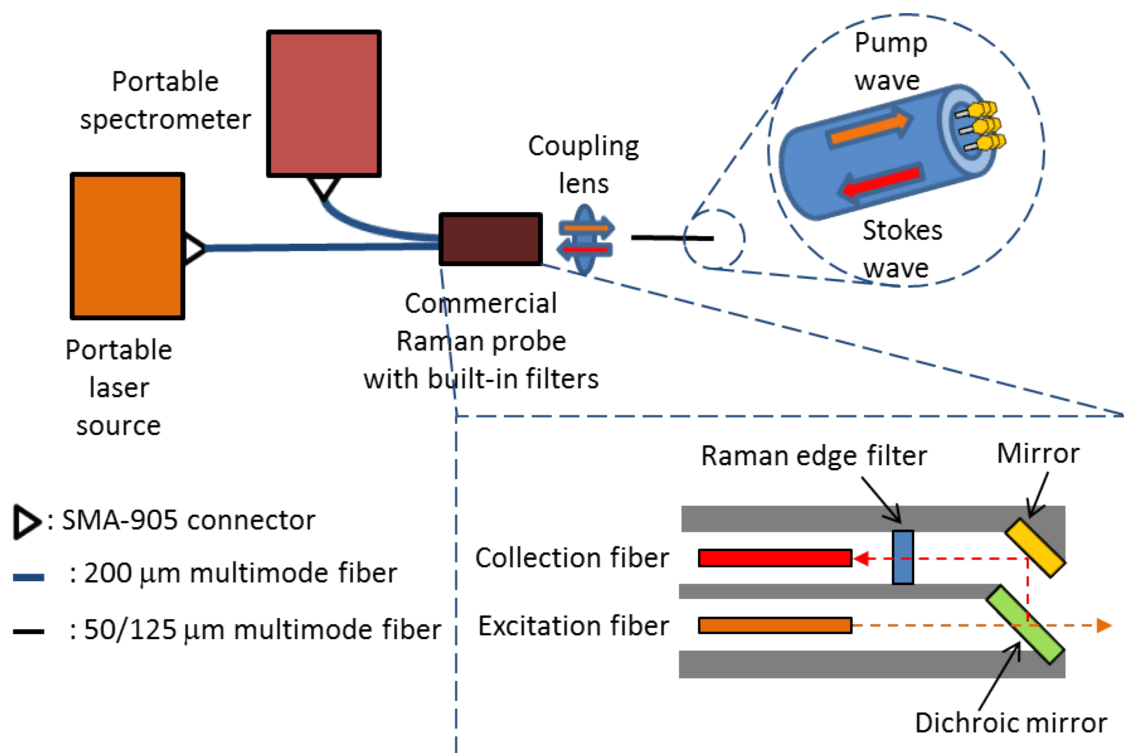

Figure 4.19 Schematic diagram of a portable all-fiber SERS system.

In addition to mobile or intravenous applications, the fiber-based system also enables remote sensing when the personnel or the Raman apparatus are far away from the sample of interest. For example, the fiber can extends miles long to monitor molecules of interest in the open field, while the technician stays indoors with all the laser and spectrometer for remote probing. Another potential application is for petroleum exploration. Based on the content of sulfur-based impurities, including H_2S, crude oil can be considered "sweet" or "sour" if the impurity level is below or above 0.5% [169]. Traditionally gas chromatography is called for to determine the level of these impurities, which is time-consuming and involves bulky equipment. With a portable all-fiber system, sulfur-containing compounds can readily bind onto Au nano-bulbs due to the high infinity, and each measurement would take only a few seconds.

Chapter 5

Conclusions and Future Directions

To briefly recapitulate, this thesis presents fabrication methods that are wafer-scalable for plasmonic metal nanostructures; the entire process flow can be immediately repeated in commercial semiconductor foundries for mass production. Extraordinary transmission (EOT) was studied for various metal types, nano-aperture patterns, and substrate choices; with transparent substrates like sapphire or glass, EOT devices are no longer fragile membranes and can instead be a mechanically robust biochemical assay. The hybrid fabrication approach also enables surface-enhanced Raman spectroscopy (SERS) to be deterministic, consistent, and repeatable not only from chip to chip, but wafer to wafer. Its huge enhancement was demonstrated with thiophenol, and with the fast acquisition time that ensued, binding dynamics of thrombin onto anti-thrombin aptamers could be well resolved. By heating up and cooling down the entire chip, the thermal dynamics of binding could also be well characterized. In addition to chip functionalization, this SERS platform could also readily detect substances like tracheal cytotoxin (TCT) and ethyl mercapatan without any sample preparation. The full Raman spectrum of TCT was obtained for the first time, and the results of ethyl mercapatan indicated great promise in the trace detection of hydrogen sulfide, a similar but highly poisonous gas. With some more fabrication steps, microfluidic channels can be integrated on the chip for easier use outside of a laboratory. The metal nanostructures can also be transferred to flexible substrates for surface conformation or SERS excitation from the other side. Nanocups, another family of metal nanostructures, also became available for adaptable designing and mass production in this manner. The Au nano-bulbs could also be mounted on a fiber tip, and an all-fiber SERS system could be assembled so that everything would be pre-aligned already. Without the need of arduous tweaking on site, portable applications are then possible, and the superior guiding capability of fibers means the system can monitor in-field signals kilometers away from the control center. The SERS fiber is also small enough to fit into a gauge 30 hypodermic needle, which would be very useful for clinical applications.

For EOT devices, the next steps include several exciting possibilities. Now that dense arrays of nanostructures can also be turned into EOT nano-apertures, additional shapes,

periodicity, and dimensions can be fabricated and measured. For each pattern, 3D sculpting can also be introduced to fine-tune the transmission characteristics even more. If 3D sculpting calls for thicker Si on the silicon-on-sapphire (SOS) chips, an additional layer of Si can be deposited first on top by, for example, plasma-enhanced chemical vapor deposition (PECVD). With proper design and etching, it is possible to block certain wavelengths and eliminate the use of filters in some applications, which would be a step further for system miniaturization. Since fabrication methods are available that do not involve thermal reflow, other metals like Cr, Cu, or Ag can be tested, which have been theoretically and experimentally shown to behave quite differently for extraordinary transmission [48, 170].

For EOT biochemical assays based on photo-uncaging, since the process was done with a photolithography machine, it would be convenient to use a photomask for defining areas to be photo-uncaged, as shown in Fig. 5.1 (A). Repeating these procedures could lead to multiplexed functionalization on a chip; since many cancer markers are degenerate, such a chip would be a promising sensor to pinpoint the exact type of cancer with a single test, compared with traditional approaches like quantitative polymerase chain reaction (qPCR) [171] that involve multiple iterations and call for a large amount of time and cost. On-chip super-resolution imaging is also possible from spectral transmission bands like Fig. 2.28 (E). When the incident polarization is rotated by 90°, the original wavelength of transmission is blocked, and another wavelength can pass through the nano-apertures instead. Since the distance between the binary components in each nano-pattern cell is known, the respective images corresponding to 90° polarization offsets can be deterministically combined in post-processing to present more information. If a digital imaging device is used right next to the EOT metal layer, the aforementioned feature means the resolution can be doubled when the pixel size is the same as the EOT cell dimension and when the structures are aligned during fabrication to the imaging pixels. Combining all these, it is then possible to make a smart petri dish that allows the simultaneous measurement of biochemical reaction and microscopy imaging as depicted in Fig. 5.1 (B). The EOT nano-apertures are fabricated on SOS or SOG substrates for mechanical strength, and are oriented so that the nano-apertures would face the CMOS sensor. The sample then flows between the nano-apertures and the CMOS sensor, for example through on-chip microfluidic structures. Light is then illuminated from the top.

Extractable, pre-aligned polarizers can be inserted along the grooves on the module for polarization-resolved measurement; for example, one polarizer can be aligned along the long side of rectangular nano-apertures, while the other along the short side. With all the pre-alignment, the interface would be user-friendly since the entire action is similar to inserting a memory card into a digital camera. In this configuration, the orthogonal spectral transmission bands like in Fig. 2.28 (E) can be exploited to double the effective pixel density of the CMOS sensor. The nano-apertures can also be functionalized in order to detect specific analytes in the sample flow, and optical signals like fluorescence can then be recorded by the CMOS sensor.

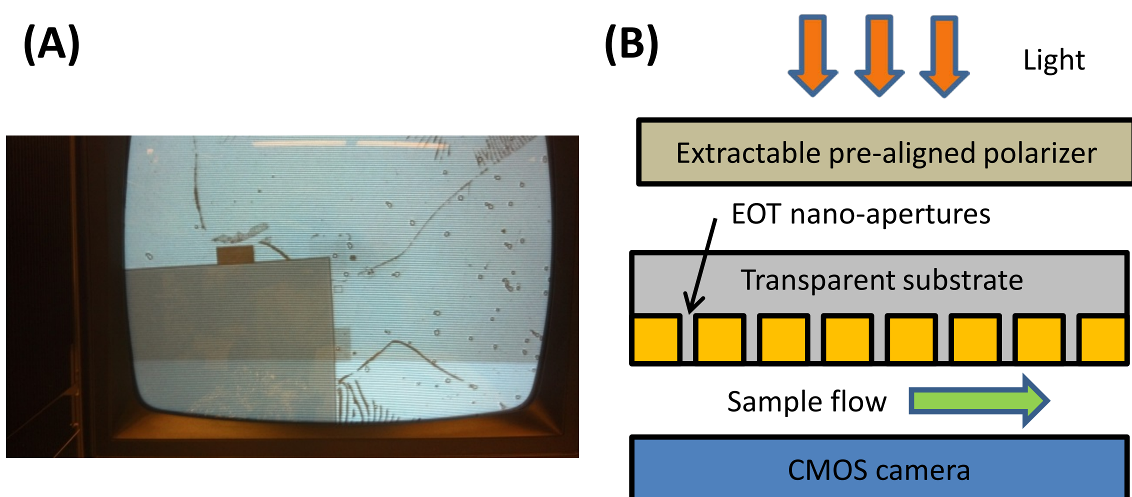

Figure 5.1 (A) Screenshot of a photomask covering portions of EOT nano-apertures for partial photo-uncaging. (B) Schematic diagram of a smart petri dish based on EOT nano-apertures.

Fiber-based SERS detection is surely one of the most exciting parts. A tissue phantom can be used first to test SERS fibers in a needle for further improvement; the fiber diameter can also be further reduced so that it fits into an even smaller needle. If the SERS fiber does not have to go through a needle, another configuration of the fiber tip can be implemented as shown in Fig. 5.2. First, techniques like the cryo etch can be employed to define the mesa region that would serve as the sidewall reflector at the end, as shown in Fig. 5.2 (A). Orientation-dependent etching like KOH can lead to the V-groove structure for fiber

placement on (100) Si wafers, as depicted in Fig. 5.2 (B). The pseudo Bosch etch can now define the nanopillars in Fig. 5.2 (C), followed by thermal oxidation as in Fig. 5.2 (D). After Au sputtering, thermal reflow, and fiber attachment, the final structure is shown in Fig. 5.2 (E). Laser scribing (shown as the dotted red lines) can further trim down the total size. Either type of the SERS fibers can be used for in-field detection, with hydrogen sulfide being the next goal. First, a gas-diluting setup will be built in the laboratory; the 2.16 ppm H_2S standard gas purchased from Praxair will be diluted repeatedly, and SERS chips will be exposed to each

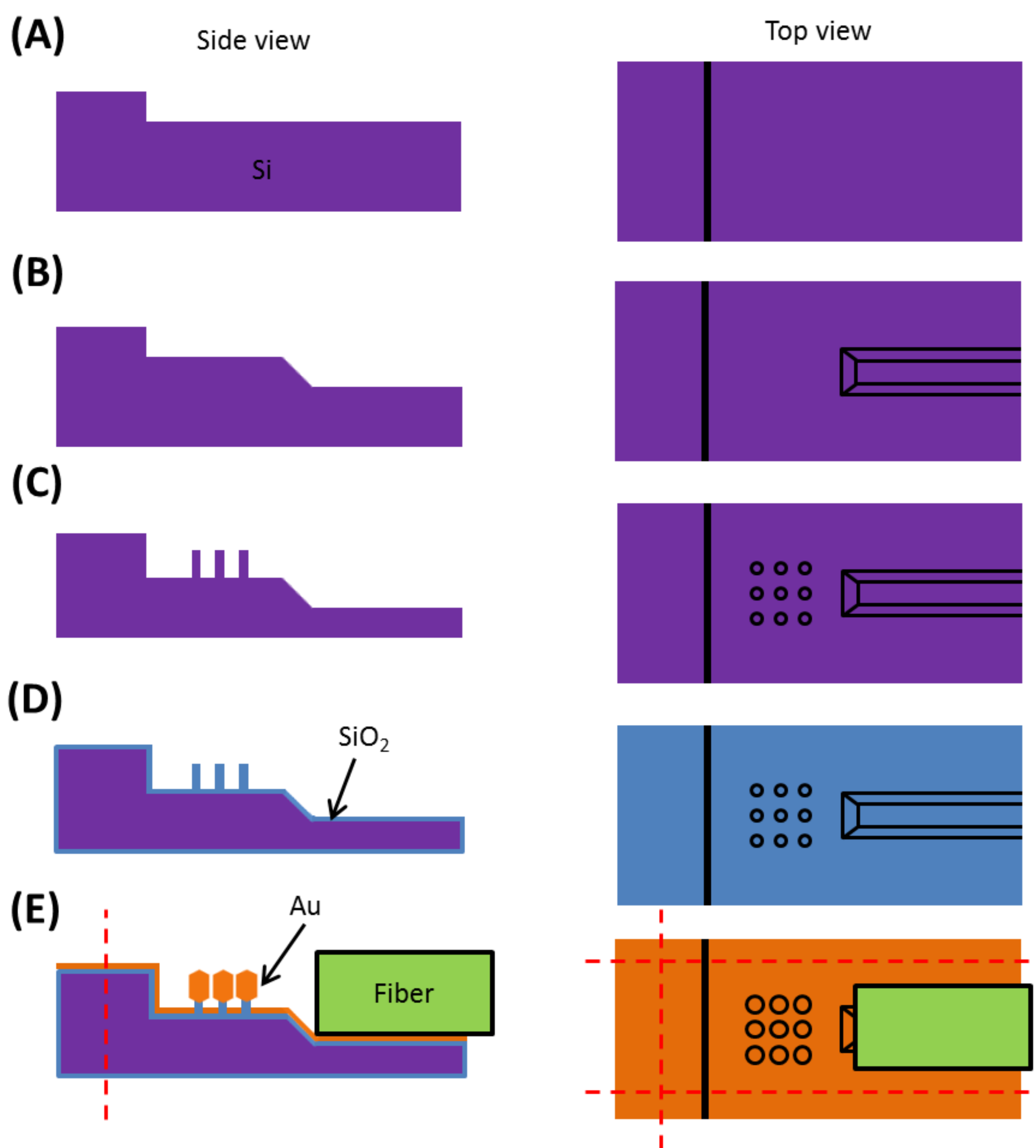

Figure 5.2 Schematic diagram of another configuration of SERS fiber tip.

lower concentration of H_2S and measured with a Raman microscope to determine the limit of detection. The experiment will then be repeated for the all-fiber system to compare the performance. For in-field applications, one possibility is to detect nitride-based compounds (organic or inorganic) in the air or soil to determine if plants need more fertilizer. Ammonium nitride, $(NH_4)_3N$, can be a good candidate for such a purpose. First, it is evaluated if the substance can bind onto Au nano-bulbs directly, or if further functionalization is desired to improve the efficacy. Microscope-based experiments would then be conducted to determine if the peak strength would correlate to the sample concentration.

To further improve the sensitivity of the SERS detection at a trace concentration – especially for single-molecule detection – it would be desirable for the biomolecule of interest to bind or adsorb themselves onto those SERS-active spots as described in Section 3.3 and shown in Fig. 5.3 (A) for convenience. Otherwise, it is likely for molecules to be away for locally-enhanced fields so that they do not get probed at all, as was possibly the case in Section 3.5.2 when a little bit of search was needed to find the signal from 500 fM of thrombin. Local field enhancement may be exploited again here [162]. The entire chip is first coated with a photo-sensitive material, and the illumination intensity is calibrated so that it does not exceed the threshold of photo-reaction for the general area. Around the hot spots between Au nano-bulbs the material may be exposed above the threshold or thermally ablated away, however, by choosing an appropriate material and by thermally reflowing Au into a suitable gap distance, as illustrated in Fig. 5.3 (B). After this process of self-aligned ablation or exposure (with an additional step of developing the chip), the hot spots are now accessible again as shown in Fig. 5.3 (C), and they can be functionalized as in Fig. 5.3 (D). Possible choices of functionalization include thiolated aptamers, antibodies, complimentary DNA (cDNA) segments, etc. When bio-molecules bind onto these spots, as a result, Raman signals will pick up their chemical fingerprints since those regions will again experience local field enhancement. A similar implementation can be done on nano-cups, with Fig. 5.3 (E) as one example from various configurations of nanocups. By proper design, the photo-sensitive material coating the insides of nanocups can be exposed or ablated, and self-aligned functionalization is again possible, as shown in Fig. 5.3 (F).

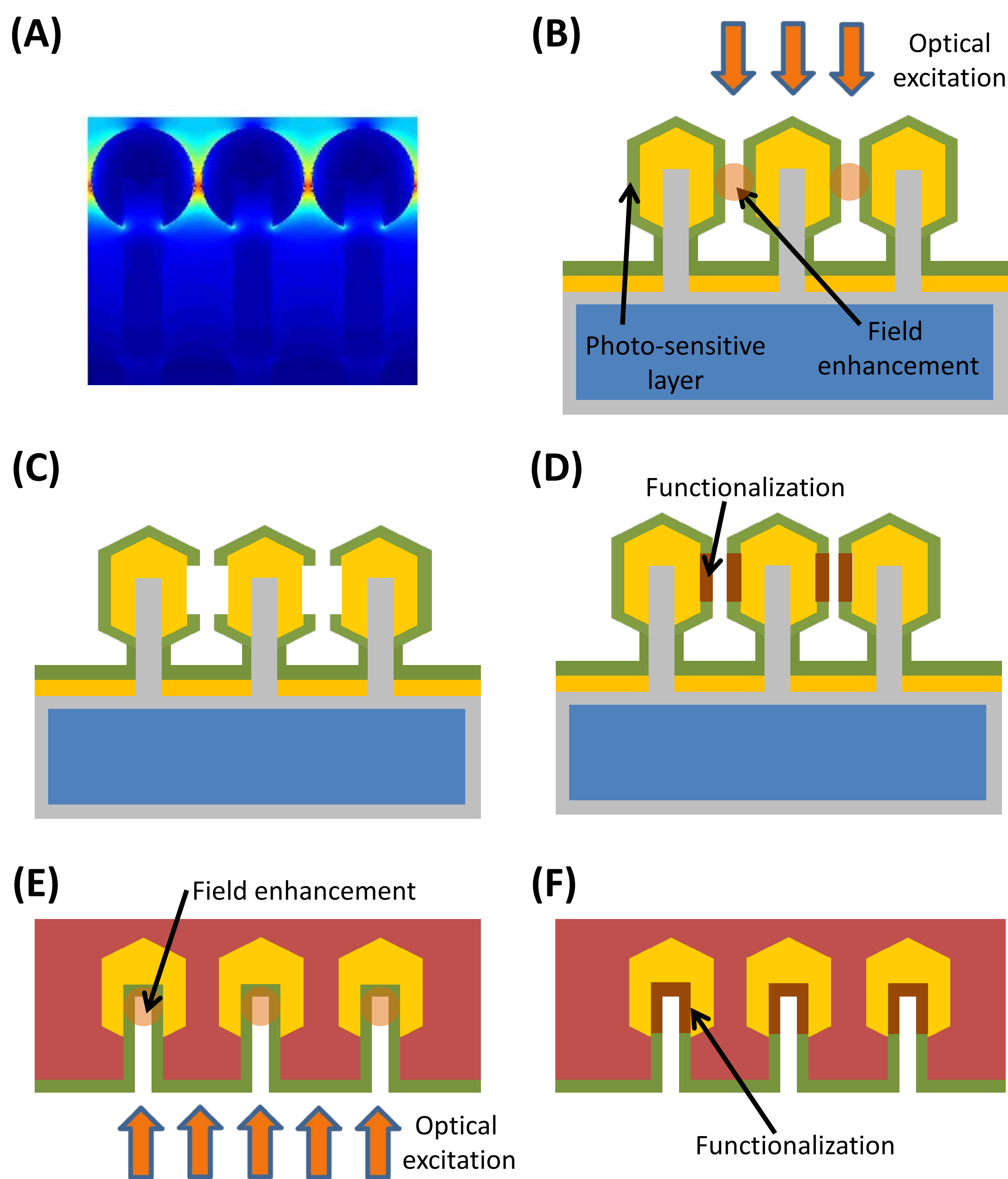

Figure 5.3 (A) Schematic of local field enhancement between Au nano-bulbs from numerical simulation. After the chip is coated with a photo-sensitive material, it can be illuminated at a correct amount of flux so that photo-reaction only takes place around the hot spots, as in (B). These spots are now accessible again as in (C), which can be functionalized as in (D). The same technique can be applied to the interior cavities of nanocups, as shown in (E) and (F).

Conformation onto non-flat surfaces can also be made better by fabricating recessed regions on flexible substrates in order to protect the integrity of plasmonic structures during the attachment [162]. As shown in Fig. 5.4 (A), the chip can be mounted on a carrier substrate first before the deposition of a flexible, transparent layer. As an alternative, the regions outside of the nano-patterns can be etched as in Fig. 5.4 (B); this can be done before the nanofabrication starts so that the nanostructures will be defined on a mesa, or after the nanofabrication by masking the nano-patterns with a protection layer during the etch. The flexible, transparent layer is then applied on top. After the removal of unnecessary regions, a sticker-like structure is available, as illustrated in Fig. 5.4 (C), which will be convenient for SERS detection on surfaces to probe volatile molecules released from the region of interest. Wearable SERS sensors on human skin for clinical purposes would be possible, or the device can be conformally attached to places like an endoscopic probe. If the nanopilllars are to be preserved, a thick sacrificial layer or an etched carrier chip can be an intermediate step, as shown in the left and right portion of Fig. 5.4 (D), respectively. The bottom Au layer has been removed with the technique described in Section 4.2 so that optical readout can be possible from the other side. Following similar processing steps as discussed earlier in this paragraph and in Section 4.2, upright SERS nanostructures in a flexible cavity can be achieved as in Fig. 5.4 (E). If the protruding nanostructures are removed as described in Section 2.1.6, it is also straightforward to apply the same process flow to transfer the nano-apertures into the configuration of Fig. 5.4 (F). The SiO_2 openings can be functionalized for further optical readout.

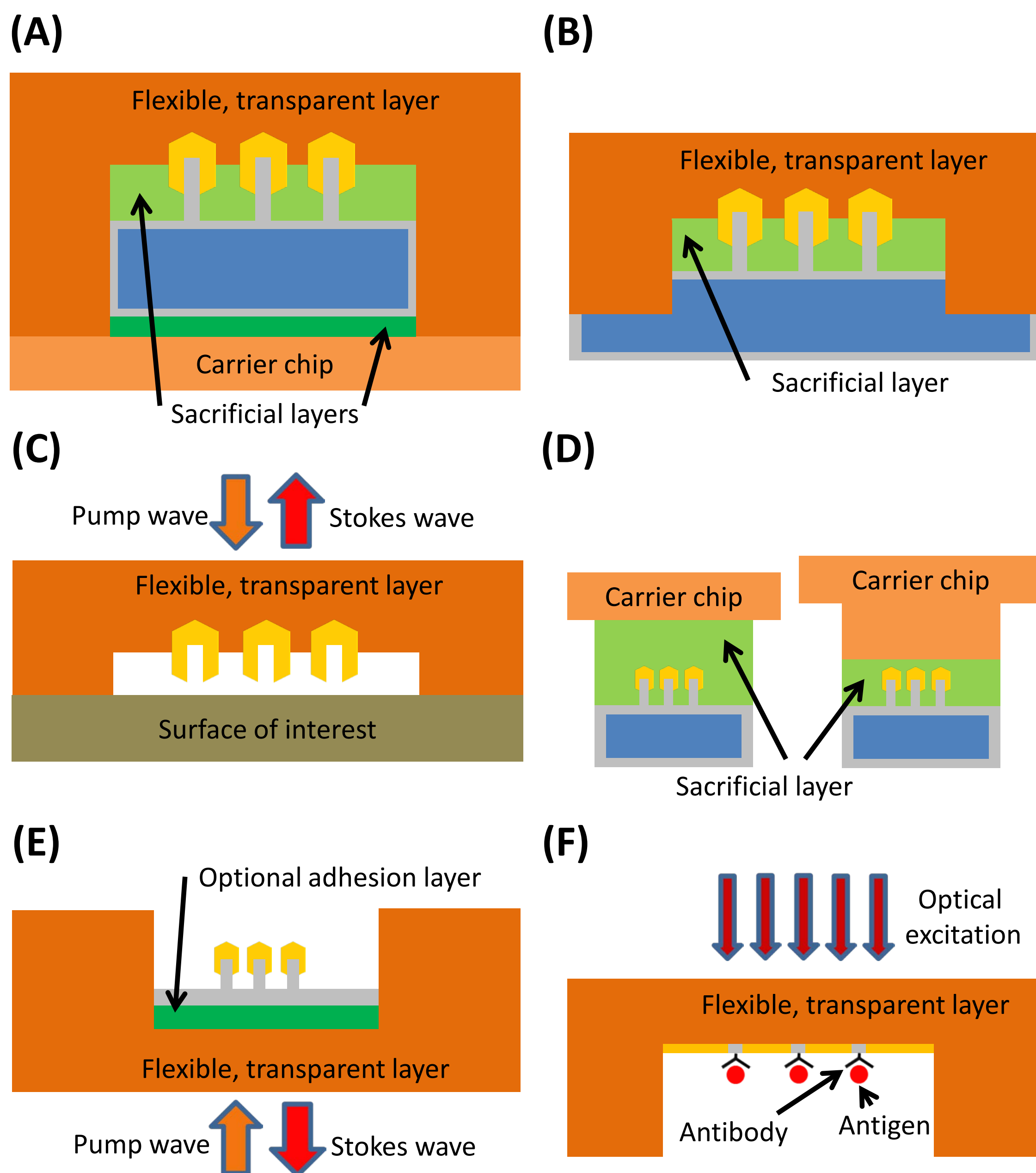

Figure 5.4 Fabrication of plasmonic nanostructures on a flexible sticker through (A) a carrier chip or (B) substrate etching. The final structure as (C) can conform onto a non-flat surface while preserving the nanostructures. In (D), with a thicker sacrificial layer (left) or an etched carrier chip (right), the patterns can be transferred upright as in (E). EOT nano-apertures can be processed in a similar way, as shown in (F).

Nanocups can be useful in other plasmonic applications such as optical nano-antennae [172], second harmonic generation [173], SERS [166], and so on. These nanostructures can be further shaped for an even greater degree of freedom [162]. Starting from Fig. 5.5 (A), where Au nano-bulbs have reflowed from the thermal treatment, specific regions of nano-bulbs can be reshaped with techniques like focused ion beam, as shown in Fig. 5.5 (B). If wafer-wide reshaping is desired, it can be done with procedures like Ar ion milling as in Fig. 5.5 (C). In both scenarios, the substrate can be tilted to reshape the nano-bulbs from a specific angle, and multiple rounds at different angles can be done for sophisticated sculpting. Instead of Au sputtering and thermal reflow, on the other hand, oxidized nanostructures as in Fig. 3.2 (C) can be shadow-evaporated as illustrated in Fig. 5.5 (D) so that the metal layer is deposited from an angle, and again it is optional to go for several rounds at different angles. The wafer

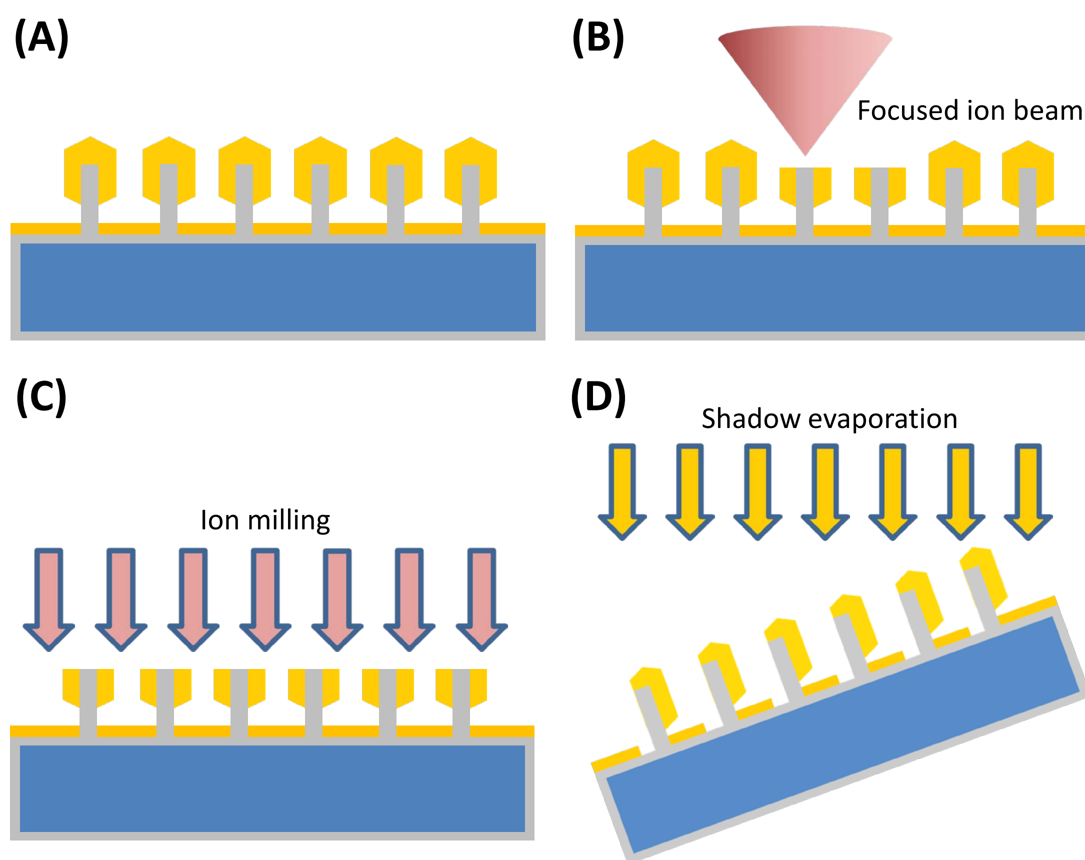

Figure 5.5 (A) Au nano-bulbs after thermal reflow, which can be topically shaped with focused ion beam as in (B) or generally modified with ion milling as in (C). Shadow evaporation can also be the method of metal deposition to fabricate asymmetric nanocups, as shown in (D).

can then go through the reshaping process if desired, again possibly for several times if necessary, followed by the transfer process as described in Section 4.2.

The power of wafer-scalable nanofabrication does not just stop here for the possible applications already mentioned. When it takes much less time, cost, and effort to make plasmonic devices, people can creatively design and try new patterns of various shapes and dimensions to explore additional possibilities. Predictions from theories and simulations can be verified experimentally in a timely fashion. When it is no longer a catastrophe to break a plasmonic device simply because it takes tens of hours to make a single chip, chemists and biologists can then have the peace of mind to try new methods of processing and functionalization. When it is more effective in time and cost to try something new, serendipitous discovery will also be much more likely to occur.

As a concluding remark, hopefully this thesis can contribute to the kind of influence that emulates the assembly line on automobile production. Henry Ford did not invent a new type of car that was far superior to contemporary vehicles, but by making the price of a Model T about one quarter of other cars, new business models associated with automobiles soon emerged and boomed. In the same light, it would be really great if this wafer-scalable method of nanofabrication can disseminate plasmonic devices to a wider audience so that the chips are no longer intricate samples in the hands of researchers and scientists, but versatile and affordable tools for the general public. With the huge potential of plasmonics in biomedical sensing, crowds of people can then benefit from new methods of health monitoring, early diagnosis, personalized medicine, and so on. As an engineering researcher, I look forward to seeing the advent of this day.

BIBLIOGRAPHY

1. S. E. Thompson, and S. Parthasarathy, "Moore's law: the future of Si microelectronics," *Materials Today* **9**, 20-25 (2006).

2. T. H. Maiman, "STIMULATED OPTICAL RADIATION IN RUBY," *Nature* **187**, 493-494 (1960).

3. M. Noginov, G. Zhu, A. Belgrave, R. Bakker, V. Shalaev, E. Narimanov, S. Stout, E. Herz, T. Suteewong, and U. Wiesner, "Demonstration of a spaser-based nanolaser," *Nature* **460**, 1110-1112 (2009).

4. K. Nozaki, S. Kita, and T. Baba, "Room temperature continuous wave operation and controlled spontaneous emission in ultrasmall photonic crystal nanolaser," *Optics Express* **15**, 7506-7514 (2007).

5. B. Cetinoneri, Y. A. Atesal, A. Fung, and G. M. Rebeiz, "W-band amplifiers with 6-dB noise figure and milliwatt-level 170–200-GHz doublers in 45-nm CMOS," *IEEE Transactions on Microwave Theory and Techniques* **60**, 692-701 (2012).

6. W. L. Barnes, A. Dereux, and T. W. Ebbesen, "Surface plasmon subwavelength optics," *Nature* **424**, 824-830 (2003).

7. S. A. Maier, and H. A. Atwater, "Plasmonics: Localization and guiding of electromagnetic energy in metal/dielectric structures," *Journal of Applied Physics* **98**, 011101 (2005).

8. S. Lal, S. Link, and N. J. Halas, "Nano-optics from sensing to waveguiding," *Nature Photonics* **1**, 641-648 (2007).

9. A. Yariv, and P. Yeh, "Photonics: optical electronics in modern communications" (Oxford University Press New York, 2007).

10. W. D. Wilson, "Analyzing biomolecular interactions," *Science* **295**, 2103-2105 (2002).

11. P. R. West, S. Ishii, G. V. Naik, N. K. Emani, V. M. Shalaev, and A. Boltasseva, "Searching for better plasmonic materials," *Laser & Photonics Reviews* **4**, 795-808 (2010).

12. H. Ehrenreich, H. Philipp, and B. Segall, "Optical properties of aluminum," *Physical Review* **132**, 1918 (1963).

13. Y. S. Chang, D. P. Kim, C. I. Kim, K. B. Sim, and E. G. Chang, "Etching characteristics of Au thin films using inductively coupled Cl 2/Ar plasma," *Journal of the Korean Physical Society* **42**, S791-S794 (2003).

14. S. Murarka, and C. Mogab, "Contamination of silicon and oxidized silicon wafers during plasma etching," *Journal of Electronic Materials* **8**, 763-779 (1979).

15. S. Park, Y. Lee, G. Yeom, S. Kim, H. Choe, and M. Hong, "Effects of additive gases on Ag etching using inductively coupled Cl2-based plasmas," *Journal of the Korean Physical Society* **42**, S804-S808 (2003).

16. V. M. Donnelly, and A. Kornblit, "Plasma etching: Yesterday, today, and tomorrow," *Journal of Vacuum Science & Technology A* **31**, 050825 (2013).

17. S. J. Pearton, and D. P. Norton, "Dry etching of electronic oxides, polymers, and semiconductors," *Plasma Processes and Polymers* **2**, 16-37 (2005).

18. L. Novotny, and N. Van Hulst, "Antennas for light," *Nature Photonics* **5**, 83-90 (2011).

19. H. ChuláJeon, and S. YeonáLee, "Optically tunable arrayed structures for highly sensitive plasmonic detection via simplified holographic lithography," *Journal of Materials Chemistry* **22**, 4603-4606 (2012).

20. D. Wasserman, E. Shaner, and J. Cederberg, "Midinfrared doping-tunable extraordinary transmission from sub-wavelength gratings," *Applied physics Letters* **90**, 191102-191102-191103 (2007).

21. M. Rycenga, C. M. Cobley, J. Zeng, W. Li, C. H. Moran, Q. Zhang, D. Qin, and Y. Xia, "Controlling the synthesis and assembly of silver nanostructures for plasmonic applications," *Chemical Reviews* **111**, 3669-3712 (2011).

22. V. M. Shalaev, W. Cai, U. K. Chettiar, H.-K. Yuan, A. K. Sarychev, V. P. Drachev, and A. V. Kildishev, "Negative index of refraction in optical metamaterials," *Optics Letters* **30**, 3356-3358 (2005).

23. G. Dolling, M. Wegener, C. M. Soukoulis, and S. Linden, "Negative-index metamaterial at 780 nm wavelength," *Optics Letters* **32**, 53-55 (2007).

24. P. Mühlschlegel, H.-J. Eisler, O. Martin, B. Hecht, and D. Pohl, "Resonant optical antennas," *Science* **308**, 1607-1609 (2005).

25. G. A. Wurtz, R. Pollard, W. Hendren, G. Wiederrecht, D. Gosztola, V. Podolskiy, and A. V. Zayats, "Designed ultrafast optical nonlinearity in a plasmonic nanorod metamaterial enhanced by nonlocality," *Nature Nanotechnology* **6**, 107-111 (2011).

26. N. Fang, H. Lee, C. Sun, and X. Zhang, "Sub–diffraction-limited optical imaging with a silver superlens," *Science* **308**, 534-537 (2005).

27. Z. Liu, H. Lee, Y. Xiong, C. Sun, and X. Zhang, "Far-field optical hyperlens magnifying sub-diffraction-limited objects," *Science* **315**, 1686-1686 (2007).

28. C. M. Galloway, M. P. Kreuzer, S. S. Aćimović, G. Volpe, M. Correia, S. B. Petersen, M. T. Neves-Petersen, and R. Quidant, "Plasmon-assisted delivery of single nano-objects in an optical hot spot," *Nano Letters* **13**, 4299-4304 (2013).

29. A. Krasavin, and A. Zayats, "Photonic signal processing on electronic scales: electro-optical field-effect nanoplasmonic modulator," *Physical Review Letters* **109**, 053901 (2012).

30. A. A. Yanik, M. Huang, O. Kamohara, A. Artar, T. W. Geisbert, J. H. Connor, and H. Altug, "An optofluidic nanoplasmonic biosensor for direct detection of live viruses from biological media," *Nano Letters* **10**, 4962-4969 (2010).

31. A. Sengupta, M. Mujacic, and E. J. Davis, "Detection of bacteria by surface-enhanced Raman spectroscopy," *Analytical and Bioanalytical Chemistry* **386**, 1379-1386 (2006).

32. J. N. Anker, W. P. Hall, O. Lyandres, N. C. Shah, J. Zhao, and R. P. Van Duyne, "Biosensing with plasmonic nanosensors," *Nature Materials* **7**, 442-453 (2008).

33. S. S. Walavalkar, P. Latawiec, A. P. Homyk, Scherer, and Axel, "Scalable Method for the Fabrication and Testing of Glass-Filled, Three-Dimensionally Sculpted Extraordinary Transmission Apertures," *Nano Letters* **14**, 311-317 (2013).

34. H. Bethe, "Theory of diffraction by small holes," *Physical Review* **66**, 163 (1944).

35. C. J. Bouwkamp, "Diffraction theory," *Reports on Progress in Physics* **17**, 35 (1954).

36. T. W. Ebbesen, H. Lezec, H. Ghaemi, T. Thio, and P. Wolff, "Extraordinary optical transmission through sub-wavelength hole arrays," *Nature* **391**, 667-669 (1998).

37. M. Beruete, M. Sorolla, I. Campillo, J. Dolado, L. Martín-Moreno, J. Bravo-Abad, and F. García-Vidal, "Enhanced millimeter wave transmission through quasioptical subwavelength perforated plates," *IEEE Transactions on Antennas and Propagation* **53**, 1897-1903 (2005).

38. H.-T. Chen, H. Lu, A. K. Azad, R. D. Averitt, A. C. Gossard, S. A. Trugman, J. F. O'Hara, and A. J. Taylor, "Electronic control of extraordinary terahertz transmission through subwavelength metal hole arrays," *Optics Express* **16**, 7641-7648 (2008).

39. L. Martin-Moreno, F. Garcia-Vidal, H. Lezec, K. Pellerin, T. Thio, J. Pendry, and T. Ebbesen, "Theory of extraordinary optical transmission through subwavelength hole arrays," *Physical Review Letters* **86**, 1114 (2001).

40. Z. Fan, L. Zhan, X. Hu, and Y. Xia, "Critical process of extraordinary optical transmission through periodic subwavelength hole array: Hole-assisted evanescent-field coupling," *Optics Communications* **281**, 5467-5471 (2008).

41. C. Genet, and T. Ebbesen, "Light in tiny holes," *Nature* **445**, 39-46 (2007).

42. L. Moreno, and F. García-Vidal, "Optical transmission through circular hole arrays in optically thick metal films," *Optics Express* **12**, 3619-3628 (2004).

43. P. Lalanne, J. Rodier, and J. Hugonin, "Surface plasmons of metallic surfaces perforated by nanohole arrays," *Journal of Optics A: Pure and Applied Optics* **7**, 422 (2005).

44. R. M. Roth, N. C. Panoiu, M. M. Adams, J. I. Dadap, and R. M. Osgood Jr, "Polarization-tunable plasmon-enhanced extraordinary transmission through metallic films using asymmetric cruciform apertures," *Optics Letters* **32**, 3414-3416 (2007).

45. X. Zhang, Z. Li, S. Ye, S. Wu, J. Zhang, L. Cui, A. Li, T. Wang, S. Li, and B. Yang, "Elevated Ag nanohole arrays for high performance plasmonic sensors based on extraordinary optical transmission," *Journal of Materials Chemistry* **22**, 8903-8910 (2012).

46. K.-L. Lee, W.-S. Wang, and P.-K. Wei, "Sensitive label-free biosensors by using gap plasmons in gold nanoslits," *Biosensors and Bioelectronics* **24**, 210-215 (2008).

47. A. G. Brolo, R. Gordon, B. Leathem, and K. L. Kavanagh, "Surface plasmon sensor based on the enhanced light transmission through arrays of nanoholes in gold films," *Langmuir* **20**, 4813-4815 (2004).

48. F. Przybilla, A. Degiron, J. Laluet, C. Genet, and T. Ebbesen, "Optical transmission in perforated noble and transition metal films," *Journal of Optics A: Pure and Applied Optics* **8**, 458 (2006).

49. C. Lehrer, L. Frey, S. Petersen, M. Mizutani, M. Takai, and H. Ryssel, "Defects and gallium-contamination during focused ion beam micro machining," in *IEEE Conference on Ion Implantation Technology*, pp. 695-698 (2000).

50. Y. Ekinci, H. H. Solak, and C. David, "Extraordinary optical transmission in the ultraviolet region through aluminum hole arrays," *Optics Letters* **32**, 172-174 (2007).

51. S. Chuang, H. Chen, S. Kuo, Y. Lai, and C. Lee, "Using direct nanoimprinting to study extraordinary transmission in textured metal films," *Optics Express* **16**, 2415-2422 (2008).

52. C.-f. Chang, S. S. Walavalkar, B. Marin, and A. Scherer, "Top-Down Designing and Fabrication of Metal Nanostructures for Plasmonics-Assisted Biomedical Sensing Applications," in *IEEE EMBS Micro and Nanotechnology in Medicine Conference*, MoET1.44 (2014).

53. M. D. Henry, "ICP etching of silicon for micro and nanoscale devices," Ph.D. thesis, Department of Applied Physics, California Institute of Technology, Pasadena, CA, U.S.A. (2010).

54. S. S. Walavalkar, "Optical, mechanical, and electronic properties of etched silicon nanopillars," Ph.D. thesis, Department of Applied Physics, California Institute of Technology, Pasadena, CA, U.S.A., (2011).

55. K. R. Williams, K. Gupta, and M. Wasilik, "Etch rates for micromachining processing-Part II," *Journal of Microelectromechanical Systems* **12**, 761-778 (2003).

56. A. Pinardi, S. Leake, R. Felici, and I. Robinson, "Formation of an Au-Si eutectic on a clean silicon surface," *Physical Review B* **79**, 045416 (2009).

57. O. Nast, T. Puzzer, L. M. Koschier, A. B. Sproul, and S. R. Wenham, "Aluminum-induced crystallization of amorphous silicon on glass substrates above and below the eutectic temperature," *Applied Physics Letters* **73**, 3214-3216 (1998).

58. B. Lom, K. E. Healy, and P. E. Hockberger, "A versatile technique for patterning biomolecules onto glass coverslips," *Journal of Neuroscience Methods* **50**, 385-397 (1993).

59. M. Fedurco, A. Romieu, S. Williams, I. Lawrence, and G. Turcatti, "BTA, a novel reagent for DNA attachment on glass and efficient generation of solid-phase amplified DNA colonies," *Nucleic Acids Research* **34**, e22-e22 (2006).

60. H. Chen, X. Hou, G. Li, F. Zhang, M. Yu, and X. Wang, "Passivation of porous silicon by wet thermal oxidation," *Journal of Applied Physics* **79**, 3282-3285 (1996).

61. A. J. Bard, R. Parsons, and J. Jordan, "Standard potentials in aqueous solution" (CRC press, 1985).

62. G. G. Shahidi, "SOI technology for the GHz era," *IBM Journal of Research and Development* **46**, 121-131 (2002).

63. S. Lai, S. Srinivasan, R. J. Westerman, D. Johnson, and J. J. Nolan, "Notch reduction in silicon on insulator (SOI) structures using a time division multiplex etch processes," in *Conference on MOEMS-MEMS Micro & Nanofabrication*, pp. 33-38 (2005).

64. H. Manasevit, and W. Simpson, "Single-Crystal Silicon on a Sapphire Substrate," *Journal of Applied Physics* **35**, 1349-1351 (1964).

65. M. A. Green, "Self-consistent optical parameters of intrinsic silicon at 300K including temperature coefficients," *Solar Energy Materials and Solar Cells* **92**, 1305-1310 (2008).

66. E. A. Dobisz, R. Bass, S. L. Brandow, M.-S. Chen, and W. J. Dressick, "Electroless metal discharge layers for electron beam lithography," *Applied Physics Letters* **82**, 478-480 (2003).

67. M. Angelopoulos, "Conducting polymers in microelectronics," *IBM Journal of Research and Development* **45**, 57-75 (2001).

68. J. Joo, B. Y. Chow, and J. M. Jacobson, "Nanoscale patterning on insulating substrates by critical energy electron beam lithography," *Nano Letters* **6**, 2021-2025 (2006).

69. Y. Shevchenko, C. Chen, M. Dakka, and J. Albert, "Polarization-selective grating excitation of plasmons in cylindrical optical fibers," *Optics Letters* **35**, 637-639 (2010).

70. E. Hecht, "Optics" (Pearson Education, Limited, 2013).

71. Y. M. Strelniker, "Theory of optical transmission through elliptical nanohole arrays," *Physical Review B* **76**, 085409 (2007).

72. B. E. Saleh, and M. C. Teich, "Fundamentals of photonics" (Wiley Series in Pure an Applied Optics, 2007).

73. K. Ray, M. H. Chowdhury, and J. R. Lakowicz, "Aluminum nanostructured films as substrates for enhanced fluorescence in the ultraviolet-blue spectral region," *Analytical Chemistry* **79**, 6480-6487 (2007).

74. V. R. Shembekar, Y. Chen, B. K. Carpenter, and G. P. Hess, "A protecting group for carboxylic acids that can be photolyzed by visible light," *Biochemistry* **44**, 7107-7114 (2005).

75. M. J. Weber, "Handbook of optical materials" (CRC press, 2002).

76. C. V. Raman, and K. S. Krishnan, "A new type of secondary radiation," *Nature* **121**, 501-502 (1928).

77. P. Maker, and R. Terhune, "Study of optical effects due to an induced polarization third order in the electric field strength," *Physical Review* **137**, A801 (1965).

78. A. Zumbusch, G. R. Holtom, and X. S. Xie, "Three-dimensional vibrational imaging by coherent anti-Stokes Raman scattering," *Physical Review Letters* **82**, 4142 (1999).

79. C. W. Freudiger, W. Min, B. G. Saar, S. Lu, G. R. Holtom, C. He, J. C. Tsai, J. X. Kang, and X. S. Xie, "Label-free biomedical imaging with high sensitivity by stimulated Raman scattering microscopy," *Science* **322**, 1857-1861 (2008).

80. J. T. Verdeyen, "Laser Electronics," (Prentice-Hall, 1995).

81. M. Fleischmann, P. J. Hendra, and A. McQuillan, "Raman spectra of pyridine adsorbed at a silver electrode," *Chemical Physics Letters* **26**, 163-166 (1974).

82. K. Kneipp, Y. Wang, H. Kneipp, L. T. Perelman, I. Itzkan, R. R. Dasari, and M. S. Feld, "Single molecule detection using surface-enhanced Raman scattering (SERS)," *Physical Review Letters* **78**, 1667 (1997).

83. J. Jiang, K. Bosnick, M. Maillard, and L. Brus, "Single molecule Raman spectroscopy at the junctions of large Ag nanocrystals," *The Journal of Physical Chemistry B* **107**, 9964-9972 (2003).

84. K. Kneipp, H. Kneipp, V. B. Kartha, R. Manoharan, G. Deinum, I. Itzkan, R. R. Dasari, and M. S. Feld, "Detection and identification of a single DNA base molecule using surface-enhanced Raman scattering (SERS)," *Physical Review E* **57**, R6281 (1998).

85. J. Zhang, J. Malicka, I. Gryczynski, and J. R. Lakowicz, "Surface-enhanced fluorescence of fluorescein-labeled oligonucleotides capped on silver nanoparticles," *The Journal of Physical Chemistry B* **109**, 7643-7648 (2005).

86. R. Antoine, M. Pellarin, B. Palpant, M. Broyer, B. Prevel, P. Galletto, P. Brevet, and H. Girault, "Surface plasmon enhanced second harmonic response from gold clusters embedded in an alumina matrix," *Journal of Applied Physics* **84**, 4532-4536 (1998).

87. A. M. Michaels, M. Nirmal, and L. Brus, "Surface enhanced Raman spectroscopy of individual rhodamine 6G molecules on large Ag nanocrystals," *Journal of the American Chemical Society* **121**, 9932-9939 (1999).

88. M. S. Schmidt, J. Hübner, and A. Boisen, "Large area fabrication of leaning silicon nanopillars for surface enhanced Raman spectroscopy," *Advanced Materials* **24**, OP11-OP18 (2012).

89. V. L. De Los Santos, D. Lee, J. Seo, F. L. Leon, D. A. Bustamante, S. Suzuki, Y. Majima, T. Mitrelias, A. Ionescu, and C. H. Barnes, "Crystallization and surface morphology of Au/SiO2 thin films following furnace and flame annealing," *Surface Science* **603**, 2978-2985 (2009).

90. C. S. Kumar, "Raman spectroscopy for nanomaterials characterization" (Springer Science & Business Media, 2012).

91. M. Hu, J. Chen, Z.-Y. Li, L. Au, G. V. Hartland, X. Li, M. Marquez, and Y. Xia, "Gold nanostructures: engineering their plasmonic properties for biomedical applications," *Chemical Society Reviews* **35**, 1084-1094 (2006).

92. T. Niebauer, J. E. Faller, H. Godwin, J. L. Hall, and R. Barger, "Frequency stability measurements on polarization-stabilized He-Ne lasers," *Applied Optics* **27**, 1285-1289 (1988).

93. J. J. Baraga, M. S. Feld, and R. P. Rava, "Rapid near-infrared Raman spectroscopy of human tissue with a spectrograph and CCD detector," *Applied Spectroscopy* **46**, 187-190 (1992).

94. S. W. Raso, P. L. Clark, C. Haase-Pettingell, J. King, and G. J. Thomas, "Distinct cysteine sulfhydryl environments detected by analysis of Raman SH markers of Cys→ Ser mutant proteins," *Journal of Molecular Biology* **307**, 899-911 (2001).

95. A. J. Leavitt, and T. P. Beebe, "Chemical reactivity studies of hydrogen sulfide on Au (111)," *Surface Science* **314**, 23-33 (1994).

96. H. Wang, C. S. Levin, and N. J. Halas, "Nanosphere arrays with controlled sub-10-nm gaps as surface-enhanced Raman spectroscopy substrates," *Journal of the American Chemical Society* **127**, 14992-14993 (2005).

97. H. Y. Jung, Y.-K. Park, S. Park, and S. K. Kim, "Surface enhanced Raman scattering from layered assemblies of close-packed gold nanoparticles," *Analytica Chimica Acta* **602**, 236-243 (2007).

98. C. M. Whelan, C. J. Barnes, C. G. Walker, and N. M. Brown, "Benzenethiol adsorption on Au (111) studied by synchrotron ARUPS, HREELS and XPS," *Surface Science* **425**, 195-211 (1999).

99. M. Mahmoud, and M. El-Sayed, "Aggregation of gold nanoframes reduces, rather than enhances, SERS efficiency due to the trade-off of the inter-and intraparticle plasmonic fields," *Nano Letters* **9**, 3025-3031 (2009).

100. E. J. Bastian Jr, and R. B. Martin, "Disulfide vibrational spectra in the sulfur-sulfur and carbon-sulfur stretching region," *The Journal of Physical Chemistry* **77**, 1129-1133 (1973).

101. C.-C. Chang, H.-L. Wu, C.-H. Kuo, and M. H. Huang, "Hydrothermal synthesis of monodispersed octahedral gold nanocrystals with five different size ranges and their self-assembled structures," *Chemistry of Materials* **20**, 7570-7574 (2008).

102. X.-L. Tang, P. Jiang, G.-L. Ge, M. Tsuji, S.-S. Xie, and Y.-J. Guo, "Poly (N-vinyl-2-pyrrolidone)(PVP)-capped dendritic gold nanoparticles by a one-step hydrothermal route and their high SERS effect," *Langmuir* **24**, 1763-1768 (2008).

103. C. J. Orendorff, A. Gole, T. K. Sau, and C. J. Murphy, "Surface-enhanced Raman spectroscopy of self-assembled monolayers: sandwich architecture and nanoparticle shape dependence," *Analytical Chemistry* **77**, 3261-3266 (2005).

104. A. Vial, A.-S. Grimault, D. Macías, D. Barchiesi, and M. L. de La Chapelle, "Improved analytical fit of gold dispersion: Application to the modeling of extinction spectra with a finite-difference time-domain method," *Physical Review B* **71**, 085416 (2005).

105. E. Le Ru, and P. Etchegoin, "Principles of Surface-Enhanced Raman Spectroscopy: and related plasmonic effects" (Elsevier, 2008).

106. K. Kneipp, R. R. Dasari, and Y. Wang, "Near-infrared surface-enhanced Raman scattering (NIR SERS) on colloidal silver and gold," *Applied Spectroscopy* **48**, 951-955 (1994).

107. E. Le Ru, E. Blackie, M. Meyer, and P. G. Etchegoin, "Surface enhanced Raman scattering enhancement factors: a comprehensive study," *The Journal of Physical Chemistry C* **111**, 13794-13803 (2007).

108. Y. Suzaki, and A. Tachibana, "Measurement of the μm sized radius of Gaussian laser beam using the scanning knife-edge," *Applied Optics* **14**, 2809-2810 (1975).

109. J. Parker Jr, D. Feldman, and M. Ashkin, "Raman scattering by silicon and germanium," *Physical Review* **155**, 712 (1967).

110. R. Rosenthal, W. Nogami, B. Cookson, W. Goldman, and W. Folkening, "Major fragment of soluble peptidoglycan released from growing Bordetella pertussis is tracheal cytotoxin," *Infection and Immunity* **55**, 2117-2120 (1987).

111. B. T. Cookson, A. N. Tyler, and W. E. Goldman, "Primary structure of the peptidoglycan-derived tracheal cytotoxin of Bordetella pertussis," *Biochemistry* **28**, 1744-1749 (1989).

112. J. G. Magalhaes, D. J. Philpott, M. A. Nahori, M. Jéhanno, J. Fritz, L. Bourhis, J. Viala, J. P. Hugot, M. Giovannini, and J. Bertin, "Murine Nod1 but not its human orthologue mediates innate immune detection of tracheal cytotoxin," *EMBO Reports* **6**, 1201-1207 (2005).

113. M. Dauchez, P. Lagant, P. Derreumaux, G. Vergoten, M. Sekkal, and B. Sombret, "Force field and vibrational spectra of oligosaccharides with different glycosidic linkages—Part II. Maltose monohydrate, cellobiose and gentiobiose," *Spectrochimica Acta Part A: Molecular Spectroscopy* **50**, 105-118 (1994).

114. R. M. Jarvis, and R. Goodacre, "Discrimination of bacteria using surface-enhanced Raman spectroscopy," *Analytical Chemistry* **76**, 40-47 (2004).

115. N. P. Ivleva, M. Wagner, H. Horn, R. Niessner, and C. Haisch, "Towards a nondestructive chemical characterization of biofilm matrix by Raman microscopy," *Analytical and Bioanalytical Chemistry* **393**, 197-206 (2009).

116. J. Suh, and M. Moskovits, "Surface-enhanced Raman spectroscopy of amino acids and nucleotide bases adsorbed on silver," *Journal of the American Chemical Society* **108**, 4711-4718 (1986).

117. A. Barth, and C. Zscherp, "What vibrations tell about proteins," *Quarterly Reviews of Biophysics* **35**, 369-430 (2002).

118. S. Song, and S. A. Asher, "UV resonance Raman studies of peptide conformation in poly (L-lysine), poly (L-glutamic acid), and model complexes: the basis for protein secondary structure determinations," *Journal of the American Chemical Society* **111**, 4295-4305 (1989).

119. C. V. Pagba, S. M. Lane, H. Cho, and S. Wachsmann-Hogiu, "Direct detection of aptamer-thrombin binding via surface-enhanced Raman spectroscopy," *Journal of Biomedical Optics* **15**, 047006 (2010).

120. I. N. Serdyuk, N. R. Zaccai, and J. Zaccai, "Methods in molecular biophysics: structure, dynamics, function" (Cambridge University Press, 2007).

121. L. Zeiri, B. Bronk, Y. Shabtai, J. Eichler, and S. Efrima, "Surface-enhanced Raman spectroscopy as a tool for probing specific biochemical components in bacteria," *Applied Spectroscopy* **58**, 33-40 (2004).

122. K. De Vos, I. Bartolozzi, E. Schacht, P. Bienstman, and R. Baets, "Silicon-on-Insulator microring resonator for sensitive and label-free biosensing," *Optics Express* **15**, 7610-7615 (2007).

123. S. M. Martin, F. H. Gebara, T. D. Strong, and R. B. Brown, "A low-voltage, chemical sensor interface for systems-on-chip: the fully-differential potentiostat," in *IEEE Proceedings of the International Symposium on Circuits and Systems*, pp. IV-892-895 (2004).

124. M. C. Rodriguez, A.-N. Kawde, and J. Wang, "Aptamer biosensor for label-free impedance spectroscopy detection of proteins based on recognition-induced switching of the surface charge," *Chemical Communications*, 4267-4269 (2005).

125. L. C. Bock, L. C. Griffin, J. A. Latham, E. H. Vermaas, and J. J. Toole, "Selection of single-stranded DNA molecules that bind and inhibit human thrombin," *Nature* **355**, 564-566 (1992).

126. R. Walsh, and M. C. DeRosa, "Retention of function in the DNA homolog of the RNA dopamine aptamer," *Biochemical and Biophysical Research Communications* **388**, 732-735 (2009).

127. K. Min, M. Cho, S.-Y. Han, Y.-B. Shim, J. Ku, and C. Ban, "A simple and direct electrochemical detection of interferon-γ using its RNA and DNA aptamers," *Biosensors and Bioelectronics* **23**, 1819-1824 (2008).

128. N. Savory, K. Abe, K. Sode, and K. Ikebukuro, "Selection of DNA aptamer against prostate specific antigen using a genetic algorithm and application to sensing," *Biosensors and Bioelectronics* **26**, 1386-1391 (2010).

129. A. S. Potty, K. Kourentzi, H. Fang, G. W. Jackson, X. Zhang, G. B. Legge, and R. C. Willson, "Biophysical characterization of DNA aptamer interactions with vascular endothelial growth factor," *Biopolymers* **91**, 145-156 (2009).

130. H. H. Salamanca, M. A. Antonyak, R. A. Cerione, H. Shi, and J. T. Lis, "Inhibiting heat shock factor 1 in human cancer cells with a potent RNA aptamer," *PloS One* **9**, e96330 (2014).

131. D. M. Tasset, M. F. Kubik, and W. Steiner, "Oligonucleotide inhibitors of human thrombin that bind distinct epitopes," *Journal of Molecular Biology* **272**, 688-698 (1997).

132. K. Y. Wang, S. H. Krawczyk, N. Bischofberger, S. Swaminathan, and P. H. Bolton, "The tertiary structure of a DNA aptamer which binds to and inhibits thrombin determines activity," *Biochemistry* **32**, 11285-11292 (1993).

133. B. I. Kankia, and L. A. Marky, "Folding of the thrombin aptamer into a G-quadruplex with Sr2+: stability, heat, and hydration," *Journal of the American Chemical Society* **123**, 10799-10804 (2001).

134. M. Tsiang, C. S. Gibbs, L. C. Griffin, K. E. Dunn, and L. L. Leung, "Selection of a suppressor mutation that restores affinity of an oligonucleotide inhibitor for thrombin using in vitro genetics," *Journal of Biological Chemistry* **270**, 19370-19376 (1995).

135. A. Smith, C. Patterson, J. Yarnell, A. Rumley, Y. Ben-Shlomo, and G. Lowe, "Which hemostatic markers add to the predictive value of conventional risk factors for coronary heart disease and ischemic stroke? The Caerphilly Study," *Circulation* **112**, 3080-3087 (2005).

136. D. M. Monroe, M. Hoffman, and H. R. Roberts, "Platelets and thrombin generation," *Arteriosclerosis, Thrombosis, and Vascular Biology* **22**, 1381-1389 (2002).

137. O. O. Ilesanmi, "Pathological basis of symptoms and crises in sickle cell disorder: implications for counseling and psychotherapy," *Hematology Reports* **2**, 10-23 (2010).

138. C. V. Pagba, S. M. Lane, and S. Wachsmann-Hogiu, "Raman and surface-enhanced Raman spectroscopic studies of the 15-mer DNA thrombin-binding aptamer," *Journal of Raman Spectroscopy* **41**, 241-247 (2010).

139. P. Larkin, "Infrared and Raman spectroscopy; principles and spectral interpretation" (Elsevier, 2011).

140. Y. Wang, K. Lee, and J. Irudayaraj, "SERS aptasensor from nanorod–nanoparticle junction for protein detection," *Chemical Communications* **46**, 613-615 (2010).

141. C. Otto, T. Van den Tweel, F. De Mul, and J. Greve, "Surface-enhanced Raman spectroscopy of DNA bases," *Journal of Raman Spectroscopy* **17**, 289-298 (1986).

142. S. Balamurugan, A. Obubuafo, R. L. McCarley, S. A. Soper, and D. A. Spivak, "Effect of linker structure on surface density of aptamer monolayers and their corresponding protein binding efficiency," *Analytical Chemistry* **80**, 9630-9634 (2008).

143. S. Weiss, "Fluorescence spectroscopy of single biomolecules," *Science* **283**, 1676-1683 (1999).

144. I. R. Krauss, A. Merlino, A. Randazzo, E. Novellino, L. Mazzarella, and F. Sica, "High-resolution structures of two complexes between thrombin and thrombin-binding aptamer shed light on the role of cations in the aptamer inhibitory activity," *Nucleic Acids Research*, gks512 (2012).

145. K. Toda, P. K. Dasgupta, J. Li, G. A. Tarver, and G. M. Zarus, "Fluorometric field instrument for continuous measurement of atmospheric hydrogen sulfide," *Analytical Chemistry* **73**, 5716-5724 (2001).

146. R. M. Bethea, "Comparison of hydrogen sulfide analysis techniques," *Journal of the Air Pollution Control Association* **23**, 710-713 (1973).

147. R. Beauchamp, J. S. Bus, J. A. Popp, C. J. Boreiko, D. A. Andjelkovich, and P. Leber, "A critical review of the literature on hydrogen sulfide toxicity," *Critical Reviews in Toxicology* **13**, 25-97 (1984).

148. R. Wang, "Physiological implications of hydrogen sulfide: a whiff exploration that blossomed," *Physiological Reviews* **92**, 791-896 (2012).

149. H. D. Axelrod, J. H. Cary, J. E. Bonelli, and J. P. Lodge Jr, "Fluorescence determination of sub-parts-per-billion hydrogen sulfide in the atmosphere," *Analytical Chemistry* **41**, 1856-1858 (1969).

150. A. Blanchette, and A. Cooper, "Determination of hydrogen sulfide and methyl mercaptan in mouth air at the parts-per-billion level by gas chromatography," *Analytical Chemistry* **48**, 729-731 (1976).

151. D. R. Linden, L. Sha, A. Mazzone, G. J. Stoltz, C. E. Bernard, J. K. Furne, M. D. Levitt, G. Farrugia, and J. H. Szurszewski, "Production of the gaseous signal molecule hydrogen sulfide in mouse tissues," *Journal of Neurochemistry* **106**, 1577-1585 (2008).

152. A. V. Mashkina, "Heterogeneous catalytic synthesis of alkanethiols and dialkyl sulfides from alcohols and hydrogen sulfide," *Russian Chemical Reviews* **64**, 1131 (1995).

153. J. Durig, W. Bucy, C. Wurrey, and L. Carreira, "Raman spectra of gases. XVI. Torsional transitions in ethanol and ethanethiol," *The Journal of Physical Chemistry* **79**, 988-993 (1975).

154. D. Maniu, V. Chis, M. Baia, F. Toderas, and S. Astilean, "Density functional theory investigation of p-aminothiophenol molecules adsorbed on gold nanoparticles," *Journal of Optoelectronics and Advanced Materials* **9**, 733 (2007).

155. J. Martin, and S. Montero, "Raman intensities of ethane and deuterated derivatives," *The Journal of Chemical Physics* **80**, 4610-4619 (1984).

156. G. M. Whitesides, "The origins and the future of microfluidics," *Nature* **442**, 368-373 (2006).

157. M. J. de Boer, J. Gardeniers, H. V. Jansen, E. Smulders, M.-J. Gilde, G. Roelofs, J. N. Sasserath, and M. Elwenspoek, "Guidelines for etching silicon MEMS structures using fluorine high-density plasmas at cryogenic temperatures," *Journal of Microelectromechanical Systems* **11**, 385-401 (2002).

158. A. Rajagopal, C.-f. Chang, C. Tschirhart, S. S. Walavalkar, and A. Scherer, "Nanoscale Pillar MOSFET for Neural Sensing," in *IEEE EMBS Micro and Nanotechnology in Medicine Conference*, ThBT1.10 (2012).

159. H. Jansen, M. De Boer, S. Unnikrishnan, M. Louwerse, and M. Elwenspoek, "Black silicon method X: a review on high speed and selective plasma etching of silicon with profile control: an in-depth comparison between Bosch and cryostat DRIE processes as a roadmap to next generation equipment," *Journal of Micromechanics and Microengineering* **19**, 033001 (2009).

160. C.-f. Chang, S. S. Walavalkar, A. Scherer, B. Marin, and S. E. Fraser, "Plasmonic Nanostructures for Multiplexing Implantable Sensors," U.S. serial/patent #14/621,265, international PCT/US2015/0516, filed Feb/12/2015, patent pending.

161. I. Barman, C.-R. Kong, G. P. Singh, R. R. Dasari, and M. S. Feld, "Accurate spectroscopic calibration for noninvasive glucose monitoring by modeling the physiological glucose dynamics," *Analytical Chemistry* **82**, 6104-6114 (2010).

162. C.-f. Chang, S. S. Walavalkar, S. E. Fraser, and A. Scherer, "Fabrication and Self-Aligned Local Functionalization of Plasmonic Nanostructures on Flexible Substrates for Implantable and Sensing Applications," U.S. serial/patent #62/089,724, provisional application filed Dec/09/2014.

163. J. C. Lo, S. Hong, R. J. Anderson, L. P. Lee, D. A. Horsley, and J. L. Skinner, "Fabrication of a large, ordered, three-dimensional nanocup array," *Applied Physics Letters* **101**, 081109 (2012).

164. Z. Wang, G. Shimon, X. Liu, C. Thompson, C. Ross, W. Choi, and A. Adeyeye, "Synthesis and magnetic properties of large-area ferromagnetic cylindrical nanoshell and nanocup arrays," *Journal of Applied Physics* **113**, 214301 (2013).

165. M. Frederiksen, V. E. Bochenkov, M. B. Cortie, and D. S. Sutherland, "Plasmon hybridization and field confinement in multilayer metal–dielectric nanocups," *The Journal of Physical Chemistry C* **117**, 15782-15789 (2013).

166. Y. Mishra, R. Adelung, G. Kumar, M. Elbahri, S. Mohapatra, R. Singhal, A. Tripathi, and D. Avasthi, "Formation of self-organized silver nanocup-type structures and their plasmonic absorption," *Plasmonics* **8**, 811-815 (2013).

167. I. Malitson, "Interspecimen comparison of the refractive index of fused silica," *Journal of the Optical Society of America* **55**, 1205-1208 (1965).

168. B. S. Kawasaki, K. O. Hill, and R. Lamont, "Biconical-taper single-mode fiber coupler," *Optics Letters* **6**, 327-328 (1981).

169. E. N. Kaufman, J. B. Harkins, and A. P. Borole, "Comparison of batchstirred and electrospray reactors for biodesulfurization of dibenzothiophene in crude oil and hydrocarbon feedstocks," *Applied Biochemistry and Biotechnology* **73**, 127-144 (1998).

170. S. G. Rodrigo, F. García-Vidal, and L. Martín-Moreno, "Influence of material properties on extraordinary optical transmission through hole arrays," *Physical Review B* **77**, 075401 (2008).

171. M. Mitas, K. Mikhitarian, C. Walters, P. L. Baron, B. M. Elliott, T. E. Brothers, J. G. Robison, J. S. Metcalf, Y. Y. Palesch, and Z. Zhang, "Quantitative real-time RT-PCR detection of breast cancer micrometastasis using a multigene marker panel," *International Journal of Cancer* **93**, 162-171 (2001).

172. N. S. King, Y. Li, C. Ayala-Orozco, T. Brannan, P. Nordlander, and N. J. Halas, "Angle-and spectral-dependent light scattering from plasmonic nanocups," *ACS Nano* **5**, 7254-7262 (2011).

173. Y. Zhang, N. K. Grady, C. Ayala-Orozco, and N. J. Halas, "Three-dimensional nanostructures as highly efficient generators of second harmonic light," *Nano Letters* **11**, 5519-5523 (2011).